TROPICAL CYCLONE INTENSITIES FROM SATELLITE MICROWAVE DATA

By

Thomas H. Vonder Haar, Principal Investigator

and

Stanley Q. Kidder, Co-Investigator

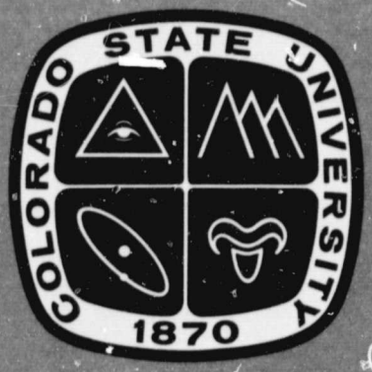

NASA GRANT NSG-5258
ANNUAL REPORT
(1 April 1979-31 March 1980)
and
FINAL REPORT

DEPARTMENT OF ATMOSPHERIC SCIENCE
COLORADO STATE UNIVERSITY
FORT COLLINS, COLORADO

TROPICAL CYCLONE INTENSITIES FROM SATELLITE MICROWAVE DATA

Annual Report
(Period: 1 April 1979 to 31 March 1980)

and

Final Report

for

National Aeronautics and Space Administration
Grant NSG-5258

by

Thomas H. Vonder Haar, Principal Investigator
Department of Atmospheric Science
Colorado State University
Ft. Collins CO 80523

and

Stanley Q. Kidder, Co-Investigator
Laboratory for Atmospheric Research
University of Illinois
Urbana IL 61801

July 1980

NASA Technical Officer: Edward B. Rodgers

1.0 INTRODUCTION

During the final year of Grant sponsorship a paper reporting work done previously was published (Kidder, et al., 1980); a paper covering part of the work done this year was published (Chan et al., 1980), and a Master's thesis was completed (Durkee, 1980). All of these papers are reproduced in Appendix B. A complete list of puclications sponsored by Grant NSG-5258 is presented in Appendix A. Scientific results obtained during the period 1 April 1979 to 31 March 1980 are summarized in the next section.

2.0 SUMMARY OF SCIENTIFIC RESULTS

Work during this period concentrated on three areas: forecasting intensity change in tropical cyclones, forecasting tropical cyclone turning motion, and detecting summer precipitation over the North Central U.S.

2.1 Tropical Cyclone Intensity Change

It has often been mentioned that for tropical cyclones to form or intensify, they must exist in large-scale environments of low-level positive relative vorticity and upper-level negative relative vorticity (Riehl, 1948, 1950; Yanai, 1961; Dvorak, 1975; Sadler, 1976, 1978). Recently McBride (1979) has done compositing studies of developing versus non-developing cloud clusters. He found that the single most important indicator of tropical cyclone genesis was the difference between low-level (900 mb) and upper-level (200 mb) relative vorticity averaged over the area 0°- 6° latitude centered on the precursor cloud cluster. $\langle \zeta_{900} - \zeta_{200} \rangle_{0°-6°}$ is larger by a factor of three for developing systems.

By thermal wind arguments, this vorticity difference is related to the laplacian of the mean temperature of the 900 mb to 200 mb layer:

$$\zeta_{900} - \zeta_{200} = - \frac{R}{f} \ln(\frac{900}{200}) \nabla^2 \overline{T}_{900-200} \qquad (1)$$

where R is the gas constant, and f the Coriolis parameter. When averaged over the 0°-6° area, this becomes

$$\langle \zeta_{900-200} \rangle_{0°-6°} = - \frac{R}{f} \ln(\frac{900}{200}) \frac{2}{r_{6°}} [\frac{\partial}{\partial r} \overline{T}_{900-200}]_{6°}$$

where square brackets indicate averaging around the circle whose radius is indicated by the subscript, and $r_{6°}$ is the radius of the 6° latitude circle. Eq. (2) states that if a tropical disturbance is going to develop (intensify) one should see an inward gradient of $\overline{T}_{900-200}$.

To see whether satellite sounder data may play a role in forecasting tropical cyclone intensity, radial profiles of mean 1000 mb to 250 mb temperature from the Nimbus 6 Scanning Microwave Spectrometer (SCAMS) were constructed around eight intensifying tropical storms in the western Pacific during the period August, 1975, to January, 1976 (Fig. 1). Seven showed distinct inward temperature gradients, required for intensification. The eighth (Alice) did not display an inward gradient and indeed was decaying 24 h later.

Because the current operational polar-orbiting satellites (TIROS-N and NOAA-6) provide a dense network of soundings in the tropics, the above results indicate that they may play a key role in forecasting intensity changes in tropical cyclones.

2.2 Tropical Cyclone Track Forecasting

In order to better understand the relation between a tropical cyclone's motion and the mass and flow fields of its environment, J. C. L.

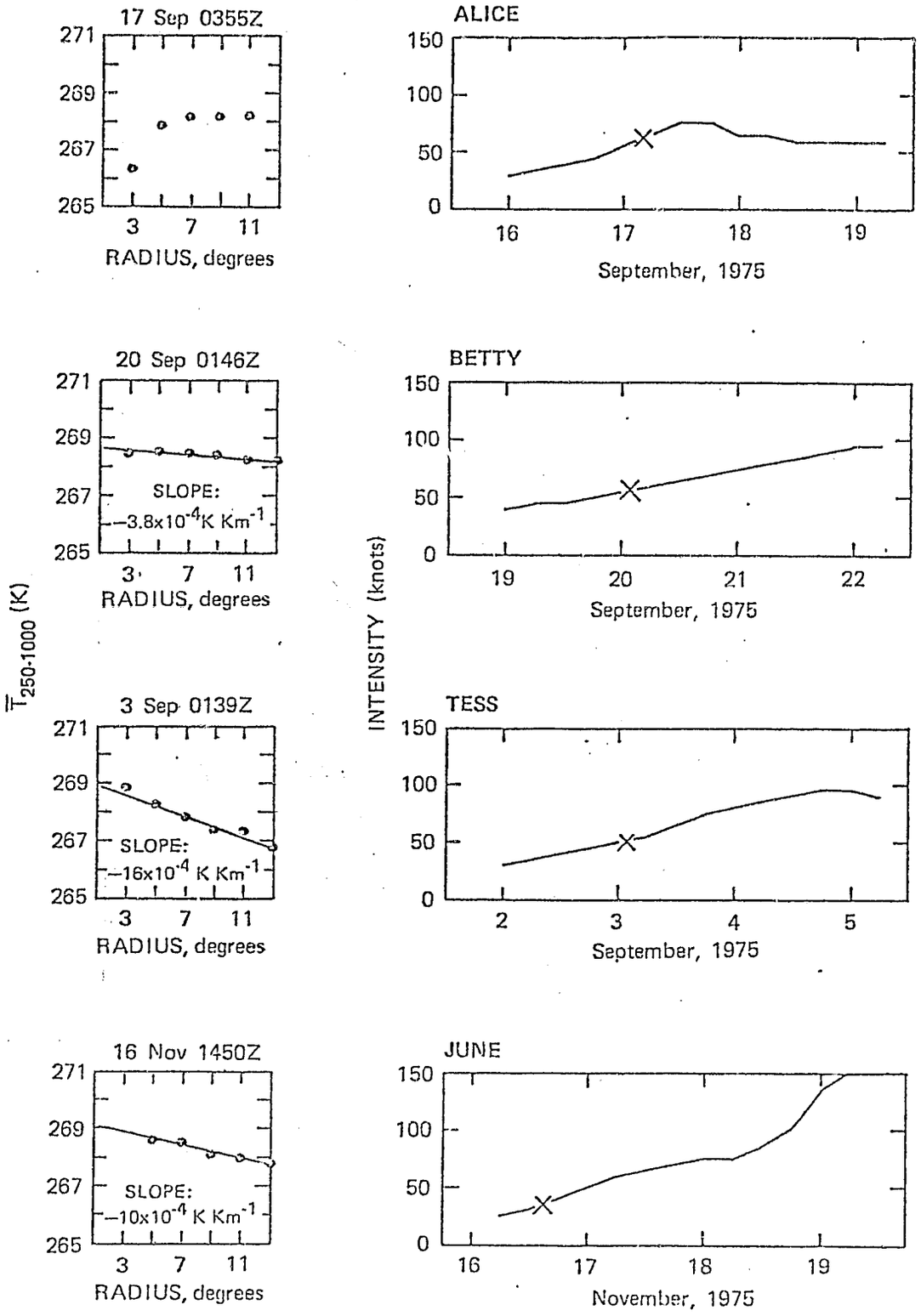

Fig. 1. Left: Mean 1000-250 mb temperatures as inferred from Nimbus 6 SCAMS data versus radius for eight typhoons. Time of satellite observation is indicated above the graph. Right: Plot of storm intensity versus time. Time of satellite observation is marked with an X.

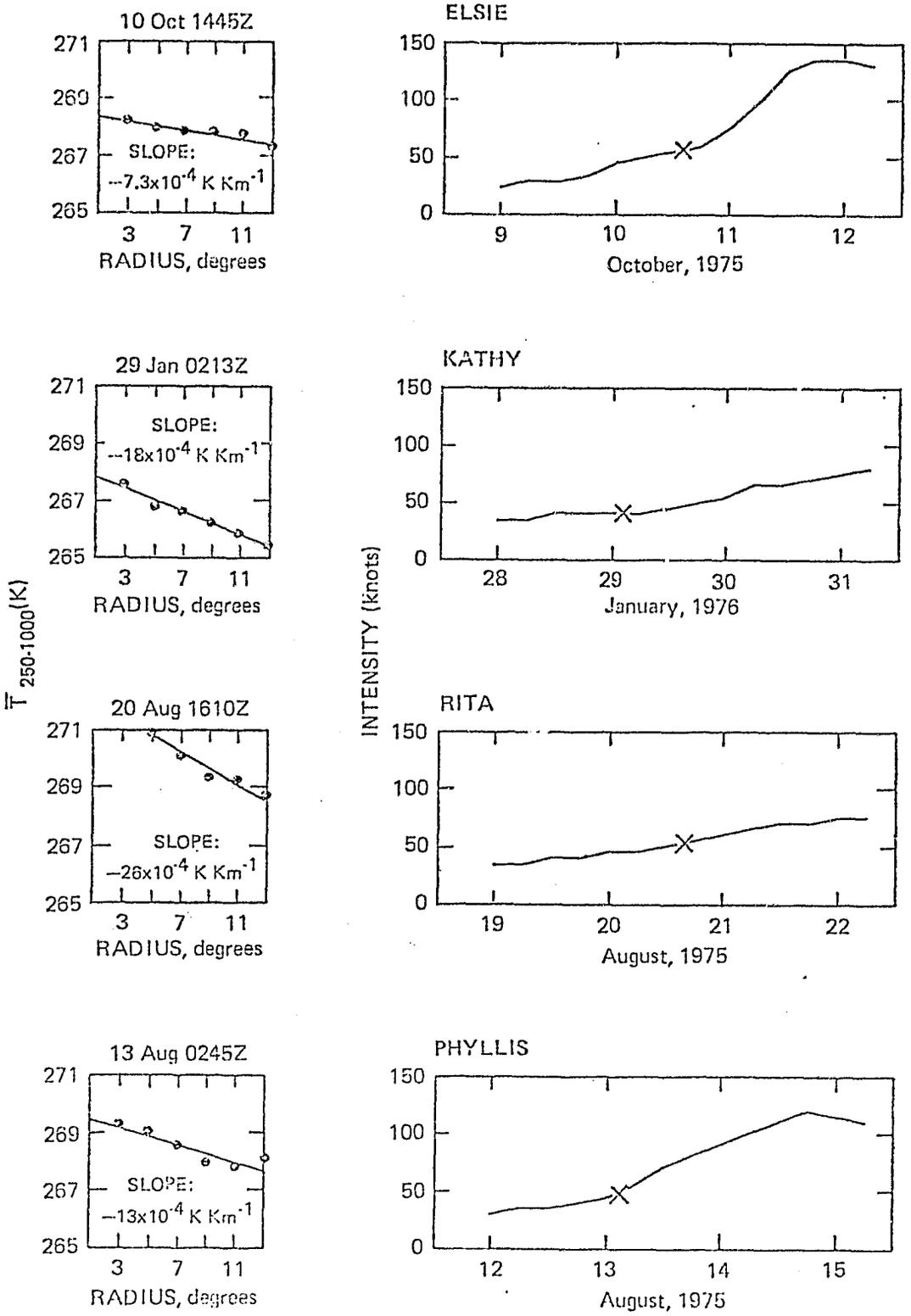

Fig. 1. (continued)

Chan and W. M. Gray of Colorado State University composited rawinsonde observations around West Indies tropical cyclones for the period 1961-1977. When they stratified their data into three classes--storms which turned right, storms which turned left, and storms which continued on a straight track--they found that 24 to 36 h before a storm turned, the vertical shear (difference between 900 and 200 mb) of the component of the environmental wind in the direction of storm motion (V_p) was distinctly different in the three cases. For storms which turned right 24 to 36 h later, V_p decreased with height; for storms which turned left V_p increased with height; and for straight-moving storms V_p changed little with height. Although the exact dynamical connection between vertical shear of V_p and storm direction is not fully understood, it appears to have potential as a forecast tool.

By thermal wind considerations the shear of V_p should be reflected in the horizontal gradient of the mean temperature between 900 and 200 mb ($\overline{T}_{900-200}$) such that turning storms turn toward cold air. Because microwave sounders can estimate such mean temperatures even in the presence of clouds, we were asked by Chan and Gray to investigate the possibility that satellite data might be used to forecast tropical cyclone turning motion. Estimates of the mean 1000 to 250 mb temperature field around eleven tropical storms in 1975 were obtained from Nimbus 6 SCAMS data tapes. Analysis of these data showed that for turning storms, in all but one case, the turn was signaled 24 h in advance by a significant temperature gradient perpendicular to the storm's path at a distance of 9° to 13° in front of the storm. Similarly, in all but one case, storms which continued on a straight course showed no significant gradient of $\overline{T}_{1000-250}$. These results have been submitted for publication (Chan et al.,

1980; see Appendix B). They may have the potential to improve tropical cyclone 24 h position forecasts, the error in which is currently nearly 200 km.

2.3 Summer Precipitation Frequency

The Electrically Scanning Microwave Radiometer on board Nimbus 6 (ESMR-6) measures both vertically and horizontally polarized upwelling radiation in a 250 MHz band centered at 37 GHz. At these frequencies, precipitation appears cold in comparison with high emittance, high temperature land. A thresholding technique was developed to distinguish cold rain from warmer, non-raining areas. Rain was separated from standing water by examination of the two polarizations. Fig. 2 shows a comparison between ESMR-6-derived area of precipitation and raingage measurements. The thresholding technique was applied to the North Central U.S. during the Summer of 1976 to estimate precipitation frequency. Good agreement was found between gauge measurements and satellite estimates except in Minnesota where a large number of small lakes probably biased the estimates.

3.0 SUGGESTED FUTURE WORK

One half of the earth's surface lies between 30°N and 30°S, and 47 percent of that area is covered by ocean where few conventional meteorological observations are made. Satellite observations, therefore, have the potential to substantially improve weather analysis and forecasting in the tropics.

Satellite sounder data has not been used extensively in the tropics because the uncertainty in the retrieved temperature at a particular level is often greater than the climatological variation. During the

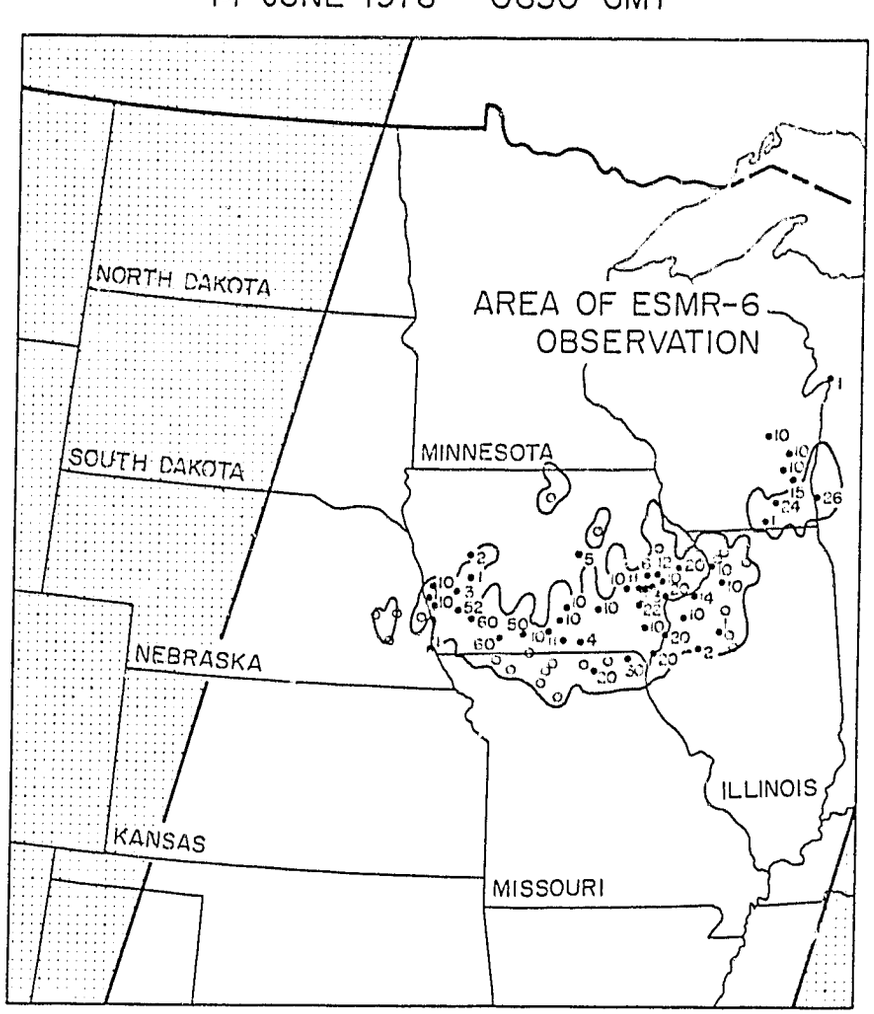

Figure 2. Satellite derived rain areas and amounts of rainfall (hundredths of an inch) at surface observing raingages for 14 June 1976 at 0630 GMT. Area of satellite observation is also indicated.

course of this Grant, however, we have shown that if one carefully chooses the satellite data and the meteorological situation to be analyzed, satellite data can be very beneficial. We strongly recommend that efforts to apply satellite data to tropical weather analysis and forecasting be increased.

Significant temperature gradients occur over the tropical oceans only near tropical cyclones. During the first year of Grant sponsorship we showed that brightness temperature anomalies in the 55.45 GHz channel of the Nimbus 6 SCAMS (caused by upper tropospheric temperatuer anomalies) could be used to estimate surface wind speeds outside of the radius of maximum winds. Because this technique is suitable for use with the TIROS-N Microwave Sounding Unit (MSU) or with the Defense Military Satellite Program (DMSP) microwave sounder (SSM/T), we believe the technique should be tried with those data.

During the second year of Grant sponsorship, work concentrated on using mean tropospheric temperatures to forecast 1) turning motion of tropical cyclones, and 2) intensity change. Initial results of these investigations (described above) look extremely promising. We highly recommend that investigation in these areas continue, and one of us (S. Q. K.) has proposed to do so.

4.0 REFERENCES

Chan, J. C. L., W. M. Gray, and S. Q. Kidder, 1980: Forecasting tropical cyclone turning motion from surrounding wind and temperature fields. Mon. Wea. Rev., 108, 778-792.

Durkee, P. A., 1980: Summer precipitation frequency of the North Central U.S. from satellite microwave observations. M.S. Thesis, Colorado State University, Ft. Collins, 67 pp.

Dvorak, V. F., 1975: Tropical cyclone intensity analysis and forecasting from satellite imagery. Mon. Wea. Rev., 103, 420-430.

Kidder, S. W., W. M. Gray, and T. H. Vonder Haar, 1980: Tropical cyclone outer surface winds derived from satellite microwave sounder data. Mon. Wea. Rev., 108, 144-152.

McBride, J. L., 1979: Observational analysis of tropical cyclone formation. Atmos. Sci. Paper No. 308, Colo. State Univ., Ft. Collins, 230 pp.

Riehl, H., 1948: On the formation of typhoons. J. Meteor., 5, 247-264.

_____, 1950: A model of hurricane formation. J. Appl. Phys., 21, 917-925.

Sadler, J. C., 1976: A role of the tropical upper troposphere in early season typhoon development. Mon. Wea. Rev., 104, 1266-1278.

_____, 1978: Mid-season typhoon development and intensity changes and the tropical upper tropospheric trough. Mon. Wea. Rev., 106, 1137-1152.

Yanai, M., 1961: A detailed analysis of typhoon formation. J. Meteor. Soc. Japan, 39, 187-214.

APPENDIX A

Publications Sponsored by
NASA GRANT NSG-5258

Publications Sponsored by NASA Grant NSG-5258

Chan, J. C. L., W. Gray, and S. Q. Kidder, 1980: Forecasting tropical cyclone turning motion from surrounding wind and temperature fields. Mon. Wea. Rev., 108, 778-792.

Durkee, P. A., 1980: Summer precipitation frequency of the North Central U.S. from satellite microwave observations. M.S. Thesis, Colorado State Univ., Ft. Collins, 67 pp.

Kidder, S. Q., W. M. Gray, and T. H. Vonder Haar, 1978: Estimating tropical cyclone central pressure and outer winds from satellite microwave data. Mon. Wea. Rev., 106, 1458-1464.

_____, _____, and _____, 1980: Tropical cyclone outer surface winds derived from satellite microwave sounder data. Mon. Wea. Rev., 108, 144-152.

APPENDIX B

Papers Sponsored by NASA Grant NSG-5258
During the Period 1 April 1979 to 31 March 1980

Reprinted from MONTHLY WEATHER REVIEW, Vol. 108, No. 2, February 1980
American Meteorological Society
Printed in U. S. A.

Tropical Cyclone Outer Surface Winds Derived from Satellite Microwave Sounder Data

STANLEY Q. KIDDER, WILLIAM M. GRAY AND THOMAS H. VONDER HAAR

Tropical Cyclone Outer Surface Winds Derived from Satellite Microwave Sounder Data

STANLEY Q. KIDDER,[1] WILLIAM M. GRAY AND THOMAS H. VONDER HAAR

Department of Atmospheric Science, Colorado State University, Ft. Collins, 80523

(Manuscript received 17 September 1979, in final form 26 November 1979)

ABSTRACT

Upper tropospheric temperature anomalies are detected in brightness temperature data from the Nimbus 6 Scanning Microwave Spectrometer (SCAMS). Brightness temperature anomalies are related to surface pressure anomalies through the radiative transfer and hydrostatic equation. Surface wind speeds at outer radii are then estimated using the gradient wind equation and a shearing parameter. The method is first tested using simulated satellite data constructed from temperature, pressure and height data recorded by aircraft reconnaissance of four hurricanes. Wind speeds in the 80–95 kPa region are estimated with 2–3 m s $^{-1}$ accuracy. Next, 55.45 GHz SCAMS data over eight typhoons during 1975 are used to estimate the radii of 15.4 m s $^{-1}$ (30 kt) and 27.5 m s $^{-1}$ (50 kt) winds. Accuracies of about ±80 and ±70 km, respectively, are found. It is suggested that the technique be further tested using data from the Microwave Sounding Unit (MSU) on board the TIROS-N and NOAA 6 satellites.

1. Introduction

Over large areas of the oceans, the only feasible method for monitoring tropical cyclones is through the use of satelliteborne instrumentation. Since the launch of the first meteorological satellite in 1960, scientists have been collecting such data. Today the data are abundant and the challenge is to translate the raw data into accurate estimates of meteorological parameters.

One of the most important parameters of a tropical cyclone is surface wind speed. Among the uses of surface wind speed information are the following. Numerical models of storm motion need the wind speeds as input. Those responsible for routing ships need to chart courses which are outside the radius of 30 kt winds. Storm surge models are very sensitive to wind speed. Over the years a great deal of work has gone into the estimation of maximum sustained surface wind speed (intensity). The culmination of these efforts is the widely used Dvorak (1975) technique which is based on a correlation of intensity with cloud patterns. Unfortunately, the Dvorak technique does not estimate wind speeds at outer radii which are poorly related to intensity (see Gray and Frank, 1978, Tables 14 and 15). Recently, however, because of their importance to ship routing and storm surge prediction (Jelesnianski and Taylor, 1973), outer winds have become a topic of interest. Rodgers *et al.* (1979) have obtained good estimates of low-level wind speeds around tropical cyclones by tracking clouds in high-frequency (7.5 min) GOES (Geosynchronous Operational Environmental Satellite) images. Initial results from the Seasat-A Scatterometer System (SASS) and the Scanning Multichannel Microwave Radiometer (SMMR)[2], also on board Seasat, indicate that in the future, these instruments may be able to estimate surface wind speeds around tropical cyclones by observing the sea state (Jones *et al.*, 1979; Lipes *et al.*, 1979).

In a previous paper (Kidder *et al.*, 1978) we proposed a microwave technique for estimating surface wind speeds at outer radii which has several potential advantages over other techniques. First, it is suitable for use with the Microwave Sounding Unit (MSU) on board the current polar-orbiting operational satellites (TIROS-N and NOAA 6). Second, it requires only a small amount of computing and no special equipment, such as video displays. Third, it utilizes routinely available data; no special observations are needed. Fourth, the technique is unaffected by the extensive cloudiness which surrounds a tropical cyclone. And finally, it is an objective technique based soundly on the radiative transfer, hydrostatic and gradient wind equations. Note that in related work Grody *et al.* (1979) have used microwave data to estimate weighted mean tropospheric wind speeds around Typhoon June (1975).

In this paper we drive a more exact relationship between satellite-observed brightness temperatures and surface wind speeds than presented in Kidder

[1] Current affiliation: Laboratory for Atmospheric Research, University of Illinois, Urbana 61801.

[2] SMMR is also on board the Nimbus 7 satellite.

0027-0644/80/020144-09$06.25

et al. (1978). The theory is first tested using simulated satellite data constructed from aircraft reconnaissance of four hurricanes. The theory is next tested using data from the 55.45 GHz channel of the Nimbus 6 Scanning Microwave Spectrometer (SCAMS) to estimate the radii of 15.4 m s $^{-1}$ (30 kt) and 25.7 m s $^{-1}$ (50 kt) winds in eight West Pacific typhoons during 1975. We call this technique the Surface Wind Inference from Microwave data (SWIM) technique.

2. Theory

The high surface winds in a tropical cyclone are caused by surface pressure gradients which are in turn caused by warm temperature anomalies in the upper troposphere. The basis of the SWIM technique is that microwave radiometers can measure the upper level warming which may then be related to surface winds.

a. Tropical cyclone temperature structure

Shown in Fig. 1 are the mean temperature anomalies (difference from storm environment) for west Pacific typhoons and for Atlantic (West Indies) hurricanes as composited from rawinsonde data by Núñez and Gray (1977). The two main features of the curves are 1) the large positive anomalies peaking between 25 and 30 kPa and extending several hundred kilometers from the storm center, and 2) the remarkable similarity in the shape of the profiles at different radii. Specifically, the temperature anomaly is well approximated by

$$T'(r,z) = \alpha(r)\hat{T}(z), \qquad (1)$$

where $\hat{T}(z)$ is a standard known temperature anomaly profile (slightly different in the different oceans) and $\alpha(r)$ is a strength parameter, which will be different for different storms. That this relationship is not an artifact of the compositing procedure may be seen in plots of temperature anomalies in individual storms (e.g., in LaSeur and Hawkins, 1963; Hawkins and Rubsam, 1968; Hawkins and Imbembo, 1976).

It must be noted that the profiles shown in Fig. 1 have been modified slightly from those presented in Núñez and Gray (1977). First, because there were few statistically significant temperature anomalies at low levels, the profiles were extrapolated to zero at 100 kPa in the Pacific and at 70 kPa in the Atlantic. Second, small cold anomalies exist above the storms due to overshooting Cb cloud tops and/or radiative cooling. Because data are sparse at upper levels, this cooling was parameterized as follows. In the Atlantic, where storms are shallower than in the Pacific, the cooling was assumed to be zero at 16.25 kPa and 5 kPa and to be parabolic between with the amplitude determined by the 20 kPa anomaly such that the slope was continuous across 16.25 kPa. This parameterization fits the data rather well (see Kidder, 1979). In the Pacific, the cooling, shown schematically with the dotted line in Fig. 1a, was ignored because of statistical uncertainty in rawinsonde data at that altitude. It also made no difference in the calculations presented below.

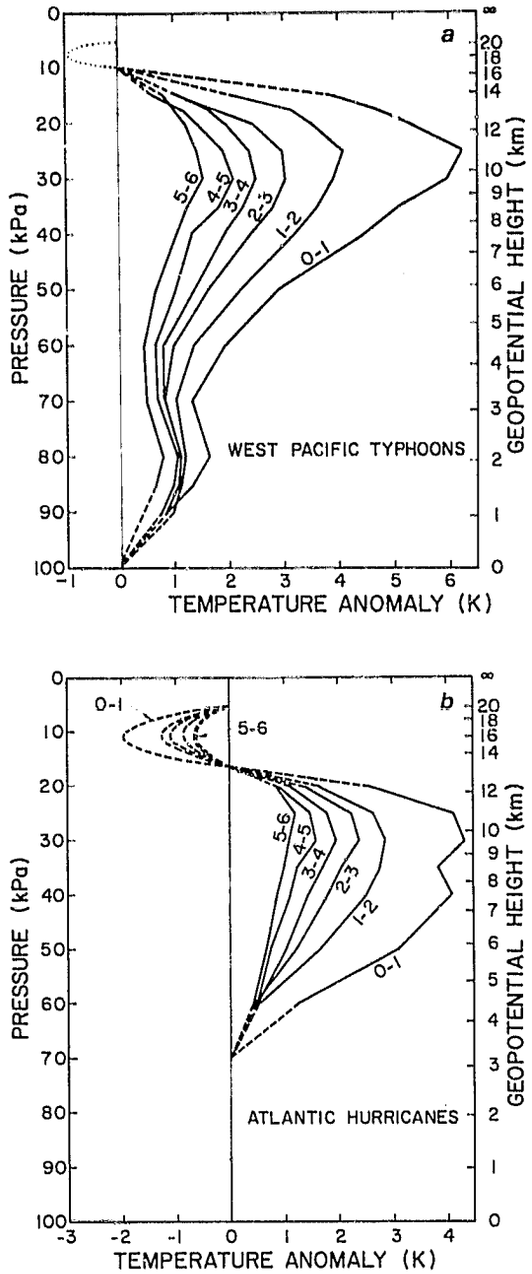

FIG. 1. Mean temperature anomalies in 1° radial bands for (a) West Pacific typhoons and (b) Atlantic (West Indies) hurricanes (after Nuñez and Gray, 1977).

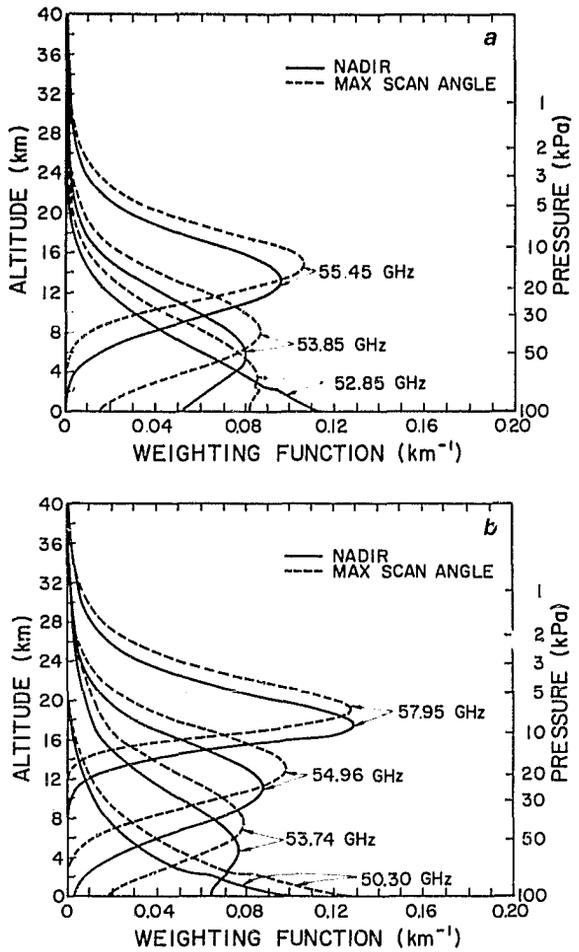

FIG. 2. Weighting functions for (a) the Nimbus 6 Scanning Microwave Spectrometer (SCAMS) and (b) the TIROS-N/NOAA Microwave Sounding Unit (MSU) in the 15° North Annual Atmosphere.

b. *Radiometer characteristics*

The SCAMS instrument is a five-channel radiometer sensing radiation nominally at 22.235, 31.65, 52.85, 53.85 and 55.45 GHz (Staelin *et al.*, 1975a). The lower two frequencies are used to estimate integrated liquid water and water vapor (Grody, 1976). The upper three channels, which are on the wing of an oxygen (O_2) absorption band, are used to sound the atmosphere. In the absence of scattering [due to particles of diameter ≥ 0.2 mm (i.e., precipitation)] the brightness temperature measured by channel i($i = 3, 4, 5$) of the radiometer is given by a form of the radiative transfer equation:

$$T_{B_i} = \epsilon_i T_s \tau_i + \int_0^\infty T(z)\, W_i(z) dz, \qquad (2)$$

where ϵ_i is the surface emittance, τ_i the transmittance from the surface to the satellite, T_s the surface temperature, $T(z)$ the atmospheric temperature at height z and $W_i(z)$ a weighting function (Staelin *et al.*, 1975a). $W_i(z)$ and ϵ_i are both weakly dependent on temperature but more strongly dependent on scan angle. Fig. 2 shows the weighting functions for the SCAMS and for the MSU on board the TIROS-N and NOAA 6 satellites. The 15° North Annual Atmosphere was used to construct these weighting functions, and it was assumed that the surface was the ocean where ϵ_i is ~0.5.

At frequencies which peak in the upper troposphere, warm brightness temperature anomalies should be observed over tropical cyclones. These warm anomalies were first observed in 55.45 GHz SCAMS data over Typhoon June of 1975 by Rosenkranz and Staelin (1976) and Rosenkranz *et al.* (1978) and over other storms by Kidder *et al.* (1978). All of the above authors concluded that the brightness temperature anomalies were not caused by clouds, which are far too transparent to cause anomalies of several kelvin (Staelin *et al.*, 1975b; Kidder, 1979) or by precipitation, which will be frozen (and thus much less able to interact with microwave radiation) at the levels sensed by the SCAMS 55.45 GHz channel. The brightness temperature anomalies are directly related to thermodynamic temperature anomalies in the storms as shown in Fig. 1. The object of this paper is to translate these satellite-observed brightness temperature anomalies into storm parameters of interest to the meteorologist.

c. *Surface pressure equation*

Warming in the upper troposphere is responsible for the surface pressure drop in tropical cyclones. Because satellite-measured brightness temperature (at certain frequencies) is a measure of this upper warming, brightness temperature ought to be related to surface pressure. It was shown in Kidder *et al.* (1978) that 55.45 GHz brightness temperature anomalies are statistically correlated with central pressure. A more exact relationship may be derived as follows. At a frequency for which the transmittance from the surface to the satellite is vanishingly small, the surface term in Eq. (2) may be neglected. Thus

$$T_B = \int_0^\infty T(z)\, W(z) dz. \qquad (3)$$

If the atmospheric temperature is divided into environmental temperature T_e plus temperature perturbation T', and if Eq. (1) is used to express T', we can write

$$T_B = \int_0^\infty T_e(z)\, W(z) dz + \int_0^\infty T'(r,z)\, W(z) dz \qquad (4)$$

or

$$T_B = T_{B_e} + \alpha(r) \int_0^x \hat{T}(z) W(z) dz, \qquad (5)$$

where T_{B_e} is the environmental brightness temperature. In the above, the small variation of the weighting function with temperature has been neglected.

The surface pressure outside of the radius of maximum wind can be obtained from the hydrostatic equation.[3] If the hydrostatic equation is integrated from the surface to a height such as the 5 kPa level which is undisturbed by the storm (Frank, 1977), we have

$$\ln p_s = \ln p_T + \frac{g}{R} \int_0^{H_T} \frac{dz}{T(z)}. \qquad (6)$$

Substituting for $T(z)$ as above and using the binomial expansion, keeping only terms linear in $\alpha(r)$, yields

$$\ln p_s = \ln p_e - \alpha(r) \frac{g}{R} \int_0^{H_T} \frac{\hat{T}(z)}{T_e^2(z)} dz, \qquad (7)$$

where p_e is the environmental surface pressure, and H_T the height of the 5 kPa surface. The unknown $\alpha(r)$ may now be eliminated between Eqs. (5) and (7) to yield

$$\Delta \ln p_s = -A \Delta T_B, \qquad (8)$$

where Δ indicates a departure from the environmental value and A is given by

$$A = \frac{\frac{g}{R} \int_0^{H_T} \frac{\hat{T}(z)}{T_e^2(z)} dz}{\int_0^x \hat{T}(z) W(z) dz}. \qquad (9)$$

Eq. (8) relates surface pressure anomalies to anomalies in a satellite-observed quantity (brightness temperature). Its usefulness depends on the characteristics of the coefficient A. Of chief concern is the uncertainty in the calculated value of A. An alternate method for calculating A which is slightly more accurate than Eq. (9) [because it takes into account the small variation of $W(z)$ with temperature] is to calculate the brightness temperature for a storm environment, then to perturb the environmental temperature with one of the profiles in Fig. 1 and calculate the surface pressure and brightness temperature anomalies. When this procedure was carried out using Pacific and Atlantic environmental soundings from the work of Núñez and Gray (1977) and atmospheric absorption coefficients calculated using the formulas of Liebe and Gimmestad (1978) and Liebe *et al.* (1977), the values of A listed in Table 1 resulted. There seems to be no systematic variation in A with radius, and the standard deviations of the samples are less than 10% of the mean values. Furthermore, A seems to be fairly insensitive to changes in the environment. Changing to the U.S. Standard Atmosphere changes A only ~12%. Similarly, switching an Atlantic temperature anomaly profile to a Pacific profile only changes A by ~11%. It thus appears that the coefficient A can be calculated from existing data, and it has a rather small uncertainty.

TABLE 1. Values of the coefficient A (K^{-1}) as a function of radius.

Radial band (deg latitude)	55.45 GHz	54.96 GHz
Atlantic		
0–1	1.13×10^{-2}	0.66×10^{-2}
1–2	1.10	0.66
2–3	1.07	0.64
3–4	1.03	0.62
4–5	1.01	0.62
5–6	0.94	0.54
6–7	0.85	0.51
Mean	1.02×10^{-2}	0.61×10^{-2}
Standard deviation	0.09×10^{-2}	0.06×10^{-2}
Pacific		
0–1	0.90×10^{-2}	0.82×10^{-2}
1–2	0.94	0.83
2–3	0.98	0.84
3–4	0.99	0.86
4–5	1.02	0.87
5–6	0.95	0.85
6–7	0.83	0.80
Mean	0.95×10^{-2}	0.84×10^{-2}
Standard deviation	0.06×10^{-2}	0.02×10^{-2}

Kidder *et al.* (1978) showed a high correlation (−0.86) between central surface pressure and the brightness temperature anomaly at the center of the storm. Although there are problems with this relationship due to the eye having a variable diameter, the high correlation is explained by Eq. (8).

d. Surface wind speed

If one has an estimate of the surface pressure gradient, one ought to be able to estimate the surface wind speed. Our simple approach to this problem is the following. Although surface pressure in tropical cyclones is nearly symmetric about the center (Frank, 1977), wind speeds are notoriously asymmetric. Most of that asymmetry at radii $\geq 1°$, however, can be explained by the motion of the storm (George and Gray, 1976). Therefore, we assumed that at gradient level (~85 kPa) the relative winds

[3] See Kidder (1979) for a demonstration that on space scales of 100 km the hydrostatic equation is valid in tropical storms.

(storm motion subtracted) were symmetric and to a close degree in gradient balance,[4] i.e.,

$$\frac{V_G^2}{r} + fV_G = RT_G \frac{\partial \ln p_s}{\partial r}, \quad (10)$$

where V_G is the relative wind speed at gradient level, r the radius, R the gas constant, T_G the temperature at gradient level, f the Coriolis parameter, and p_s the surface pressure. The surface pressure has been substituted for the pressure at gradient level because, by the hydrostatic equation, the radial gradient of the logarithms of the two pressures will be identical if the radial gradient of temperature between the two levels is small, which is the case (Fig. 1). Substituting from Eq. (8) yields

$$\frac{V_G^2}{r} + fV_G = -ART_G \frac{\partial T_B}{\partial r}. \quad (11)$$

Eq. (11) relates relative wind speed at gradient level to satellite-observed brightness temperature gradients.

If satellite data were noise-free, one could take any two brightness temperature observations near a tropical cyclone and estimate the gradient level wind speed between them from Eq. (11). Unfortunately, the SCAMS instrument has about ±0.5 K noise equivalent brightness temperature which would result in extremely noisy winds. It is therefore desirable to smooth the data before calculating the winds. One way to accomplish this smoothing is to assume a functional form for wind speed with radius. A suitably simple function proposed by Hughes (1952), Riehl (1954, 1963), and others is

$$V = Cr^{x}. \quad (12)$$

The exponent x would be 1 for parcels conserving their angular momentum. Near the surface where friction is large, x is near 0.5 (Riehl, 1963; Gray and Shea, 1973). The effect of changing x will be discussed later. Inserting Eq. (12) in Eq. (11) and integrating with respect to r holding C, x, f, A and T_G constant, gives

$$T_B = (ART_G)^{-1}\left(C^2\frac{r^{2x}}{2x} + fC\frac{r^{1+x}}{1+x}\right) + T_c, \quad (13)$$

where T_c is an integration constant. Given a field of satellite-measured brightness temperature around a tropical cyclone, one can average the temperatures in radial bands about the storm center (an additional smoothing technique) and calculate the C which gives the best least squares fit to the data. This C is the real, positive root[5] of

$$\frac{1}{x^2}\left[\sum r^{4x} - \frac{1}{N}(\sum r^{2x})^2\right]C^3 - \frac{3f}{x(1+x)}\left[\sum r^{1+3x} - \frac{1}{N}(\sum r^{2x})(\sum r^{1+x})\right]C^2 + \left\{\frac{2f^2}{(1+x)^2}\left[\sum r^{2+2x} - \frac{1}{N}(\sum r^{1+x})^2\right] - \frac{2}{x}\left[\sum yr^{2x} - \frac{1}{N}(\sum y)(\sum r^{2x})\right]\right\}C + \frac{2f}{1+x}\left[\sum yr^{1+x} - \frac{1}{N}(\sum y)(\sum r^{1+x})\right] = 0, \quad (14)$$

where $y = ART_GT_B$.

One additional parameter is necessary. We used a simple shearing parameter to relate the surface wind speed to the wind speed at gradient level, i.e.,

$$V_s = \mu V_G. \quad (15)$$

Based on the work of Bates (1977) and Gray and Frank (1978), 0.7 was chosen as the value of μ. Because wind speeds above gradient level change slowly in comparison with those below gradient level (Frank, 1977; Bates, 1977), accurate knowledge of the height of the gradient level is not required.

The SWIM technique for estimating surface wind speeds from satellite-observed brightness temperatures can then be summarized as follows:

1) Average the brightness temperatures in radial bands about the storm center. [We used 56 km (½°) bands.]

2) Choose an appropriate value of x (see next section).

3) Calculate C with Eq. (14).

4) Calculate surface wind speeds using Eqs. (12) and (15).

5) Add the storm motion to the relative winds to obtain the asymmetric wind field.

The technique was tested using, first, simulated satellite data constructed from temperature, pressure and height data measured by hurricane reconnaissance aircraft, and second, using 55.45 GHz SCAMS data.

3. Results

a. Aircraft data

Although satellite data are prevalent over tropical cyclones, one invariably finds that the number of cases in which one has both satellite data and ground truth data is extremely small. Also ground

[4] This assumption is not true at the surface where friction is large. Surface wind speeds will be derived from gradient level wind speeds by a simple parameterization of frictional effects.

[5] It is observed that Eq. (14) has only one real, positive root, the other two are generally real and negative, although they are sometimes complex conjugates. Occasionally for weak storms, no positive real root is found.

TABLE 2. Summary of aircraft reconnaissance data from hurricanes used in this study.

Storm	Date	Flight levels (kPa)	Intensity change
Cleo	18 Aug 1958	80, 56, 24	Steady
Helene	26 Sep 1958	80, 56, 25	Deepening
Hilda	1 Oct 1964	90, 75, 65, 50, 18	Deepening
Hilda	2 Oct 1964	90, 70, 65, 20	Filling
Inez	28 Sep 1966	95, 75, 65, 50, 20	Deepening

resolution of microwave data is rather coarse—145 km at nadir for SCAMS, for example. For these reasons, we decided to first test the SWIM technique using simulated satellite data which had good ground truth data and high spatial resolution. Aircraft reconnaissance data collected for the National Hurricane Research Project (Gray and Shea, 1976) were utilized for this simulation. The data were screened for the following criteria: 1) There had to be at least three flight levels; 2) one of the flights had to be near the level of maximum warming (25–30 kPa); and 3) one of the flight levels had to be near the surface to measure low-level winds. Between 1957 and 1969 there were five days (four storms) on which such data were taken (Table 2).

The satellite data were simulated as follows. At each 4.6 km (2.5 n mi) radial grid point, smoothed vortex-averaged values of temperature, pressure and height (at the lowest flight level) from Gray and Shea (1976) and relative humidities from the mean hurricane environment (Kidder, 1979) were used to construct soundings. Between flight levels, the equivalent potential temperature was assumed to vary linearly with pressure (LaSeur and Hawkins, 1963), and above the uppermost flight level, the mean environmental sounding was used. Finally, 55.45 GHz brightness temperatures were calculated, from Eq. (2), for each grid point. The result was simulated, vortex-averaged, 55.45 GHz satellite data with a spatial resolution of 4.6 km (2.5 n mi).

Simulated data outside of the radii of maximum wind were inserted into Eq. (14) to calculate C for $x = 0.5$ and $A = 1.02 \times 10^{-2}$ K^{-1}. The offset T_c was also calculated, and the simulated brightness temperatures along with the best-fit line from Eq. (13) are shown in Fig. 3. It can be seen, particularly in the case of Inez, that Eq. (13) fits the data well. The wind speeds at gradient level (~85 kPa) were then calculated with Eq. (12), and they are compared with the observed, vortex-averaged wind speed at the lowest flight level (Fig. 4). With the exception of Hilda on 2 October 1964, the agreement between observed and calculated wind speeds is excellent with rms errors of 2–3 m s^{-1}.

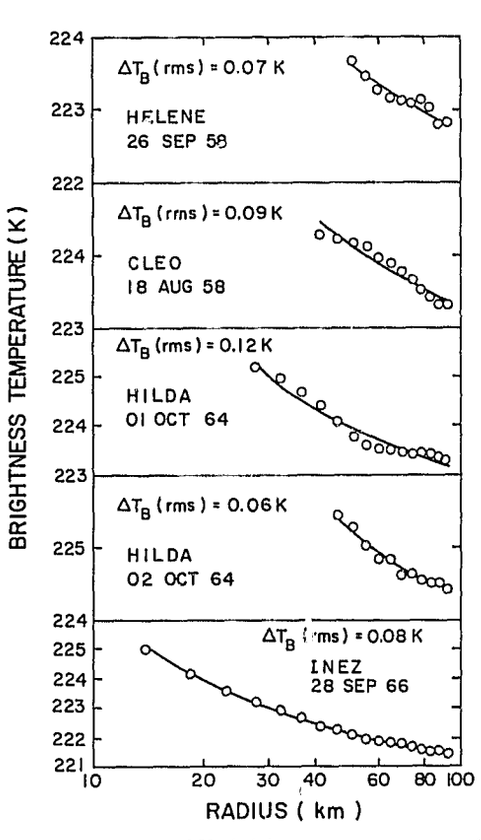

FIG. 3. Calculated 55.45 GHz brightness temperatures (circles) and best fit line for four hurricanes.

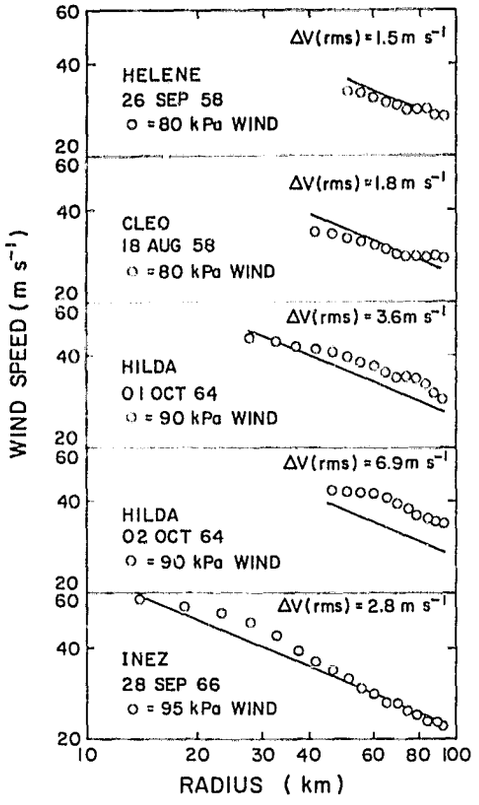

FIG. 4. Calculated gradient level (~85 kPa) wind speeds (line) and observed low-level wind speeds (circles) for four hurricanes (note that both scales are logarithmic).

TABLE 3. Typhoons used in this study (all 1975).

Name	Peak intensity (m s^{-1})	Date/time (GMT) of peak intensity	Minimum sea level pressure (kPa)	Central location at time of peak intensity (°N)	(°E)
June	82	19 Nov/1200	87.5	13.2	141.0
Phyllis	62	14 Aug/1800	92.5	24.1	137.1
Rita	41	22 Aug/1200	—	32.9	134.4
Tess	49	4 Sep/1800	94.5	23.0	147.6
Winnie	33	10 Sep/0600	—	31.0	162.8
Alice	39	17 Sep/1200	97.3	15.4	132.1
Betty	49	22 Sep/0000	94.7	22.6	123.6
Cora	54	4 Oct/1800	94.3	30.3	133.2

The case of Hilda on 2 October 1964 is interesting because it is the only filling storm. It is possible that storm temperature structure is different enough in later stages that A should have a different value. It is also possible that the process of constructing soundings mentioned above failed to detect the true magnitude of the upper level temperature anomaly. This may have caused the calculated brightness temperature gradient, and thus the calculated winds, to be too low. More research is needed to adequately resolve this problem.

In summary, it appears that with 4–5 km resolution, low-noise satellite data, one could accurately deduce low-level tropical cyclone wind speeds. We next attempted to estimate wind speeds using Nimbus 6 SCAMS data.

b. Nimbus 6 data

In our previous study (Kidder *et al.*, 1978), we had collected 116 Nimbus 6 SCAMS images of hurricanes and typhoons during 1975. These images were screened to meet two criteria: 1) the scan angle to the storm center had to be less than or equal to 21.6°, and 2) an independent estimate of the radius of 15.4 m s^{-1} (30 kt) wind had to be available. Only 20 images met both criteria, and only one of these was in the Atlantic; the remainder were Pacific typhoons. To make the data set more uniform, Tropical Storm Gladys (the only Atlantic storm) was eliminated, leaving 19 images of eight typhoons (Table 3). This is a rather small data set but it is large enough to indicate the potential of the SWIM technique.

Before calculation of the wind speeds, the 55.45 GHz brightness temperatures were corrected for scan angle with an additive correction developed by Rosenkranz *et al.* (1978). The center of the storm was chosen as the maximum brightness temperature within 145 km (one scan spot) of the interpolated best track center (1975 Annual Typhoon Report). The brightness temperatures were then azimuthially averaged in 56 km (0.5° latitude) bands from 111 km (1°) to 778 km (7°). The brightness temperature in the very center of the storm was not used in the fitting process. Eq. (14) was used to calculate C for $x = 0.5$, $A = 0.95 \times 10^{-2}$ K^{-1} and $T_G = 17.2$°C. Finally, the radii of 15.4 m s^{-1} (30 kt) and 25.7 m s^{-1} (50 kt) winds were calculated using $\mu = 0.7$ to estimate surface wind speeds. These calculations are compared with observations in Fig. 5.

The observed radii were taken from logs kept at the Joint Typhoon Warning Center on Guam. Each 6 h the forecaster on duty estimates the radii of 30, 50 and 100 kt winds using all available data. There are two problems with these observations. First, they are not coincident in time with the satellite image. The observational values plotted in Fig. 5 have been averaged both around the storm and over the two 6 h estimates between which the satellite observation was made. Second, the observations are subjective estimates which introduces some variance and a bias. Because safety is the prime concern, the observations tend to be overestimates. The average value of this error is unknown.

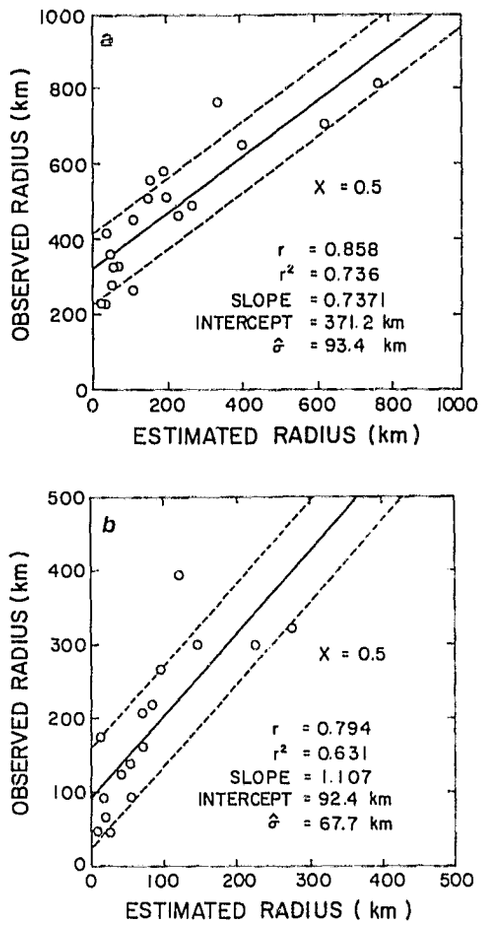

FIG. 5. Observed versus estimated average radius of (a) 15.4 m s^{-1} (30 kt) and (b) 25.7 m s^{-1} (50 kt) winds in eight typhoons during 1975 for $x = 0.5$.

The regression lines in Fig. 5 explain 63 and 74% of the variance for 25.7 m s^{-1} (50 kt) and 15.4 m s^{-1} (30 kt) winds, respectively. The standard errors of estimate are 68 and 93 km, respectively, which are reasonably good, and which may be influenced by the nature of the observed values. The intercepts are rather large, but some of this error is accounted for by the natural overestimation in the observed radii discussed above.

If the theory is correct, the slopes of the regression lines should be near 1. The fact that the slope for the radius of 15.4 m s^{-1} wind is somewhat less than 1 leads to speculation on the best value for the exponent x in the wind speed profile. Within 100 km of the storm center, 0.5 is a reasonable value for x, but Malkus and Riehl (1959) suggest that between 200 and 500 km x should be 0.6 to 0.7. Even though very few data points were available, an analysis was done to determine the effects of changing x.

Table 4 shows the square of the regression coefficient, the standard error of estimate, the slope and the intercept of the regression lines as functions of x. In general, increasing x slightly increases the fraction of explained variance, increases the slope, decreases the intercept and slightly decreases the standard error of estimate. For the radius of 25.7 m s^{-1} winds, an x in the range 0.4–0.5 produces the desired slope near 1.0. For the radius of 15.4 m s^{-1} winds, however, it appears that an x in the range 0.6 to 0.7 is a better choice. Fig. 6 shows the effect of changing x to 0.7. A better fit seems to be achieved for the radius of 15.4 m s^{-1} winds, but the opposite is true for the radius of 25.7 m s^{-1} winds. It appears, then, that for calculating the radius of 15.4 m s^{-1} (30 kt) winds by the SWIM technique one should use $x = 0.7$, but for the radius of 25.7 m s^{-1} (50 kt) winds one should use $x = 0.5$.

The 10% uncertainty in A causes approximately a 6–7% uncertainty in the wind speeds. The resultant uncertainty in the radius of a particular wind speed is the latter figure divided by x, i.e., a 13% uncertainty for $x = 0.5$ and a 10% uncertainty for $x = 0.7$. A better knowledge of the coefficient A would allow more accurate determinations of wind speed.

TABLE 4. Variation of regression statistics as a function of x.

x	r^2	Intercept (km)	$\hat{\sigma}$ (km)	Slope
	Radius of 15.4 m s^{-1} (30 kt) wind			
0.4	0.680	349	103	0.551
0.5	0.736	317	93	0.737
0.6	0.771	285	86	0.915
0.7	0.801	251	81	1.090
0.8	0.820	217	77	1.265
	Radius of 25.7 m s^{-1} (50 kt) wind			
0.4	0.579	111	72	1.058
0.5	0.631	92	68	1.107
0.6	0.663	74	65	1.165
0.7	0.685	55	63	1.231
0.8	0.701	36	61	1.305

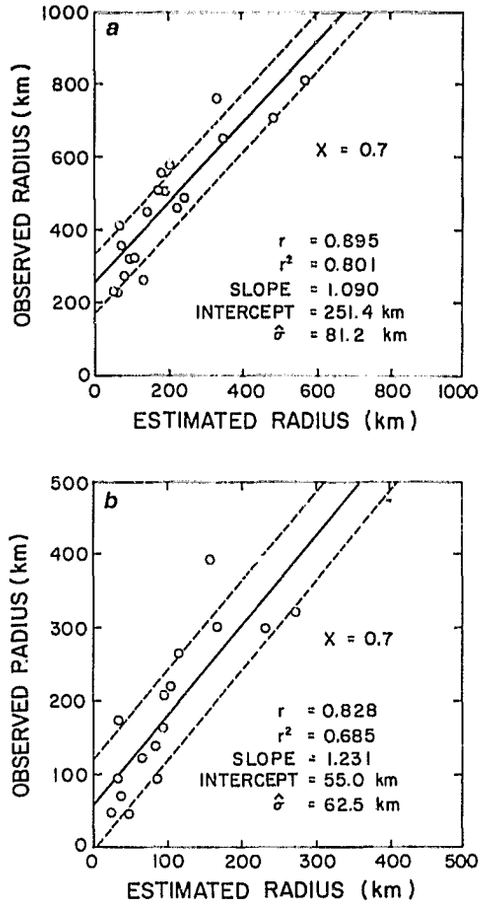

FIG. 6. As in Fig. 5 except for $x = 0.7$.

4. Conclusions

From Figs. 5 and 6, it appears that the SWIM technique is currently capable of estimating the radius of 15.4 m s^{-1} (30 kt) wind to within about ±80 km and the radius of 25.7 m s^{-1} (50 kt) wind to within about ±70 km. These results are promising, and indicate that further research is required.

The SWIM technique should be tried using TIROS-N and NOAA 6 data for several reasons. First, the MSU is a more sensitive instrument for estimating surface pressure gradients than was the SCAMS. The peak of the 54.96 GHz channel weighting function is closer to the peak of the temperature anomaly than the peak of the 55.45 GHz SCAMS weighting function (Fig. 2). Also, the 57.95 GHz channel could be used to measure the cooling above the storm. A two-parameter estimation of the sur-

face pressure anomaly of the form

$$\Delta \ln p_s = A\Delta T_{B_1} + B\Delta T_{B_2} \qquad (16)$$

should be more accurate than a single-parameter estimation. Second, since the launch of NOAA 6 there are four images per day of tropical cyclones, about half of which pass closely enough to the storm center on the average to apply the SWIM technique. And finally, the TIROS-N/NOAA series are the current operational satellites from which microwave data are routinely processed in near real time. This technique is also suitable for use with the microwave sounder on board the new DMSP satellite, and further testing may be done with those data.

In summary, we think that the microwave technique described in this paper, which we have called the SWIM technique, has the potential to become a valuable tool at the disposal of the forecaster.

Acknowledgments. The authors would like to thank Sam Brand of the Naval Environmental Prediction Research Facility and David Sokol of the Joint Typhoon Warning Center for supplying data on the typhoons of 1975, and Hans J. Liebe of the U.S. Department of Commerce Office of Telecommunications for a computer program to calculate atmospheric transmittances. This research was sponsored by the National Aeronautics and Space Administration under Grant NSG-5258.

REFERENCES

Bates, J., 1977: Vertical shear of the horizontal wind speed in tropical cyclones. NOAA Tech. Memo. ERL WMPO-39, Miami, 19 pp.

Dvorak, V. F., 1975: Tropical cyclone intensity analysis and forecasting from satellite imagery. *Mon. Wea. Rev.*, **103**, 420–430.

Frank, W. M., 1977: The structure and energetics of the tropical cyclone I. Storm structure. *Mon. Wea. Rev.*, **105**, 1119–1135.

George, J. E., and W. M. Gray, 1976: Tropical cyclone motion and surrounding parameter relationships. *J. Appl. Meteor.*, **15**, 1252–1264.

Gray, W. M., and D. J. Shea, 1973: The hurricane's inner core region. II. Thermal stability and dynamic characteristics. *J. Atmos. Sci.*, **30**, 1565–1576.

——, and ——, 1976: Data summary of NOAA's hurricane inner-core radial leg flight penetrations 1957–1967, and 1969. Atmos. Sci. Pap. 257, Colorado State University, Ft. Collins, 219 pp.

——, and W. M. Frank, 1978: New results of tropical cyclone research from observational analysis. Naval Environmental Prediction Research Facility, Tech. Rep. TR-78-01, Monterey, 106 pp.

Grody, N. C., 1976: Remote sensing of atmospheric water content from satellites using microwave radiometry. *IEEE Trans. Antennas Propag.*, **AP-24**, 155–162.

——, C. M. Hayden, W. C. C. Shen, P. W. Rosenkranz and D. H. Staelin, 1979: Typhoon June winds estimated from scanning microwave spectrometer measurements at 55.45 GHz. *J. Geophys. Res.*, **84**, 3689–3695.

Hawkins, H. F., and D. T. Rubsam, 1968: Hurricane Hilda, 1964 II. Structure and budgets of the hurricane on October 1, 1964. *Mon. Wea. Rev.*, **96**, 617–636.

——, and S. M. Imbembo, 1976: The structure of a small intense hurricane—Inez, 1966. *Mon. Wea. Rev.*, **104**, 418–442.

Hughes, L. A., 1952: On the low level wind structure of tropical cyclones. *J. Meteor.*, **9**, 422–428.

Jelesnianski, C. P., and A. D. Taylor, 1973: A preliminary view of storm surges before and after storm modifications. NOAA Tech. Memo. ERL WMPO-3, 33 pp.

Jones, L. W., P. G. Black, D. M. Boggs, E. M. Bracalente, R. A. Brown, G. Dome, J. A. Ernst, I. M. Halberstam, J. E. Overland, S. Peterherych, W. J. Pierson, F. J. Wentz, P. M. Woiceshyn and M. G. Wurtele, 1979: Seasat scatterometer: Results of the Gulf of Alaska workshop. *Science*, **204**, 1413–1415.

Kidder, S. Q., 1979: Determination of tropical cyclone surface pressure and winds from satellite microwave data. Atmos. Sci. Pap. No. 307, Colorado State University, Ft. Collins, 87 pp.

——, W. M. Gray and T. H. Vonder Haar, 1978: Estimating tropical cyclone central pressure and outer winds from satellite microwave data. *Mon. Wea. Rev.*, **106**, 1458–1464.

LaSeur, N. E., and H. F. Hawkins, 1963: An analysis of Hurricane Cleo (1958) based on data from research reconnaissance aircraft. *Mon. Wea. Rev.*, **91**, 694–709.

Liebe, H. J., and G. G. Gimmestad, 1978: Calculation of clear air EHF refractivity. *Radio Sci.*, **13**, 245–251.

——, G. G. Gimmestad and J. D. Hopponen, 1977: Atmospheric oxygen microwave spectrum—experiment versus theory. *IEEE Trans. Antennas Propag.*, **AP-25**, 327–335.

Lipes, R. G., R. L. Bernstein, V. J. Cardone, K. B. Katsaros, E. J. Njoku, A. L. Riley, D. B. Ross, C. T. Swift and F. J. Wentz, 1979: Seasat Scanning Multichannel Microwave Radiometer: Results of the Gulf of Alaska workshop. *Science*, **204**, 1415–1417.

Malkus, J. S., and H. Riehl, 1959: On the dynamics and energy transformations in steady-state hurricanes. National Hurricane Research Project Rep. No. 31, Washington, DC, 31 pp.

Núñez, E., and W. M. Gray, 1977: A comparison between West Indies hurricanes and Pacific typhoons. *Postprints 11th Tech. Conf. Hurricanes and Tropical Meteorology*, Miami, Amer. Meteor. Soc., 528–534.

Rodgers, E. B., R. C. Gentry, W. Shenk and V. Oliver, 1979: The benefits of using short-interval satellite images to derive winds for tropical cyclones. *Mon. Wea. Rev.*, **107**, 575–584.

Riehl, H., 1954: *Tropical Meteorology*. McGraw-Hill, 392 pp.

——, 1963: Some relations between wind and thermal structure of steady-state hurricanes. *J. Atmos. Sci.*, **20**, 276–387.

Rosenkranz, P. W., and D. H. Staelin, 1976: Summary of operations: The scanning microwave spectrometer (SCAMS) experiment. *The Nimbus 6 Data Catalog*, Vol. 3, NASA/Goddard Space Flight Center, Greenbelt, 1–2 through 1–4.

——, —— and N. C. Grody, 1978: Typhoon June (1975) viewed by a scanning microwave spectrometer. *J. Geophys. Res.*, **83**, 1857–1868.

Staelin, D. H., A. H. Barrett, P. W. Rosenkranz, F. T. Barath, E. J. Johnson, J. W. Waters, A. Wouters and W. B. Lenoir, 1975a: The scanning microwave spectrometer (SCAMS) experiment. *The Nimbus 6 User's Guide*, NASA/Goddard Space Flight Center, Greenbelt, 59–86.

——, A. L. Cassel, K. F. Kunzi, R. L. Pettyjohn, R. K. L. Poon and P. W. Rosenkranz, 1975b: Microwave atmospheric temperature sounding: Effects of clouds on the Nimbus 5 satellite data. *J. Atmos. Sci.*, **32**, 1970–1976.

Staff, Joint Typhoon Warning Center, 1975: 1975 Annual Typhoon Report. Joint Typhoon Warning Center, COMNAVMARIANAS Box 12, FPO, San Francisco, 75 pp.

Forecasting Tropical Cyclone Turning Motion from Surrounding Wind and Temperature Fields

JOHNNY C. L. CHAN, WILLIAM M. GRAY AND STANLEY Q. KIDDER[1]

Department of Atmospheric Science, Colorado State University, Fort Collins 80523

(Manuscript received 30 July 1979, in final form 31 January 1980)

ABSTRACT

An analysis of tropical cyclone forecast track errors shows that the largest errors are typically associated with storms undergoing turning motion. This paper presents results obtained from a composite study of tropical cyclones occurring in the West Indies during 1961–77. Storms which underwent a left or right turn or moved straight for a period of at least 36 h were studied. Wind fields at different levels in the atmosphere around these storms were investigated.

When a storm begins to turn, the environmental flow at 500 mb and the average tropospheric wind (between 200 and 900 mb) around the cyclone at 5–11° latitude radius is cyclonic for a left turning and anticyclonic for a right turning storm. At 24–36 h before a storm makes a left turn, there exists a large positive vertical wind shear around the cyclone between the upper (200 mb) and lower (900 mb) troposphere in the direction of storm motion, while the opposite occurs with a right-turning storm. Straight-moving cyclones do not show such a shear pattern. Statistical tests show that these results are significant at the 95% level or higher.

Tropospheric mean temperature fields around 13 tropical cyclone turning cases in the Atlantic and Pacific Oceans derived from the Nimbus 6 microwave sounder data during 1975 were also studied. Temperature gradients across these storms indicate (through the thermal wind relationship) vertical wind shear profiles similar to those obtained from the composite.

These results suggest or verify previous ideas that 1) by measuring certain parameters around a storm (sense of surrounding wind rotation, vertical wind shear between 200 and 900 mb, or gradient of tropospheric mean temperature) one may be able to make a better 24–36 h forecast of cyclone turning motion; 2) the turning motion of tropical cyclones is controlled by large-scale flow fields surrounding them; and 3) there seems to be a time lag between the changes in the environment and the response of the storm center to such changes.

1. Introduction

To predict the turning motion of tropical cyclones 24–36 h in advance is very difficult and quite often unsuccessful. Statistical prediction schemes (e.g., Hope and Neumann, 1970; Neumann and Lawrence, 1975) have great problems in forecasting such turning motion because of their strong emphasis on climatology and persistence. Numerical models also fail to predict cyclone turning motion most of the time. As a result, the largest tropical cyclone track forecast errors[1] are usually associated with storms undergoing a turn.

A detailed study of the characteristics of the surrounding environment of cyclones undergoing turning motion may give insight into ways of devising new schemes which may reduce forecast errors associated with turning motion. This paper presents information on the environmental flow patterns around tropical cyclones prior to and at the time when these storms undergo turning motion. It will be shown that significant differences in the large-scale surrounding wind fields exist at 500 mb, and also at 200 and 900 mb levels between left-turning, straight-moving and right-turning storms. Temperature sounding data from the Nimbus 6 Scanning Microwave Spectrometer also provide evidence of some of these differences.

2. Forecast errors associated with turning motion

To examine this forecast problem more closely, a special study of tropical cyclone forecast errors occurring in the West Indies during the period 1961–77 was made.

a. Selection of cyclone tracks

The data sample consists of tropical cyclones in the West Indies west of 55°W with maximum sustained winds ≥ 18 m s^{-1}. The direction of

[1] Present affiliation: Laboratory for Atmospheric Research, University of Illinois at Urbana-Champaign, Urbana 61801.

[1] Forecast error is defined as the deviation of the forecast position of a tropical cyclone from its best-track verifying position.

0027-0644/80/060778-15$07.75

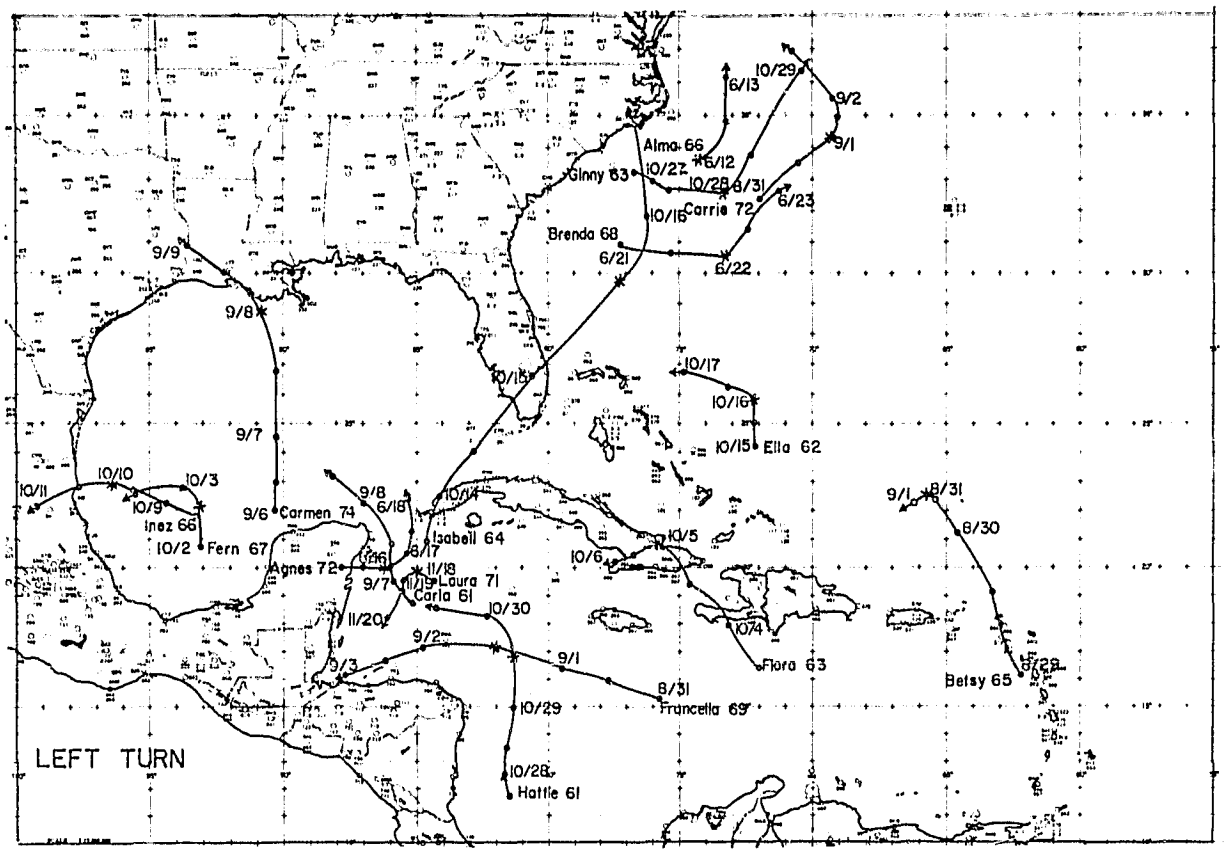

FIG. 1. Tracks of tropical cyclones used in this study which made a left turn. The asterisk on each track indicates the turn time T. The solid circle is the 0000 GMT position (with the date next to it) and the open circle is the 1200 GMT position.

motion (D) of each storm at a standard time T in hours (0000 or 1200 GMT) is defined as D(T). Three turn classes were then chosen according to the following criteria:

Left-turning: $D(T + 12) - D(T) < -20°$

Straight-moving: $-10° < D(T + 12) - D(T - 12) < 10°$

Right-turning: $D(T + 12) - D(T) > 20°$.

The time T was then defined as the turn time. In this way, 16 left-turning, 33 straight-moving and 28 right-turning cases were chosen. Tracks of these storms are shown in Figs. 1, 2 and 3.

b. Forecast errors of sample storms

The 24 h National Hurricane Center (NHC) official forecast errors issued for each storm at three time periods [24 h before turn time (T − 24), the turn time (T) and 24 h after turn time (T + 24)] were analyzed. Table 1 gives the average result for each turn class. The "special right turn" category consisted of cases where the average 24 h forecast error was greater than 350 km. It can be seen that a considerable jump in the forecast error occurs at turn time in comparison with the forecast error for straight-moving cyclones. The forecast errors are even larger for 16 of the 22 special right-turn cases, jumping from 148 km before the turn to 417 km at turn time.

Fig. 4 shows the scatter of 24 h forecast positions made at turn time and the corresponding verifying positions for each turn class. Table 2

TABLE 1. Average 24 h official tropical cyclone track forecast errors (km) issued by the National Hurricane Center, Miami. T is the time when the storm starts to turn. See text for further explanation of turn classification. Note that the number of analyzed cases are different from those mentioned in Section 2a because forecast errors for some cases are not available.

Turn classification	24-h Forecast error (km) for forecasts issued at the following times		
	T − 24	T	T + 24
Left turn (10 cases)	235	289	206
Straight (23 cases)	148	169	196
Right turn (22 cases)	178	324	239
Special right turn (16 cases)	148	417	245

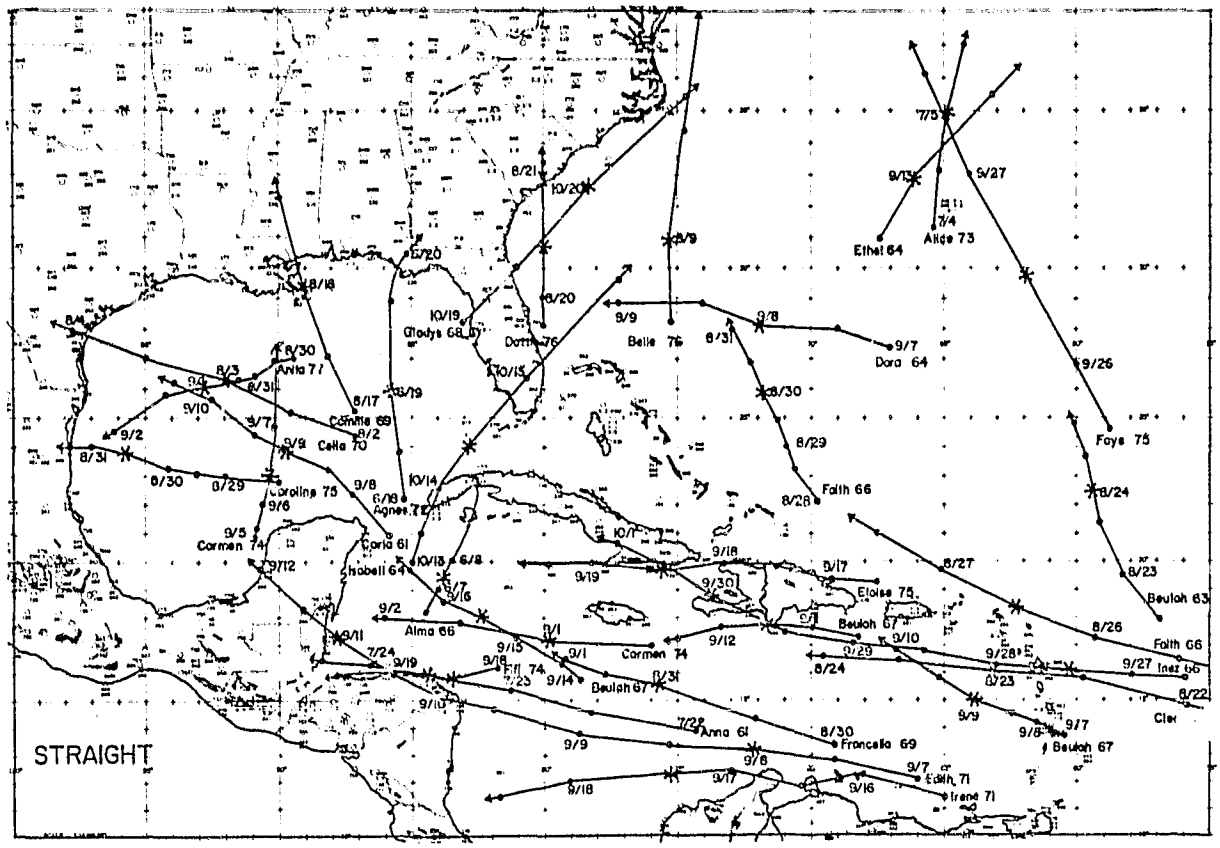

FIG. 2. As in Fig. 1 except for straight-moving tropical cyclones.

gives the average directional deviation of these forecast positions from the verifying positions and the extrapolated tracks. The forecast positions for right-turning storms are nearly always to the left of the actual storm track [Directional Deviation (DD) = −38°]. They also tend to cluster around the extrapolated position of the storm from its current path (DD = 2°). The strong bias based on persistence is evident. All forecast positions for left-turning storms are to the right of the actual track (DD = 50°). It is interesting to note that, on the average, the forecast actually calls for a right-turn (DD from extrapolated track is 21°). For straight-moving storms the forecast, verifying and extrapolated positions are nearly the same. Although there are natural limitations on the predictability of storm movement, it seems obvious that the skill of forecasting turning motion is not satisfactory. This is probably a result of insufficient observational knowledge of the characteristics of the cyclone's surrounding environmental flow patterns and their changes. It is apparent that more research on cyclone turning motion is needed.

TABLE 2. Directional deviation (DD) of the mean 24 h forecast position made at turn time from the mean verifying position and the mean extrapolated track. A positive number means the forecast position is to the right of the verifying position or the extrapolated track.

Turn classification	Directional deviation of forecast (deg)	
	From mean extrapolated track	From mean verifying position
Left turn	21	50
Straight	9	11
Right turn	2	−38

3. Data compositing

Because of the scarcity of oceanic rawinsonde data, representative information on the characteristics of surrounding flow patterns of individual tropical systems is usually very deficient. To overcome this severe data problem, a rawinsonde compositing approach was employed. This averages data from storm systems having similar turning characteristics. The rationale behind this type of data compositing has been discussed in a number of recent papers (e.g., Williams and Gray, 1973; Frank, 1977; and others). Composited data samples enable reliable quantitative analyses to be made, and allow meaningful

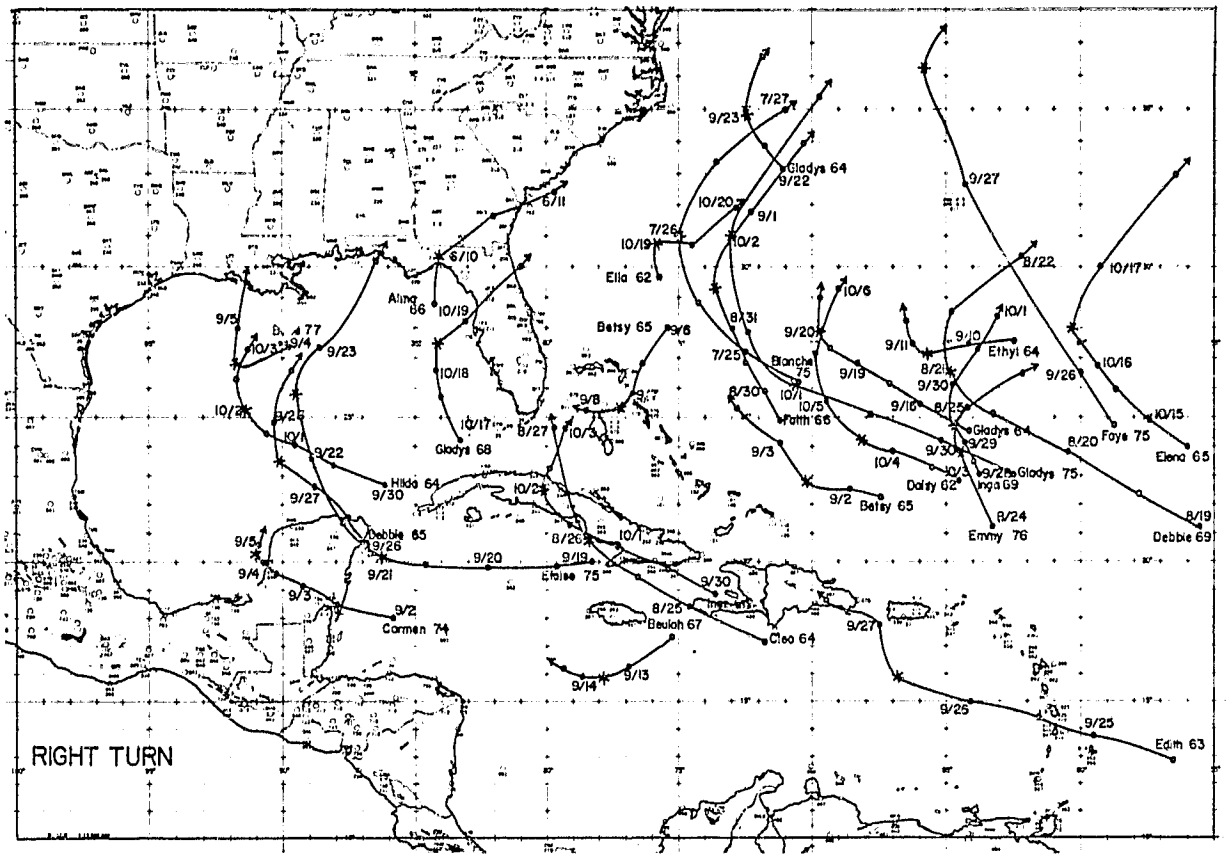

FIG. 3. As in Fig. 1 except for right-turning tropical cyclones.

conclusions to be drawn about the "average" differences in the surrounding environment between different data sets. Compositing tends to suppress random data noise and isolates mean characteristics common to each composite class. Differences between turning classes (if present) will give hints to forecasters as to which surrounding cyclone parameters to monitor in individual cases.

For each turn classification in Section 2a rawinsonde data at the following time periods were

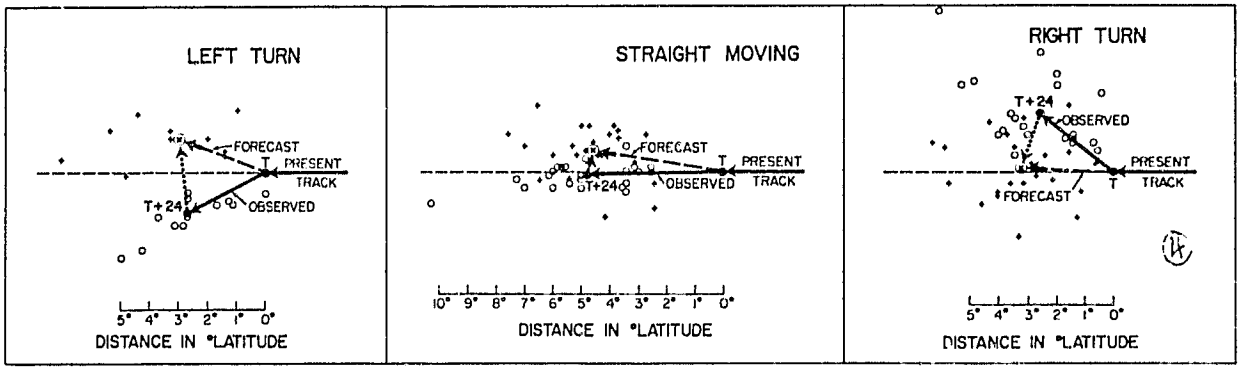

FIG. 4. National Hurricane Center 24 h forecast positions (denoted by +) made at the turn time for individual storms in each class and their actual positions (denoted by open circles) at the time T + 24. The ⊙ is the mean forecast position. The dashed arrow is the 24 h mean forecast track. The solid arrow from T to T + 24 is the mean distance (and direction) the storm has traveled during the 24 h. The dotted arrow indicates the average displacement of the forecast position from the actual position.

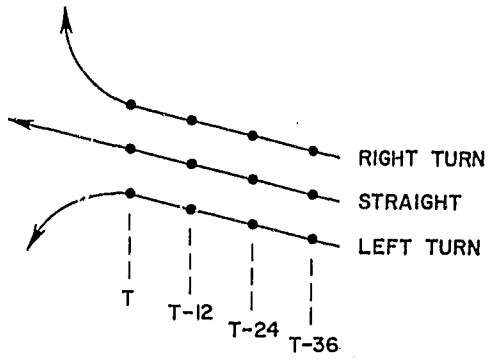

FIG. 5. Idealized picture of the three turn classes of tropical cyclones and of the time periods prior to turn which were composited.

composited: when the storm starts to turn (turn time, T), and 12, 24 and 36 h before turn time (T − 12, T − 24 and T − 36 respectively), as shown schematically in Fig. 5. Rawinsonde stations used in the data compositing are shown in Fig. 5.

Compositing is performed on a 15° latitude radius[2] cylindrical grid consisting of eight octants and eight radial bands, as shown in Fig. 7. The center of the grid corresponds to the storm center. The grid is rotated so that octant 1 is aligned along the direction of storm motion. See George and Gray (1976) for a more detailed description.

[2] Hereafter, all distances are referred to in degrees latitude (1° latitude = 111.1 km).

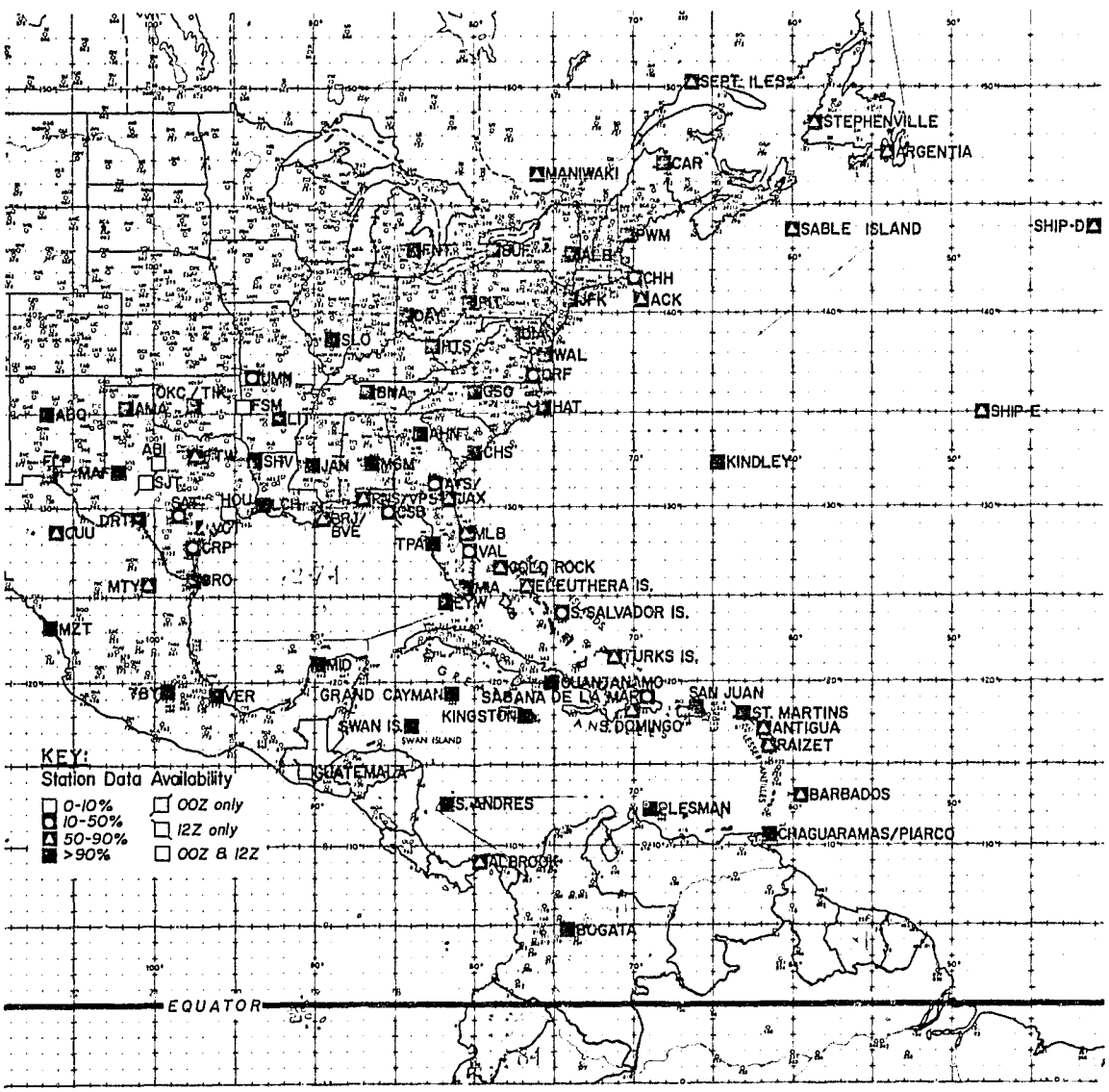

FIG. 6. Northwest Atlantic rawinsonde data network.

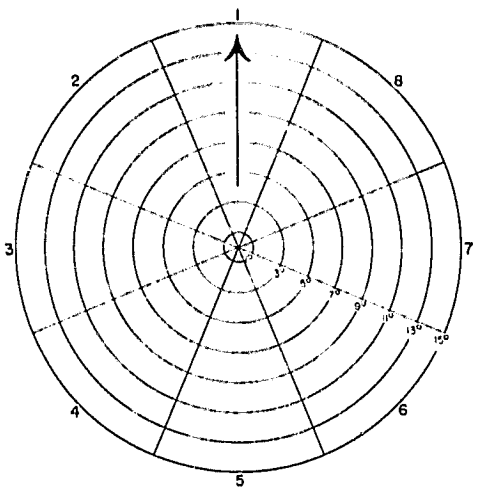

FIG. 7. Grid used for compositing rawinsonde data. The arrow points in the direction of storm motion. Outer numbers denote octants. Numbers inside grid indicate distances from the center in degrees latitude.

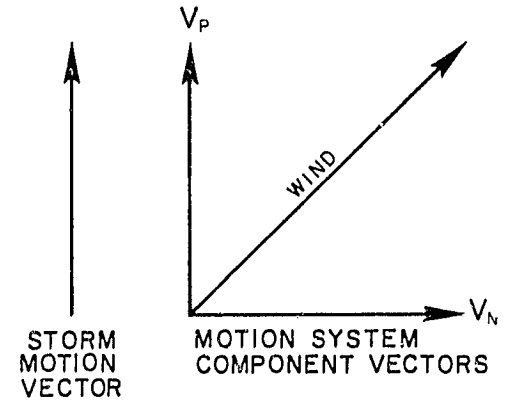

FIG. 8. Parallel (V_P) and perpendicular (V_N) components of a wind vector showing their relation to the storm motion vector.

Each wind vector is resolved into two components, one parallel to the direction of storm motion (V_P) and one normal to it (V_N), as shown in Fig. 8. All wind observations falling within a particular octant and radial band are averaged to give the composite V_P and V_N within that sector. These types of rawinsonde averaging processes are described in greater detail by Frank (1977).

4. Surrounding flow at turn time

It has been known for many years that tropical cyclone motion is well related to mid-tropospheric surrounding wind patterns. In a composite study of tropical cyclone motion stratified according to direction, latitude, speed, intensity and intensity change, George and Gray (1976) found that 500 mb is the best steering level for direction and 700 mb is the best for cyclone speed. To better refine the present knowledge of the steering flow associated with cyclones undergoing turning motion, composite flow fields at 900, 700, 500 and 200 mb at turn time were analyzed. Although 500 mb is found to be the best steering level, flow fields at the upper (200 mb) and lower (900 mb) tropospheric levels also appear quite useful.

a. Flow field at 500 mb

Fig. 9 shows the composited 500 mb streamline patterns at turn time for the three turning classes. The flow field ahead of the storm can be seen to be a very good indicator of current directional change.

The V_N components of the winds at 500 mb in the front and back octants are shown in Fig. 10. The number next to each arrow indicates the magnitude of the V_N component (m s^{-1}) averaged between 5–11° radius. For each classification, if a weighted average of V_N in the front three and back three octants [V_N in octants 1 (front) and 5 (back) are given a

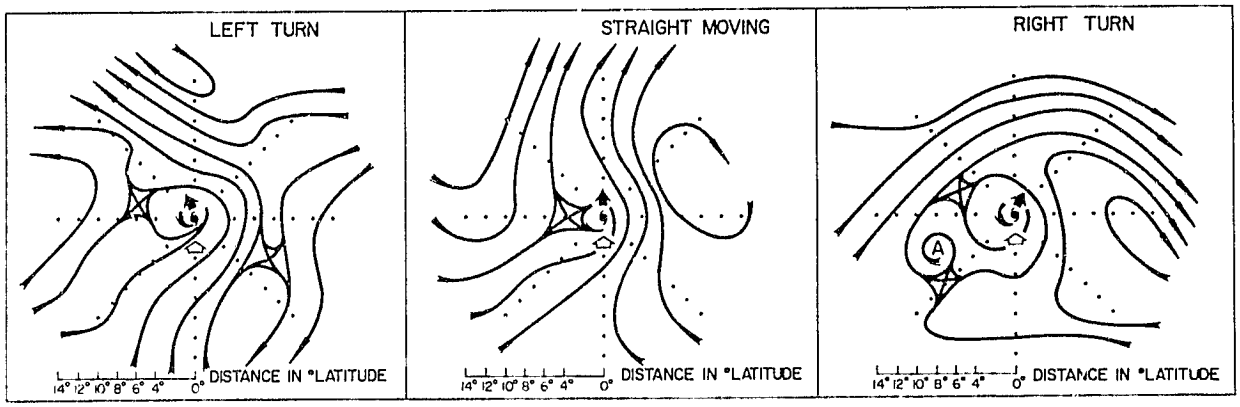

FIG. 9. 500 mb streamlines for the three turn classes at turn time. Open arrows indicate the instantaneous direction of storm motion. Solid arrows indicate the movement of the storm during the next 12 h.

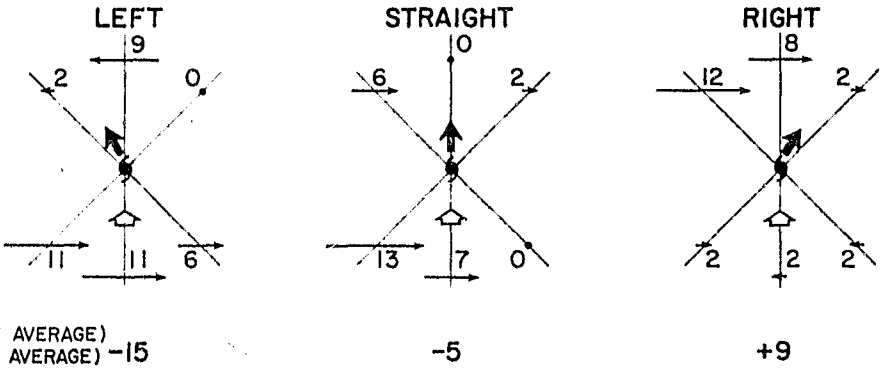

FIG. 10. Sum of V_λ [wind component (m s^{-1}) normal to direction of storm motion] at 500 mb within 5–11° radii from the storm center in various octants at the turn time T. The length of the arrow is proportional to the magnitude of the wind. See text for description of the averaging process. Open arrows indicate the instantaneous direction of storm motion and solid arrows the movement of the storm during the next 12 h.

weight of 1 and those in the right and left octants a weight of 0.5] is calculated, the front octant average minus the back octant average will give a horizontal V_N shear value. This is shown at the bottom of the figure. These shear values are significantly different between the three turn classes and they well infer turning motion at turn time.

With decreasing oceanic middle level rawinsonde and propeller aircraft data, such 500 mb level information on individual cyclone cases is usually not available. Since upper and lower tropospheric wind data are becoming more available with time from satellite and jet aircraft observations it may be more useful to try to establish steering flow relationships at upper and lower tropospheric levels.

b. Upper and lower tropospheric flow

The 5–11° radius average of the front and back octants V_N (200 mb) and V_N (900 mb) for the three turn classes at turn time is shown in Fig. 11. The differences in horizontal V_N shear values between turn classes follow the same trend as those at 500 mb. Thus, it seems possible to use the average 200 and 900 mb winds to infer turning motion at turn time.

5. Surrounding flow before turn time

A study of the composite V_N flow fields 24 or 36 h before turn time at various levels reveals no significant differences between the turn classes. The V_P component of the wind at 500 mb and the upper (200 mb) and lower (900 mb) troposphere, however, shows important relationships with cyclone turning motion 24–36 h before it takes place.

a. 500 mb flow

The V_P components of the winds (parallel to the direction of storm motion) at 500 mb in the front left (2), back left (4), back right (6) and front right (8) octants are found to best correlate with turning motion 24–36 h before turn time. These components

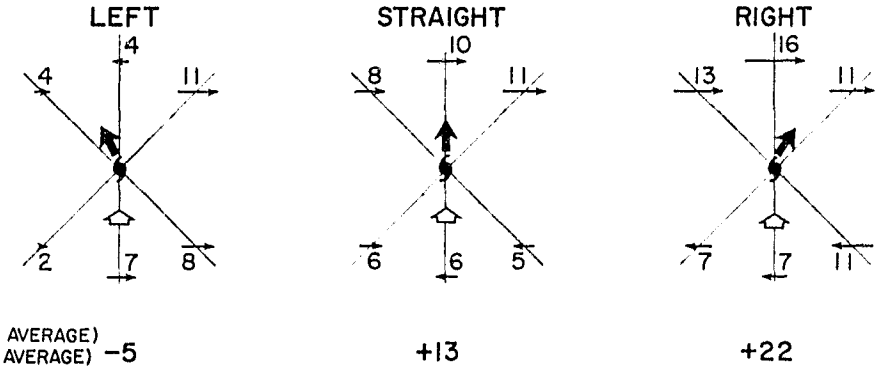

FIG. 11. As in Fig. 10 except V_λ is the sum of the average winds between 200 and 900 mb at the turn time (T).

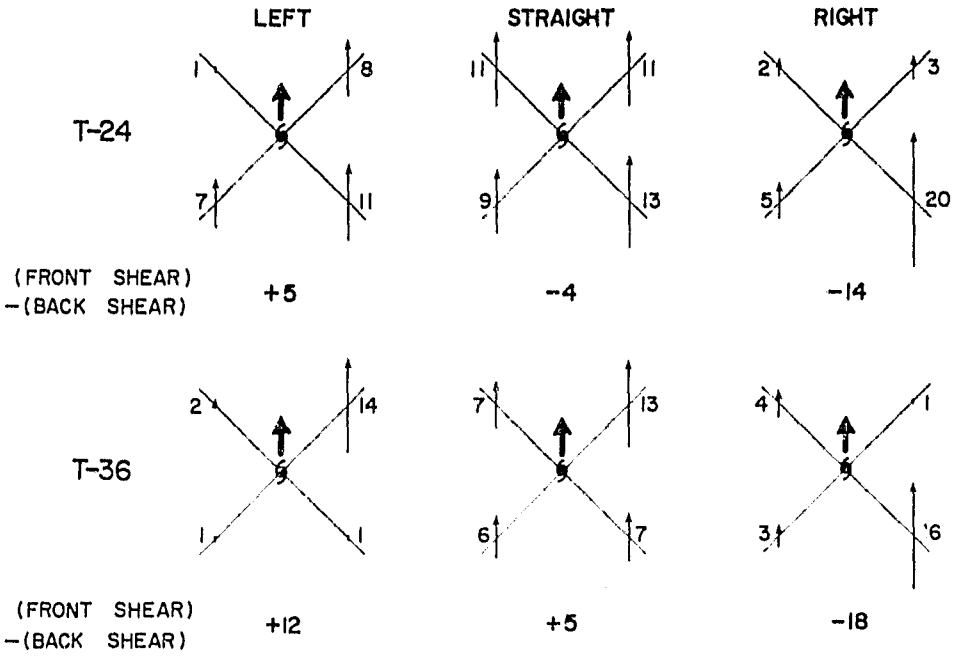

FIG. 12. Sum of 500 mb V_p [wind component (m s $^{-1}$) parallel to direction of storm motion] within 5–11° radii from the storm center in octants 2, 4, 6 and 8 for the three turn classes at 24 h (T − 24) and 36 h (T − 36) before turn time. The heavy arrow indicates the direction of storm motion. See text for description of calculating the front and back shear.

are shown in Fig. 12. At 24 h before turn time (T − 24), there exists at the front of the storm a strong cyclonic shear of V_p [V_p(right) − V_p(left)] for the left-turning storms. This shear is denoted by $\Delta V_p/\Delta n$, where Δn represents the distance between octants 2 and 8 or 4 and 6. This front V_p shear is about zero for the other two turn classes. Behind the cyclone, the right minus left V_p shear is cyclonic for all three classes. The magnitude of this V_p shear is largest for right-turning storms. Subtracting the V_p right minus left shear behind the storm from that in front of the storm, that is, $[(V_{p_8} - V_{p_2})/\Delta n - (V_{p_6} - V_{p_4})/\Delta n]$, where the numeric subscripts denote octant numbers, a front minus back V_p shear can be obtained which might be used to identify turning motion 24 h before it takes place: a positive value for left-turning, small negative for straight-moving and large negative value for right-turning.

At 36 h before turn time (T − 36) a similar difference in the front minus back V_p shear exists between the three turn classes, as indicated in the lower half of Fig. 12. Notice that the front minus back V_p shear for straight-moving storms at T − 36 is the same as that for left-turning storms at T − 24. This appears to reduce the distinguishing power of this shear to forecast turning. However, given the current low skill of forecasting turning motion, this 500 mb shear information may still be useful.

If aircraft reconnaissance flights were available to better measure these middle-level outer radius shear patterns, then an improvement in forecasting turning motion might result. Such aircraft reconnaissance requires special propeller aircraft capability and will likely be unavailable in many or most cyclone forecast situations. By contrast, satellite-derived winds in the upper and lower troposphere should be more easily available.

b. Upper and lower tropospheric flow

The component of the 200–900 mb vertical wind shear parallel to the direction of storm motion 24–36 h before turn time is significantly different between the three turn categories.

Fig. 13 shows the average V_p wind within 7–11° radius[3] from the storm center in octants 1 (front) and 5 (back) at 200 and 900 mb 24 h before the turn time (T − 24). In front of the storm, right-turning cyclones show a large negative wind shear between these two levels [V_p(200 mb)−V_p(900 mb)] while both left-turning and straight-moving storms have positive wind shear values. Behind the storm, the vertical wind shear is negative for straight-moving

[3] The reasons for using 7–11° are twofold: 1) since this flow is related to directional change of the storm 24–36 h ahead, one would expect this relation to be more significant further out from the storm center, where the environmental steering flow influences are much more dominant than that of the storm, and 2) the value of V_p in this radial band correlates best with the directional change of the storm.

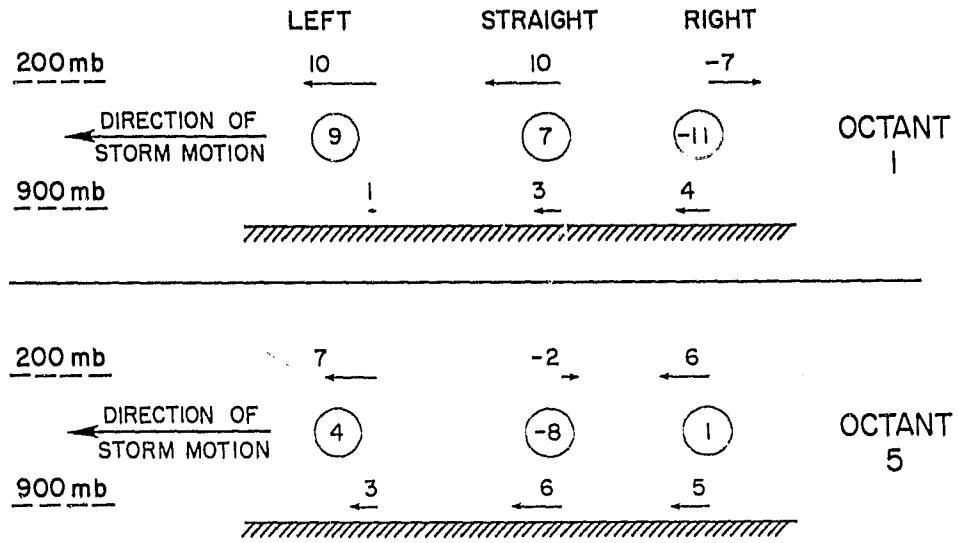

FIG. 13. Cross-sectional view of the average V_p wind components (m s^{-1}) at 200 and 900 mb within 7–11° radii from the storm center in octants 1 and 5 24 h before turn time (T − 24). The circled numbers are the values of the vertical wind shear [V_p(200 mb)− 00 mb)].

storms and slightly positive for the other two turn classes. The average front and back vertical wind shears in the direction of storm motion are 7, −1 and −6 m s^{-1} for left-, straight- and right-moving cyclones, respectively. The same shear values at T − 36 are 3, 0 and −10 m s^{-1} (see Fig. 14). Thus, for left-turning storms the net vertical wind shear in the direction of storm motion in octants 1 (front) and 5 (back) is positive. The shear is about zero for a straight-moving storm and negative for a right-turning storm.

Such differences in tropospheric vertical wind shear between the turn classes only exist 24 and 36 h prior to turn time (Fig. 15). This shear difference does not show up as the storm approaches its turn time. Wind shear values at T − 48 and before cannot be obtained because of the lack of cases.

Thus, if one is able to obtain winds in the upper

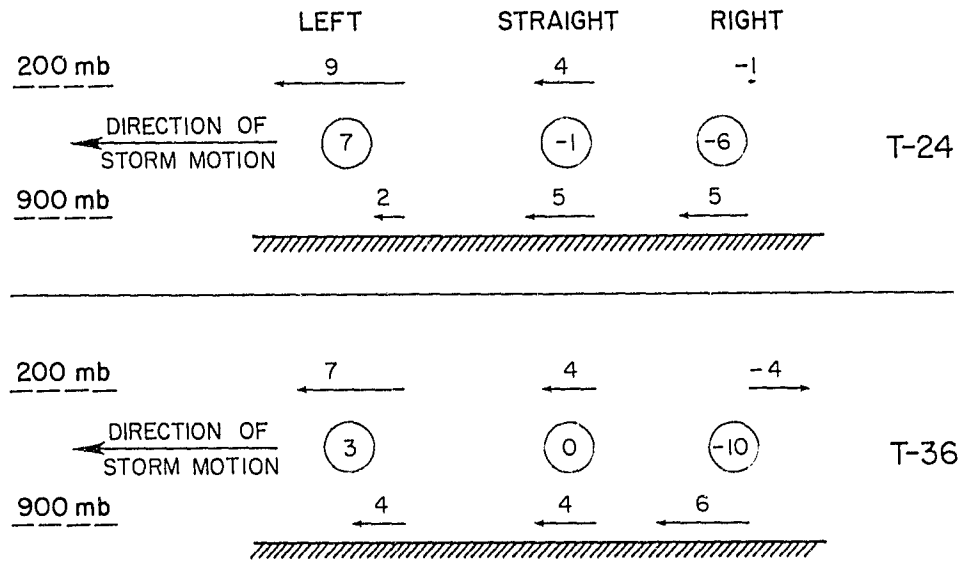

FIG. 14. Cross-sectional view of the sum of average V_p wind components (m s^{-1}) within 7–11° radii from the storm center in octants 1 and 5 at 200 and 900 mb at 24 h (T − 24) and 36 h (T − 36) before turn time for the three turn classes. The circled numbers are the values of the vertical wind shear [V_p(200 mb)−V_p(900 mb)].

and lower troposphere around a storm (for example, from satellite observations), it may be possible to better anticipate cyclone turning motion 24–36 h before it takes place.

c. Individual case analysis

To see how valid the composite results are for individual turning storms, the V_P vertical shear described in the previous section for individual cases in the sample was also studied. Individual case analysis is severely handicapped by data availability. Wind and height data must be interpolated from analyzed weather maps. Nevertheless, an attempt was made to evaluate this vertical shear parameter [V_P(200 mb)–V_P(900 mb)] for individual turning situations. The 200 mb winds were estimated from the height contours, using the geostrophic wind relationship. If there were no contour maps an estimate was made from the 200 mb streamline analysis. If neither was available, the case was not analyzed. The 900 mb winds were estimated from either the 3000 ft PIBAL maps or from the NHC ATOLL (top of the Ekman Layer) maps. If neither was available, an estimate was made from surface pressure maps, again using the geostrophic wind relationship. These methods restricted the analysis of the V_P vertical wind shear to only about two-thirds of the individual cases in the sample.

Fig. 16 shows the shear values obtained at both T − 24 and T − 36. Although there is a large spread in the vertical wind shear for each classification (which is to be expected because of the inherent data uncertainties) a relationship between the vertical wind shear and the turning motion, similar to the one in the composite, does show up.

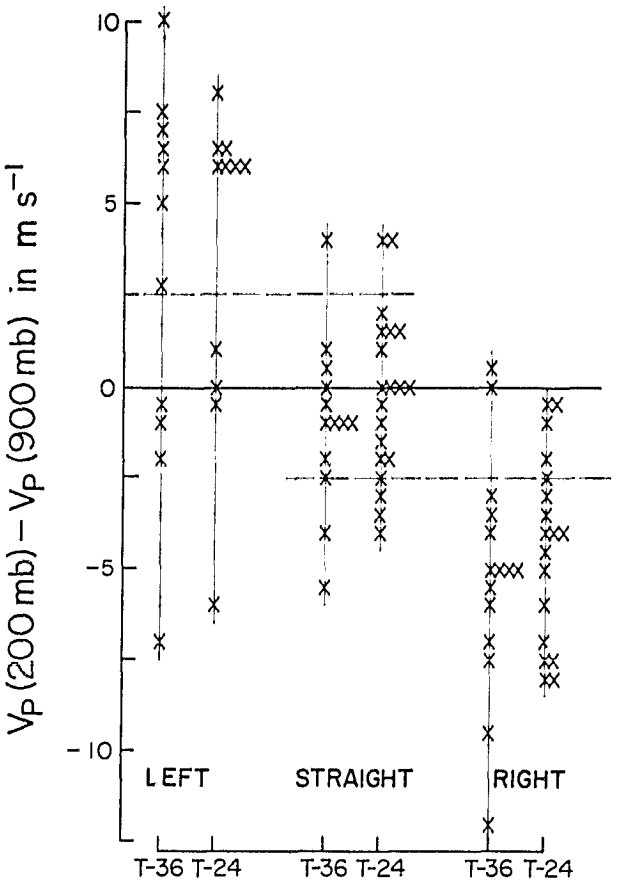

FIG. 16. Vertical wind shear between 200 and 900 mb at T − 24 and T − 36 time periods for individual storms. The ordinate is the same as in Fig. 15. Each cross represents the wind shear value from one individual storm. Equal values of the wind shear are plotted next to each other. The dashed lines indicate the threshold values described in the text.

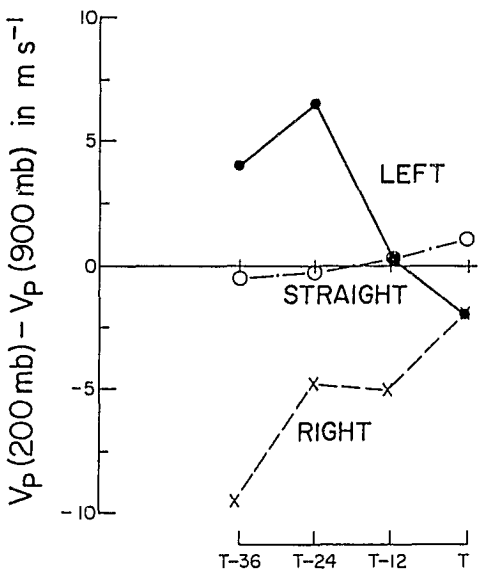

FIG. 15. Vertical wind shear for different time periods. The ordinate is the value of the average vertical wind shear (m s^{-1}) within 7–11° radii from the storm center in octants 1 and 5.

To make sure that the results for these individual cases are not due to random chance, a t test was performed on the three samples of individual storms. The results for both T − 24 and T − 36 are shown in Table 3. The symbols are defined as follows:

N	number of cases in which the vertical wind shear parameter can be estimated
$\bar{x}$	sample mean vertical wind shear
μ	average vertical wind shear of all three categories of storms from composite data (assumed to be the population mean)
s	standard deviation of the sample
t(95%)	value of t at 95% significance level given in Panofsky and Brier (1958).

It is seen that the mean vertical wind shears for both the left- and right-turning cases are significant at the 95% level. This lends confidence to the

TABLE 3. The t test of the vertical wind shear parameter on the three samples of individual storms for both T − 24 and T − 36. Symbols are defined in the text.

Turn classification	N	$\bar{x}$	μ	s	$t = \lvert\bar{x} - \mu\rvert(N-1)^{1/2}\ s^{-1}$	$t(95\%)$
			T − 24			
Left-turning	11	7.18	0	8.67	2.62	2.23
Straight-moving	20	−0.45	0	4.54	0.43	2.09
Right-turning	18	−8.72	0	5.07	7.09	2.11
			T − 36			
Left-turning	11	6.23	−2.33	10.27	2.64	2.23
Straight-moving	14	−1.71	−2.33	4.60	0.49	2.16
Right-turning	15	−10.33	−2.33	6.39	4.68	2.15

conclusion that tropospheric vertical wind shear can be used as an indicator of turning motion 24–36 h before such motion occurs.

If we set threshold values for the 200–900 mb V_p vertical wind shear as

>5, Left turn

−5 to 5, Straight

< −5, Right turn

it is found that 64% of the left-turning storms have vertical wind shears > 5 for both T − 24 and T − 36 time periods. For the straight-moving storms, 77% occurred within the range at T − 36 and 75% at T − 24. For the right-turning storms 87% have vertical wind shears < −5 at T − 36 and 72% at T − 24. The present level of success in forecasting turning motion is considered to be significantly less than this, as evident from the scatter of forecast points shown in Fig. 4.

Since the techniques in deriving lower and upper tropospheric winds from (geostationary) satellite observations are improving, the information on such vertical wind shear should become more available as time goes on and there may be hope for an improvement in future turning motion forecasts.

6. Study of satellite temperature sounding data

The vertical wind shear structure described in Section 5 should be related through the thermal wind relationship to the mean tropospheric temperature differences across these storms. An estimate of the magnitude of the temperature gradient can be obtained from the thermal wind equation

$$\frac{\Delta T}{\Delta n} \approx \frac{f}{R}\left[\ln\left(\frac{p_1}{p_2}\right)\right]^{-1} V_T, \qquad (1)$$

where Δn is the horizontal distance across which a temperature difference ΔT is measured, V_T is the thermal wind, or in this case, V_p(200 mb) − V_p(900 mb), p_1 = 900 mb, p_2 = 200 mb, f is the Coriolis parameter and R the gas constant. If we assume f to be $5 \times 10^{-5}\ s^{-1}$ (corresponding to 20°N) and Δn = 18° latitude, then for a vertical wind shear of 10 m s^{-1}, $\Delta T \approx 2.2$ K.

To investigate the existence of such a horizontal temperature gradient, temperature sounding data from the Nimbus 6 Scanning Microwave Spectrometer (SCAMS) of 1975 were examined. Since this sounder can resolve tropospheric temperature gradients of the above magnitude, we should expect the sounder data to be able to help specify turning motion.

a. The Scanning Microwave Spectrometer

The SCAMS on board the Nimbus 6 polar-orbiting satellite is a five-channel instrument sensing radiation nominally at 22.235, 31.65, 52.85, 53.85 and 55.45 GHz (Staelin *et al.*, 1975a). The latter three frequencies are used for sounding the atmosphere, while the first two are used to infer vertically integrated atmospheric water vapor and liquid water content. The Nimbus 6 spacecraft is in a sunsynchronous (1130 and 2230 Local Time) near-polar orbit at an altitude of approximately 1100 km. The SCAMS instrument scans across the spacecraft track in 13 steps at increments of 7.2° in the scan angle each 16 s which results in a spatial resolution of 145 km near nadir, degrading to 200 km downtrack by 360 km crosstrack at the maximum scan angle (Staelin *et al.*, 1975a). Approximately 400 individual soundings can be obtained within 15° of the center of a tropical cyclone for each 12 h period.

b. Tropical cyclones analyzed

A total of 13 cases[4] (11 individual storms) in both the Pacific (northeast and northwest) and Atlantic Oceans during 1975 were examined. As explained in Section 2a, only cyclones with maximum sustained wind ≥ 18.0 m s^{-1} were included. The tracks for these storms are shown in Fig. 17. The distribution of storms in each turn class is given in Table 4. Satellite data were categorized by time (T, T − 12,

[4] This is all the SCAMS information available to the authors at this time.

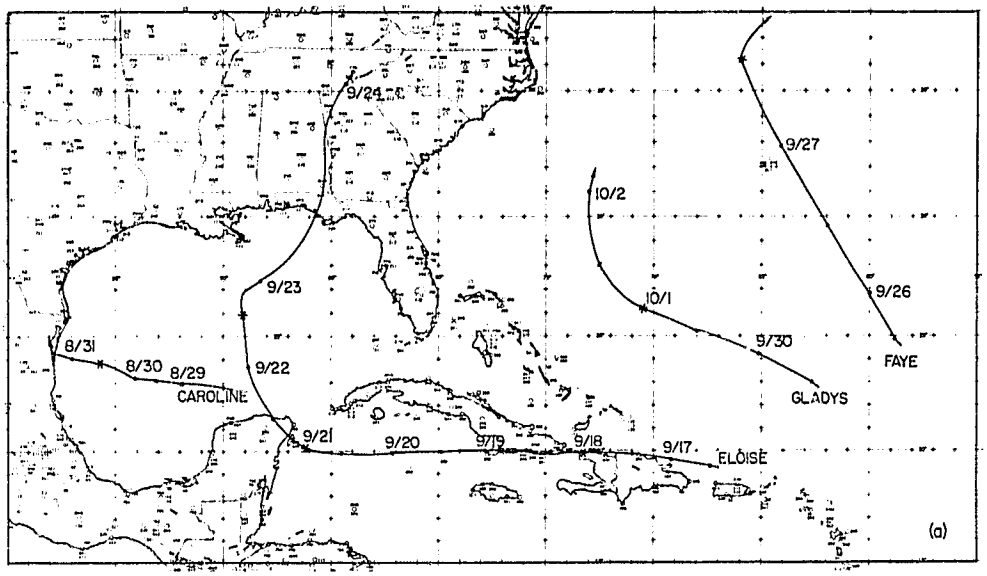

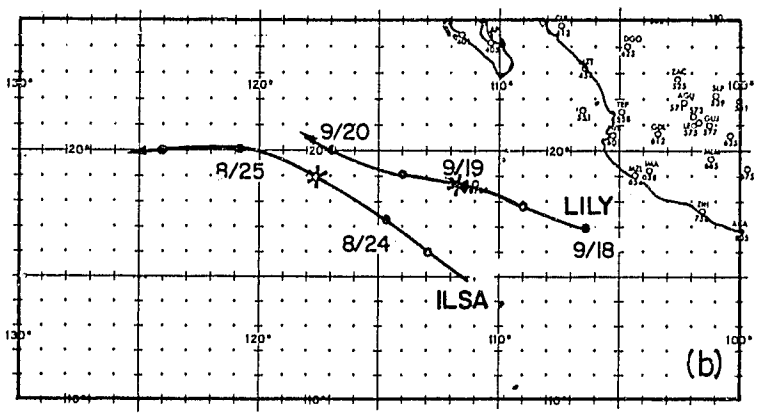

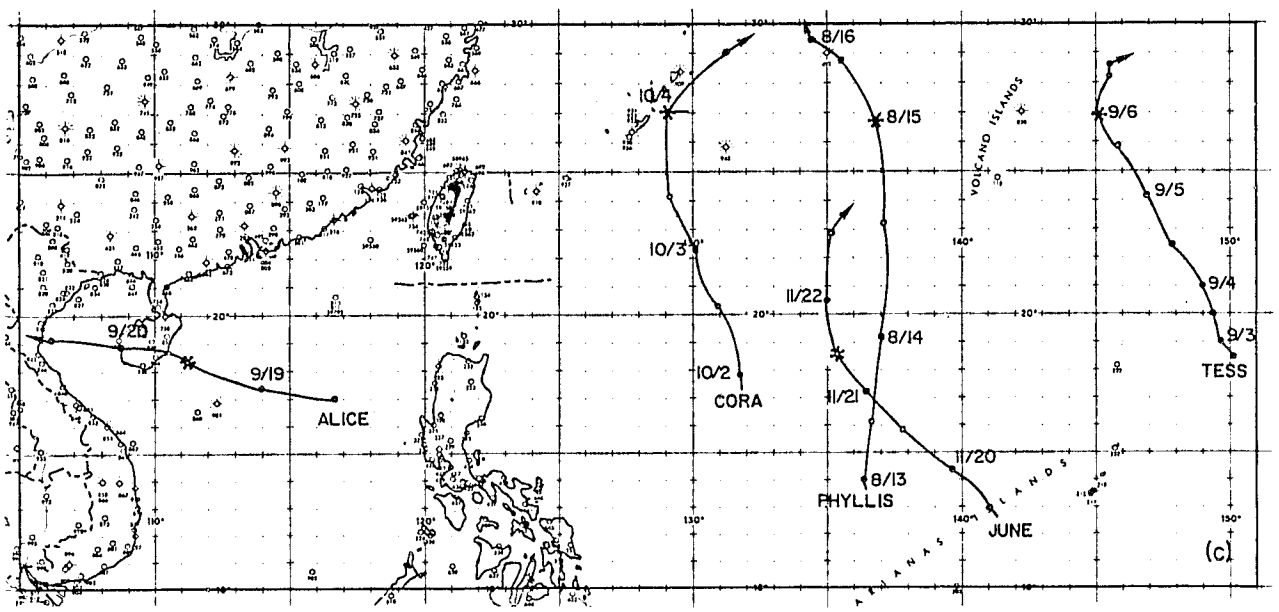

FIG. 17. Tracks of 1975 tropical cyclones in various oceans used in the Nimbus 6 SCAMS temperature sounding study. (a) Northwest Atlantic Ocean (West Indies), (b) northeast Pacific Ocean, (c) northwest Pacific Ocean. Track symbols are the same as in Fig. 2.

TABLE 4. Distribution of turn cases in the Atlantic and Pacific Oceans used in studying satellite temperature sounding data around tropical cyclones.

Ocean	Left	Straight	Right
Atlantic (West Indies)	0	2	4
Northwest Pacific	1	1	3
Northeast Pacific	1	1	0
Total	2	4	7

T − 24 and T − 36) as described in Section 3. The mean 1000–250 mb temperatures around each storm for each time period were derived from the brightness temperatures (the raw data obtained from the sounder) as described in Waters *et al.* (1975). The same method used in the rawinsonde composite was employed (see Section 3) to obtain average layer mean temperature at each of the grid points in Fig. 7 for each storm. To minimize contamination by precipitation, data points with integrated liquid water contents ≥ 0.5 kg m^{-2} were not used in the averaging process. According to Staelin *et al.* (1975b) this should eliminate most of the contaminated data.

The accuracy of atmospheric temperatures derived from satellite sounders is a pertinent point. Data from a microwave sounder were used because microwave soundings are unaffected by non-raining clouds (Staelin *et al.*, 1975b). The extensive cloudiness near tropical cyclones precludes the exclusive use of infrared sounding data. When the 1000–250 mb layer mean temperature at a single spot is compared with the nearest grid point data analyzed by the National Meteorological Center (NMC) the root-mean-square difference is ~2 K (Landsat/Nimbus Project, 1976). *It must be remembered, however, that only temperature difference and not absolute temperature is a requirement for the wind shear determination.* In addition, each grid point value is an average of a considerable number of observation points, and precipitation-contaminated data points have been eliminated. The satellite-derived temperature differences obtained in the way described above should therefore be accurate to within a few tenths kelvin (Staelin *et al.*, 1975b).

c. 1000–250 mb mean temperature fields

For convenience, the 1000–250 mb layer mean temperatures were analyzed in the following way. All layer-mean temperatures at grid points within 5–15° radius[5] from the storm center were averaged to obtain an average layer-mean temperature $\bar{T}$. The deviation of each grid point temperature from $\bar{T}$ was calculated (for all points in the grid). These deviations were used for the analysis instead of the absolute values. An example of the temperature deviation field for three individual cases 24 h before turn time (one in each turn class) is shown in Fig. 18. This figure shows the typical expected difference in temperature structure existing between a left-turning, straight-moving and right-turning storm as implied by the difference in vertical wind shear structure discussed in Section 5. The left-turning storm shows a temperature gradient across the storm corresponding to a thermal wind, or vertical wind shear, in the direction of storm motion while the opposite occurs for the right-turning storm. There is very little temperature gradient for the straight-moving case. An examination of the other cases indicates that the temperature gradients of most significance exist in front of the storm. In addition, for most of the left- and right-turn cases studied, there exists a region where the troposphere

[5] The reasons for using 5–15° are 1) more data are available outside 5° (a lot of data were eliminated within 5° because of high liquid water content), and 2) 15° is the outermost radius used in the rawinsonde composite study.

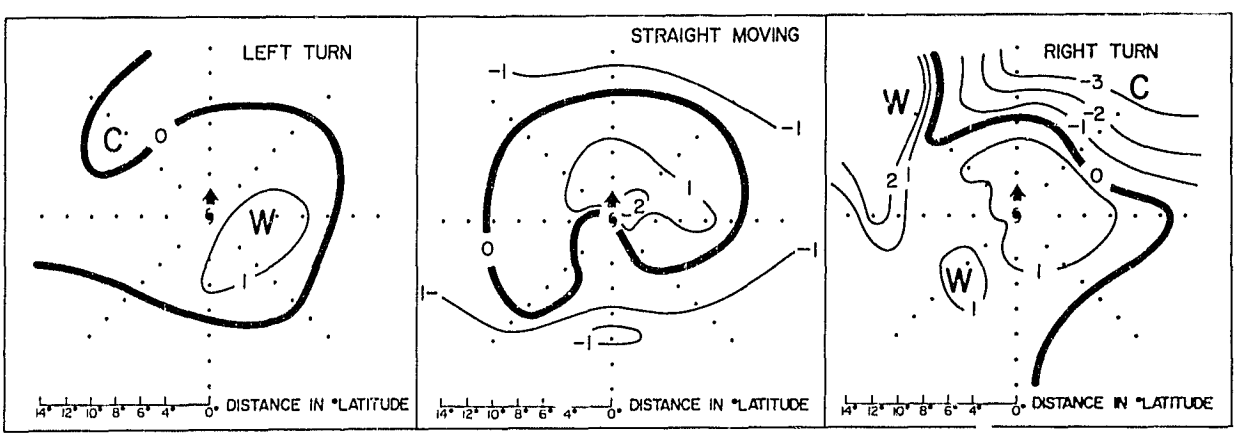

FIG. 18. 1000 to 250 mb layer mean temperature deviation from 5 to 15° radii average mean temperature derived from the Nimbus 6 SCAMS temperature sounding data 24 h before turn time. The arrow from the storm center indicates the direction of storm motion.

TABLE 5. The 1000–250 mb layer mean temperature deviations from 5–15° radii average in octants 2 (left front) and 8 (right front) within 9–13° radius from the storm center for various storms in the North Pacific and Atlantic Oceans 24 h before turn time. Vertical wind shear in the direction in which the storm is going is calculated from the thermal wind relationship using a horizontal distance of 18°. The Coriolis force f is taken to be 5×10^{-5} s^{-1}.

Storm	Region	Octant 2	Octant 8	Octant 2 minus Octant 8	Corresponding vertical wind shear (m s^{-1})	Turn
Phyllis	west Pacific	−0.8	0.2	−1.0	4.5	left
Ilsa	east Pacific	−0.9	1.5	−2.4	10.9	left
Alice	west Pacific	−0.7	0.0	−0.7	3.2	straight
Lily	east Pacific	−0.6	−0.1	−0.5	2.3	straight
Eloise	west Atlantic	0.2	0.2	0.0	0.0	straight
Caroline	west Atlantic	−1.1	2.9	−4.0	18.2	straight
Eloise	west Atlantic	1.5	−0.2	1.7	−7.7	right
Eloise	west Atlantic	1.6	−2.0	3.6	−16.4	right
Gladys	west Atlantic	0.1	−1.4	1.5	−6.8	right
Faye	west Atlantic	0.3	−0.4	0.7	−3.2	right
June	west Pacific	0.7	−1.6	2.3	−10.5	right
Tess	west Pacific	−0.7	−1.9	1.2	−5.5	right
Cora	west Pacific	1.0	1.0	0.0	0.0	right

is relatively cold in the direction toward which the storm is moving, as indicated in the examples given in Fig. 18.

To describe these temperature gradients in more quantitative terms, temperature deviations at 9–13° radius[6] in octants 2 (left front) and 8 (right front) for all cases were studied. Results are shown in Table 5. Both left-turning cases show that the mean tropospheric temperature is lower to the left front of the storm. For the straight-moving storms, only Caroline shows a large negative tropospheric shear. The reason for this is unknown. However, all other straight-moving cases show only a very weak temperature gradient across the front of the storm. In addition, all three cases show a region of cold air in octant 1 (not shown). Of the seven right-turning storms, only Cora shows no temperature gradient. The others indicate a relatively cold troposphere to the right front of the storm.

These results were obtained, as described earlier, after elimination of data points with integrated liquid water content ≥ 0.5 kg m^{-2}. To see if this process is of any great significance, temperature deviation fields without eliminating any data were also analyzed. A comparison between the two sets of results shows very little difference in the temperature structure and temperature gradients at large radii from the storm center. It would appear that it is not necessary to eliminate those data points with appreciable liquid water content provided temperatures at large distances from the storm center are used.

[6] In order to obtain the horizontal temperature gradient normal to V_p in octant 1, at radii 7–11° (the area where the vertical wind shear parameter is of significance), one has to consider temperatures in octants 2 and 8 at radii 9–13° (see Fig. 7).

These results suggest that very pertinent information on forecasting tropical cyclone turning motion 24 h in advance may be obtained from satellite sounder information in regions devoid of rawinsonde, aircraft and clouds for satellite wind vector determination. Newer and better satellite sounders are likely to be available in the future for even better determinations.

6. Summary and recommendations

The results of this study indicate that there are parameters in the large-scale environment around tropical cyclones at upper and lower tropospheric levels (in addition to the previously considered crucial middle level) which can provide information about their turning motion 24–36 h before it occurs. An estimate of the V_N component of the winds at 200 and 900 mb at 5–11° radius around the storm from satellite observations may also be useful for making short-range (0–12 h) forecasts of turning motion. Of greater significance is the possibility of using the V_p vertical wind shear to specify turning motion 24–36 h in advance. The fact that favorable environmental conditions are evident 24–36 h prior to turn time indicates that there is likely a time lag between changes in the environmental flow parameters surrounding a storm and the response of the storm to such changes.

At certain times it may not be possible to derive satellite winds at 900 and 200 mb because of an extensive cirrus canopy or because upper-level cloud motions are lacking. In these cases the satellite sounder, with its tropospheric temperature difference measurement capability, may be useful in augmenting missing wind data. Since contamination

of the sounding data by precipitation is negligible at large radii, the Microwave Sounding Unit (which does not have any water vapor channel) on board the TIROS-N satellite now in orbit might be used to monitor tropospheric temperature gradients across a storm to determine the upper and lower tropospheric vertical wind shear. It is suggested that temperature data obtained from such a sounder be used on an operational basis to test the applicability of these results.

With the large increase in computer technology and the development of more sophisticated cyclone forecast schemes, one would expect a continuous increase in tropical cyclone forecast skill. While this has been true on the average in the 1960's and early 1970's, tropical cyclone track 24 h forecast errors have been showing a slight increase in the last three to four years (see, e.g., Joint Typhoon Warning Center, 1977). These forecast error increases are likely a result of an over-reliance by the various forecast techniques on middle-level flow patterns, and a subsequent gradual reduction of oceanic rawinsonde and aircraft data to measure such flow patterns. Atlantic weather ships *Echo* and *Delta* were decommissioned in 1973. Very few oceanic propeller aircraft flights are now made. These changes have significantly reduced the already scanty mid-tropospheric Atlantic wind-height data. Accurate analysis of middle-level flow fields has always been difficult. At some locations and time periods it is now nearly impossible to obtain a meaningful analysis. Neumann (private communication) has discussed how NMC tropical analysis schemes can produce a quite unrepresentative middle-level steering current determination. He has documented cases in which an erroneous wind observation drastically changes middle-level computer-analyzed flow fields. This seriously affects the performance of tropical cyclone forecast models based on middle-level steering flow concepts (e.g., see Lawrence, 1979). New forecasting schemes (regardless of how sophisticated) which utilize middle-level flow patterns should encounter similar observational problems.

Because of the increasing availability of satellite-derived information at upper and lower tropospheric levels, it is suggested that research on storm motion be concentrated on studying the relationships between upper and lower tropospheric parameters and storm movement. The next steps in this research will be to try to relate upper and lower level parameters with cyclone speed changes, stalling and looping motions, and other special cyclone motion characteristics.

Acknowledgments. The authors would like to thank Mr. Edwin Buzzell for his programming assistance and Mrs. Bonnie Weber and Mrs. Barbara Brumit for their help in manuscript preparation and part of data reduction.

This research was supported by a NHEML NOAA Research Grant NA 79 RAD 00002 with supplementary support from NASA Grant NSG-5258.

REFERENCES

Frank, W. M., 1977: The structure and energetics of the tropical cyclone. I: Storm structure. *Mon. Wea. Rev.*, **105**, 1119–1135.

George, J. E., and W. M. Gray, 1976: Tropical cyclone motion and surrounding parameter relationships. *J. Appl. Meteor.*, **15**, 1252–1264.

Hope, J. R., and C. J. Neumann, 1970: An operational technique for relating the movement of existing tropical cyclones to past tracks. *Mon. Wea. Rev.*, **98**, 925–933.

Joint Typhoon Warning Center, 1977: Annual typhoon report. U.S. Fleet Weather Central, Joint Typhoon Warning Center, Guam, COMNAVMARINAS, Box 17, FPO San Francisco 96630, 125 pp. [NTIS AD-A055].

Landsat/Nimbus Project, 1976: *The Nimbus 6 Data Catalog*, Vol. 2. NASA/Goddard Space Flight Center, Greenbelt, MD, pp. 1–2 through 1–4 [NTIS N77-29688].

Lawrence, M. B., 1979: Atlantic hurricane season for 1978. *Mon. Wea. Rev.*, **107**, 477–491.

Neumann, C. J., and M. B. Lawrence, 1975: An operational experiment in the statistical-dynamical prediction of tropical cyclone motion. *Mon. Wea. Rev.*, **103**, 665–673.

Panofsky, H. A., and G. W. Brier, 1958: *Some Applications of Statistics to Meteorology*. The Pennsylvania State University Press, 224 pp.

Staelin, D. H., A. H. Barrett, P. W. Rosenkranz, F. T. Barath, E. J. Johnson, J. W. Waters, A. Wouters and W. B. Lenoir, 1975a: The scanning microwave spectrometer (SCAMS) experiment. *The Nimbus-6 User's Guide*, J. E. Sissala, Ed., LANDSAT/Nimbus Project, NASA/Goddard Space Flight Center, Greenbelt, MD, 59–86 [NTIS N76-31256].

——, A. L. Cassel, K. R. Kunzi, R. L. Pettyjohn, R. K. L. Poon and P. W. Rosenkranz, 1975b: Microwave atmospheric temperature sounding: Effects of clouds on the Nimbus 5 satellite data. *J. Atmos. Sci.*, **32**, 1970–1976.

Waters, J. W., K. F. Kunzi, R. L. Pettyjohn, R. K. L. Poon and D. H. Staelin, 1975: Remote sensing of atmospheric temperature profiles with the Nimbus 5 microwave spectrometer. *J. Atmos. Sci.*, **32**, 1953–1969.

Williams, K. T., and W. M. Gray, 1973: Statistical analysis of satellite-observed trade wind cloud clusters in the western North Pacific. *Tellus*, **25**, 313–336.

THESIS

SUMMER PRECIPITATION FREQUENCY OF THE NORTH CENTRAL U.S. FROM SATELLITE MICROWAVE OBSERVATIONS

Submitted by

Philip A. Durkee

Department of Atmospheric Science

In partial fulfillment of the requirements
for the degree of Master of Science
Colorado State University
Fort Collins, Colorado
Spring, 1980

COLORADO STATE UNIVERSITY

April 7 1980

WE HEREBY RECOMMEND THAT THE THESIS PREPARED UNDER OUR SUPERVISION

BY Philip A. Durkee

ENTITLED Summer Precipitation Frequency of the North Central U.S. from Satellite Microwave Observations

BE ACCEPTED AS FULFILLING IN PART REQUIREMENTS FOR THE DEGREE OF

Master of Science

Committee on Graduate Work

David A. Krueger

Stephen K. Cox

T. Vonder Haar

Advisor

COLORADO STATE UNIVERSITY

April 7 1980

WE HEREBY RECOMMEND THAT THE THESIS PREPARED UNDER OUR SUPERVISION

BY Philip A. Durkee

ENTITLED Summer Precipitation Frequency of the North Central U.S. from Satellite Microwave Observations

BE ACCEPTED AS FULFILLING IN PART REQUIREMENTS FOR THE DEGREE OF

Master of Science

Committee on Graduate Work

David A. Krueger

Stephen K. Cox

Advisor

ABSTRACT OF THESIS

SUMMER PRECIPITATION FREQUENCY OF THE NORTH CENTRAL U.S. FROM SATELLITE MICROWAVE OBSERVATIONS

The Nimbus-6 Electrically Scanning Microwave Radiometer (ESMR-6) is used to observe raining areas over the north central U.S. from 11 June through 31 August 1976. A technique is developed whereby the frequency distribution of microwave brightness temperatures over the area is analyzed to determine a threshold temperature below which the possibility of precipitation is assumed. Raining areas are classified by considering spatial distribution of possible raining areas, simultaneous infrared images, surface temperatures, surface relative humidities as well as microwave brightness temperatures. Precipitation frequency of the area derived by the satellite technique is compared to surface raingage hourly observations. The relationship between the two systems of measurement is seen to be quite high in the southern and northwestern quadrants of the area however the northeastern quadrant exhibits poor relationship due to the existence of many small lakes in Minnesota and Wisconsin. Precipitation frequency determination from satellite microwave observations is feasible for land areas warm enough to be distinguishable from raining areas. Thus, determinations over primary mid latitude crop growing seasons are possible.

Philip A. Durkee
Atmospheric Science Department
Colorado State University
Fort Collins, Colorado 80523
Spring, 1980

ACKNOWLEDGEMENTS

The author wishes to thank his advisor, Dr. Thomas H. Vonder Haar for his encouragement and direction of this study. Also, Dr. Stephen K. Cox and Dr. David A. Krueger, members of the author's committee, for their valuable advise. Much thanks goes to Dr. Stanley Q. Kidder for his helpful discussions, Ms. Laurie Parkinson for her careful typing of the manuscript, Mr. Mark Howes for his drafting of the figures, and Ms. Karen Koslow for plotting and analysis of the raingage data.

The microwave brightness temperature data was provided by the National Space Science Data Center/Goddard Space Flight Center. This research was sponsored by the National Aeronautics and Space Administration under grant NSG-5258 and the Office of Naval Research under grant N00014-79-C-0793.

TABLE OF CONTENTS

LIST OF FIGURES

1.0 INTRODUCTION

Rainfall measurement is important to many disciplines. Agriculture needs to know precipitation patterns and amounts to determine irrigation needs and flooding potential. Hydrology and Water Resource Management needs rainfall measurements to determine soil moisture, runoff potential and reservoir allotment. Knowledge of rainfall is important to the atmospheric sciences in understanding latent heat release in the atmosphere as well as determining climate tendencies.

The measurement of rainfall over land areas has primarily been done by raingages although radar observation of precipitation has been an important technique. Spatial coverage by these measurement techniques is limited, however. A network of raingages observes single point values of the precipitation over an area and interpolation between gages is highly approximate. Radar observations, though over a continuous area, have only a finite range to which the instrument can reach. Also, both observing systems have inherent errors since arrays of different instruments each with different operators are assumed the same in analyses.

The development of satellite techniques has aided greatly in eliminating some of the problems inherent in surface observation of precipitation. Griffith, et al. (1978) observed the growth of convective clouds using geosynchronous infrared and visible imagery to estimate rainfall. The use of microwave frequencies allows direct observation of precipitation due to the large interaction of microwaves with hydrometers (falling raindrops) and small interaction with clouds and gaseous constituents (away from $\sim$60 GHz). The Nimbus 5 Electrically Scanning Microwave Radiometer (ESMR-5), operating at 19.35 GHz, has

been used to observe oceanic precipitation (Kidder, 1976; Adler and Rodgers, 1977; and Wilheit, et al., 1977), an area with little or no surface observations. Rainfall observation over land areas was shown feasible by Savage and Weinman (1975) using the Nimbus 6 ESMR operating at 37 GHz. Investigation of ESMR-6 rainfall estimation was continued by Savage (1976), Weinman and Guetter (1977), Weinman and Davies (1978), and Rodgers, et al. (1978). Precipitation frequency of the north central U.S. in summer using ESMR-6 observations is the subject of this paper.

The theory of microwave radiative transfer is presented in Chapter 2 including a solution of the radiative transfer equation, absorption by water vapor, liquid water and oxygen, and a consideration of scattering by hydrometers. Chapter 3 describes the ESMR-6 instrument and the data sets used in this study. Also included in Chapter 3 is a description of the thresholding technique used to classify raining areas within the area of interest. Surface emission and the relationship between the satellite observed brightness temperature and surface temperature are also examined. Chapter 4 presents the results of the precipitation analysis as well as a comparison with hourly raingage observations.

2.0 MICROWAVE RADIATIVE TRANSFER

2.1 The Radiative Transfer Equation

For a plane-parallel atmosphere the equation of radiative transfer may be written (Chandrasekhar, 1960)

$$\mu \frac{dI\nu}{dz} = -\rho K_\nu (I_\nu - S_\nu) \tag{1}$$

where μ = cosine of the zenith angle

$I_\nu = I_\nu(x,t)$ = radiance at frequency ν at position x at time t

z = vertical coordinate

ρ = mass density of the atmosphere at x

K_ν = volume absorption coefficient per unit mass

$S_\nu = S(x,t)$ = source function of a unit mass at position x at time t

If $\tau_\nu = \int_z^\infty \rho K\nu dz'$ is the normal optical depth then (1) can be written

$$\frac{dI_\nu}{d\tau_\nu} - \frac{I_\nu}{\mu} = -\frac{S_\nu}{\mu} \tag{2}$$

Multiplying (2) by $\exp(-\frac{\tau_\nu}{\mu})$ gives

$$e^{-\frac{\tau_\nu}{\mu}} \frac{dI_\nu}{d\tau_\nu} - \frac{I_\nu}{\mu} e^{-\frac{\tau_\nu}{\mu}} = -\frac{S_\nu}{\mu} e^{-\frac{\tau_\nu}{\mu}} \tag{3}$$

The left hand side of (3) is just

$$\frac{d}{d\tau_\nu} (I_\nu e^{-\frac{\tau_\nu}{\mu}}) \tag{4}$$

so integrating (3) with respect to optical depth from the surface to τ_ν we get

$$I_\nu = I_{\nu o}\, e^{-\frac{\tau_\nu}{\mu}} + \int_o^{\tau_\nu} S_\nu\, e^{-\frac{(\tau_\nu - t)}{\mu}}\, \frac{dt}{\mu} \tag{5}$$

I_ν is the radiance at frequency ν out the top of the atmosphere which may be viewed by a satellite.

The source function, S_ν, is a function of the radiative properties of the atmosphere. For a scattering, non-absorbing atmosphere

$$S_\nu = \frac{1}{4\pi}\int_o^{\pi}\int_o^{2\pi} p(\theta,\theta,\phi')\; I_\nu\; \sin\theta' d\theta' d\phi' \tag{6}$$

where θ and ϕ are the zenith and azimuth angles respectively. $p(\theta,\theta',\phi')$ is known as the phase function and represents the angular distribution of scattered energy. For a non-scattering atmosphere satisfying local thermodynamic equilibrium

$$S_\nu = B_\nu = \frac{2h\nu^3}{c^2}\; \frac{1}{e^{h\nu/kT} - 1} \tag{7}$$

where h = Planck's constant

k = Boltzman's constant

c = velocity of light

T = local thermodynamic temperature

and is just Planck's black-body relation. If $\frac{h\nu}{dT} << 1$ then $e^{h\nu/kT}$ may be expanded and B_ν may be approximated as

$$B_\nu \simeq \frac{2\nu^2 kT}{c^2} \tag{8}$$

which is the Rayleigh-Jeans approximation. At 37 GHz (which is the frequency of interest for this study) for example $h\nu/kT = 0.006$ if $T = 300$ K which introduces an error of less than 0.3% (Kreiss, 1968). Defining T_b, the brightness temperature, such that

$$I_\nu = \frac{2\nu^2 k}{c^2} T_b \tag{9}$$

the solution of the radiative transfer equation becomes

$$T_b = T_{bo}\, e^{-\frac{\tau_\nu}{\mu}} + \int_o^{\tau_\nu} T\, e^{-\frac{(\tau_\nu - t)}{\mu}} \frac{dt}{\mu} \tag{10}$$

The contribution to the total brightness temperature by the surface, T_{bo}, is made up of two parts; the emitted radiation and reflected radiation incident downward on the surface. The satellite observed brightness temperature from equation (10) is then just the portion of the effective surface brightness temperature which is transmitted through the atmosphere, plus the contribution from atmospheric emission which is transmitted.

2.2 Transfer of Microwaves Through the Cloudy Atmosphere

The three major atmospheric constituents which absorb and hence emit thermal microwaves are molecular oxygen, water vapor, and liquid water. Figure 1 shows the absorption coefficient near the surface of the earth of oxygen and water vapor as a function of frequency. Water vapor absorption in this region is due to a rotational transition at about 22.2 GHz. Oxygen absorption results from a series of magnetic dipole moment vs. rotational angular moment reconfigurations from 53 GHz to 66 GHz (Meeks and Lilley, 1963). Figure 2 shows the absorption coefficient of

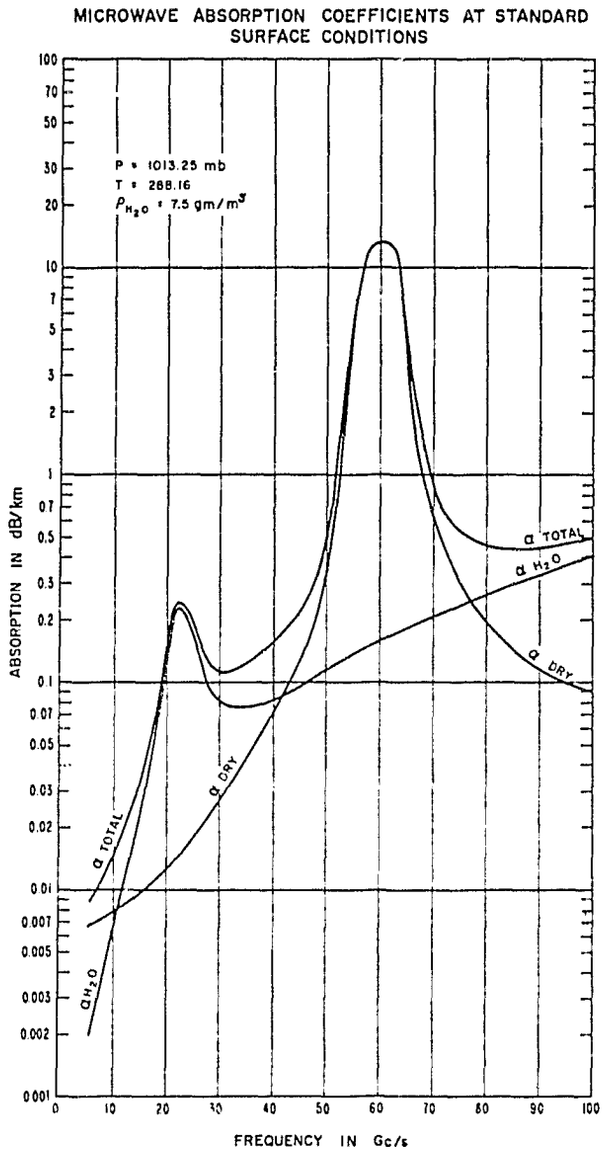

Figure 1. Absorbtion coefficient for atmospheric water vapor and oxygen. (After Westwater, 1965)

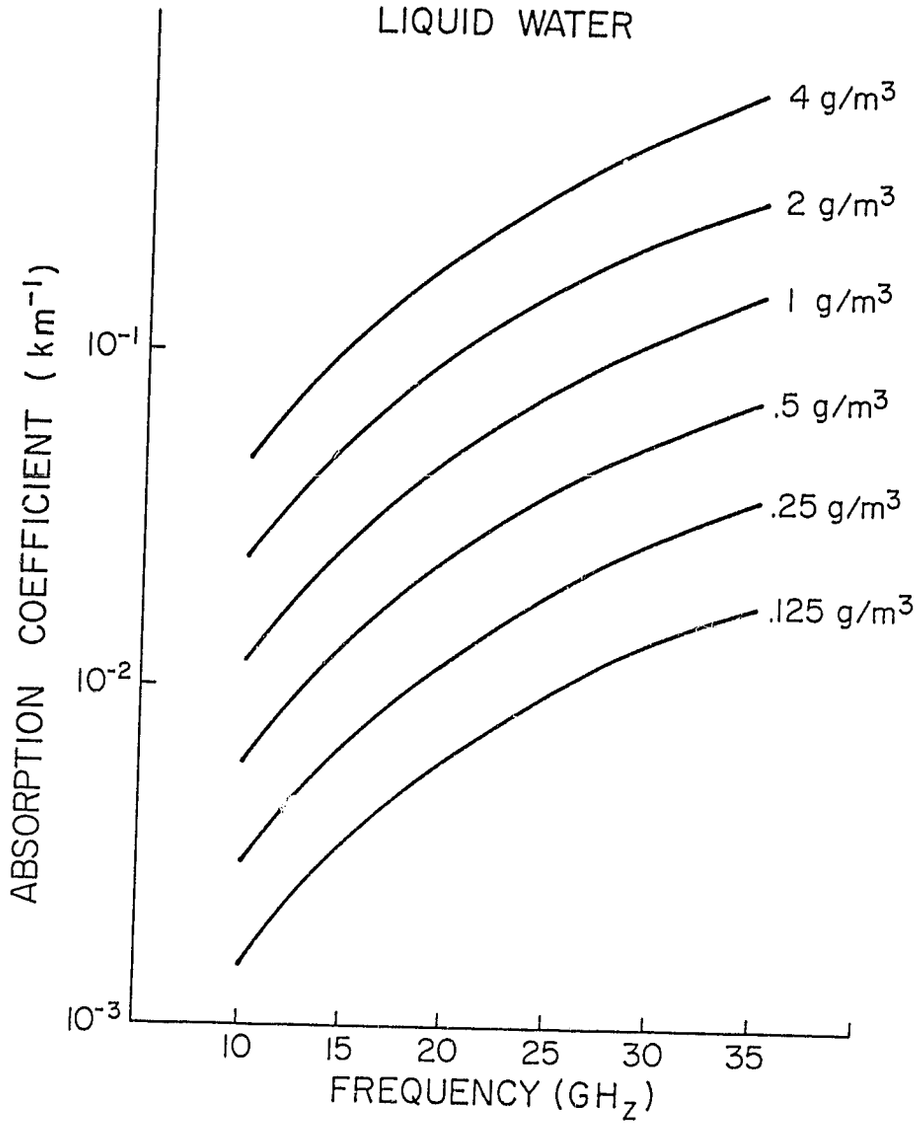

Figure 2. Absorbtion coefficient for various densities of atmospheric liquid water.

various liquid water contents of the atmosphere as a function of frequency from Staelin (1966). The relationship is valid from 10 to 35 GHz and is a good approximation for small droplets compared to $\lambda/2\pi$, where λ is the wavelength. As droplets increase in size their scattering effects become more important. These effects will be discussed in section 2.4.

Of the microwave absorbing constituents of the atmosphere, water vapor and liquid water are the most variable. These also have a significant, though small, temperature dependence on absorption. Figure 3 illustrates this temperature dependence for various mass densities of water vapor and liquid water. These curves are calculated by expressions from Van Vleck (1947) and Staelin (1966) for water vapor and liquid water respectively. Both show a decreasing absorption coefficient with increasing temperature.

The temperature dependence of water vapor absorption is due to the temperature dependence of the Boltzman distribution. Simply it is a result of the fact that with higher temperature fewer molecules will have an energy corresponding to the lower energy state of the transition resulting in less interaction with the radiation and less absorption. As apparent from Figure 3 the temperature dependence is small for water vapor absorption. For a decrease of 40 K in temperature, the absorption coefficient increases by 30%. Temperature dependence on liquid water absorption is due to the temperature dependence on the dielectric constant of water. As temperature increases the dielectric constant of water decreases. The result from Figure 3 is that with a 40 K decrease in temperature the absorption coefficient increases by a factor of 3.

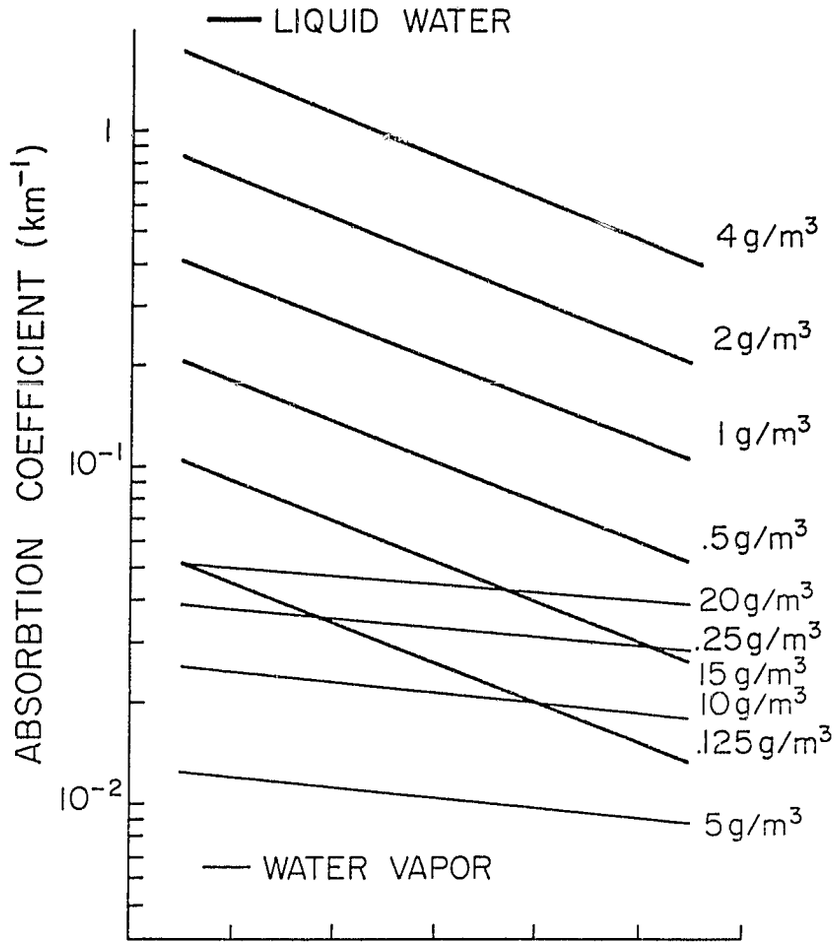

Figure 3. Absorbtion coefficient at 37 GHz as a function of temperature for various densities of water vapor (pressure = 800 mb) and liquid water.

It should be noted that ice particles are highly transparent at microwave frequencies. Water covered ice however, has been shown to have significant absorbtive properties (Westwater, 1972).

The total optical depth, τ_ν, is obtained by integrating the absorption coefficient with height. The factor $e^{-\frac{\tau_\nu}{\mu}}$ in (5) is then known as the fractional transmittance of the atmosphere. Calculations by Westwater (1972) show that at 37 GHz the clear atmosphere has a transmittance of about 93% for the U.S. Standard atmosphere and about 88% for the 15°N Tropical atmosphere. Calculations were also made using typical cloud liquid water and water vapor distributions for non-precipitating clouds. Transmittances remained greater than 70%.

2.3 Surface Emission

At microwave frequencies below 50 GHz the atmosphere is highly transparent. Therefore the effective brightness temperature of the surface, T_{bo}, is often the most prominent contribution to the brightness temperature observed at the satellite:

$$T_{bo} = \epsilon_\nu T_s + T_{br} \tag{11}$$

where ϵ_ν and T_s are the emittance and temperature of the surface and T_{br} is the contribution due to reflection of incident radiation. The surface emittance then is the important characteristic which controls a large part of the total signal.

In the microwave region surface emittances are a function of: terrain composition, electrical conductivity of the surface, roughness of the surface, and the frequency of observation. At 37 GHz the emittance of a water surface is about 0.45 while for most land surfaces the emittance is about 0.90.

Since the transmittance of the earth's surface is zero, the emittance is related to the reflective properties of a surface by

$$\epsilon_\nu = 1 - r_\nu \tag{12}$$

where ν is the frequency and r_ν is the reflectance of the surface. From (12) surfaces of high emittance have low reflectance and low emittance infers high reflectance. It is the relatively high reflectance of water surfaces which distinguishes them from raining areas over land surfaces.

Radiation incident on a reflecting surface at some angle will be partially polarized to the extent that the angle of incidence is close to Brewster's angle for the medium. For water surfaces Brewster's angle is very close to 50° which is the constant viewing angle of the ESMR-6. Therefore brightness temperatures from water surfaces will be lower than from land surfaces (due to lower emittance) and will also be relatively polarized (due to higher reflectance) with vertical polarization greater than the horizontal polarization.

2.4 Scattering of Microwaves by Hydrometers Over Land Surfaces

As cloud droplets increase in size and approach precipitation sized particles the effect of scattering of microwave radiation increases. Deirmendjian (1963) has shown that at frequencies below 60 GHz, for clouds with a modal drop size of greater than 50 μm scattering effects become important compared to absorption. In a scattering atmosphere equation (6) must be used in addition to the Planck relation as the source function in the radiative transfer equation along with the full Mie equations. Weinman and Guetter (1977) have calculated 37

GHz microwave radiances from rain clouds over land and water surfaces in both vertical and horizontal polarizations. Figure 4 is a plot of their results for various rain rates over land, rough* and calm water. Brightness temperatures of rain clouds is seen to be a decreasing function of rain rate over land surfaces while over water surfaces brightness temperatures increase with rainfall rate to about 4 mm/hr and then decrease as over land. Above 8 mm/hr the surface is no longer an important factor in determining the brightness temperature as the emission of the raining cloud is the sole contributor to the upward radiance.

---

* The distinction of a rough water surface is only in that the surface does not polarize.

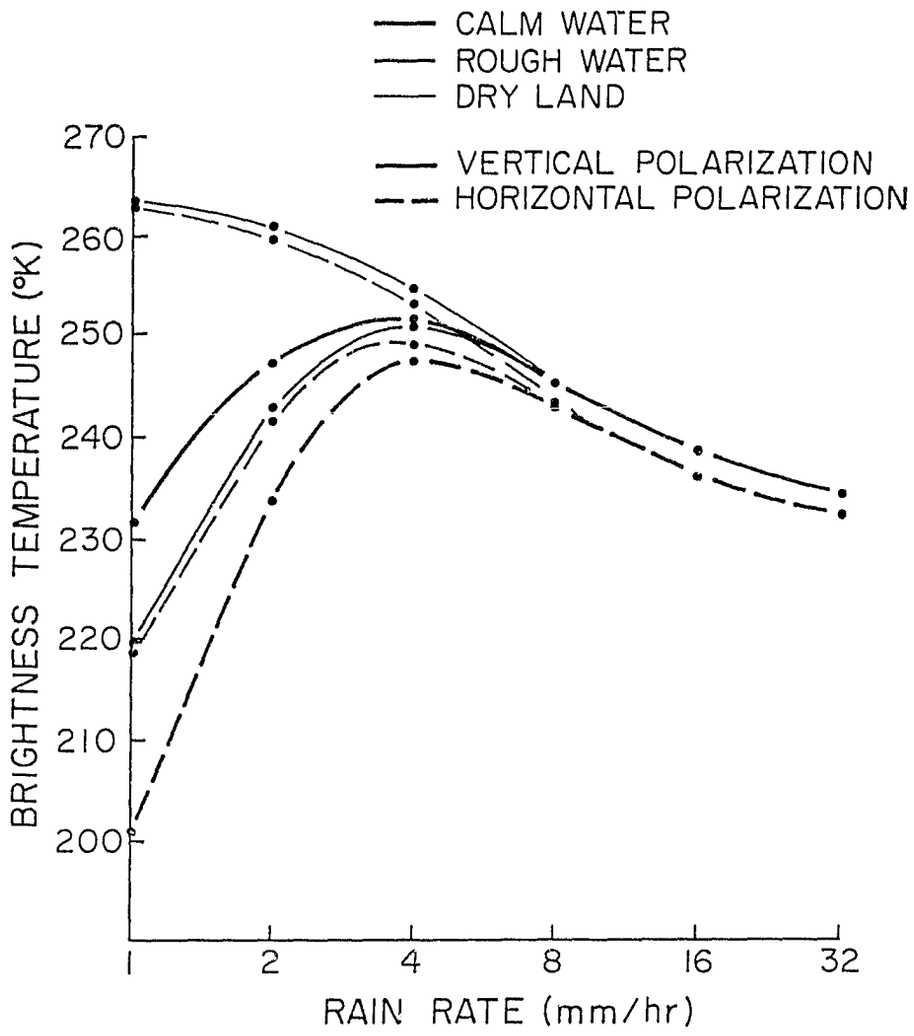

Figure 4. Brightness temperatures of 37 GHz radiances as a function of rainfall rate over land, rough and calm water. (After Weinman and Guetter, 1977)

3.0 DATA AND PROCEDURES

3.1 Description of the Instrument

The Nimbus 6 satellite was launched on 12 June 1975 into a circular sun-synchronous polar orbit at an altitude of approximately 1100 km. On board was the Electrically Scanning Microwave Radiometer (ESMR-6) which detected the vertical and horizontal polarizations of thermal microwaves in a 250 MHz band centered at 37 GHz. ESMR-6 operated satisfactorily through 15 September 1976 when the horizontal channel failed. The instrument was situated aboard the satellite as shown in Figure 5 where it electrically scans along a cone forward of the satellite such that the incidence angle at the surface remains constant at 50^{o}. The scan is done in 71 discrete steps from 35^{o} to the right to 35^{o} to the left of the forward direction. For a zero degree pitch angle the resolution of each beam position is 20 km cross-track and 42 km down-track.

The orbit of Nimbus 6 had a retrogade inclination of 81^{o} with equator crossings at local noon (northward) and midnight (southward) and a period of 107.25 minutes. Figure 6 shows a typical 24 hour coverage of the ESMR-6. The width of the 71 beam position scan is only 1272 km which results in large gaps in coverage over the equatorial regions. The gray shaded areas and areas between 60^{o} and 85^{o} latitude are covered at least twice each 24 hour period. There is no coverage poleward of 85^{o}.*

*See Wilheit (1975) for a complete description of the ESMR-6.

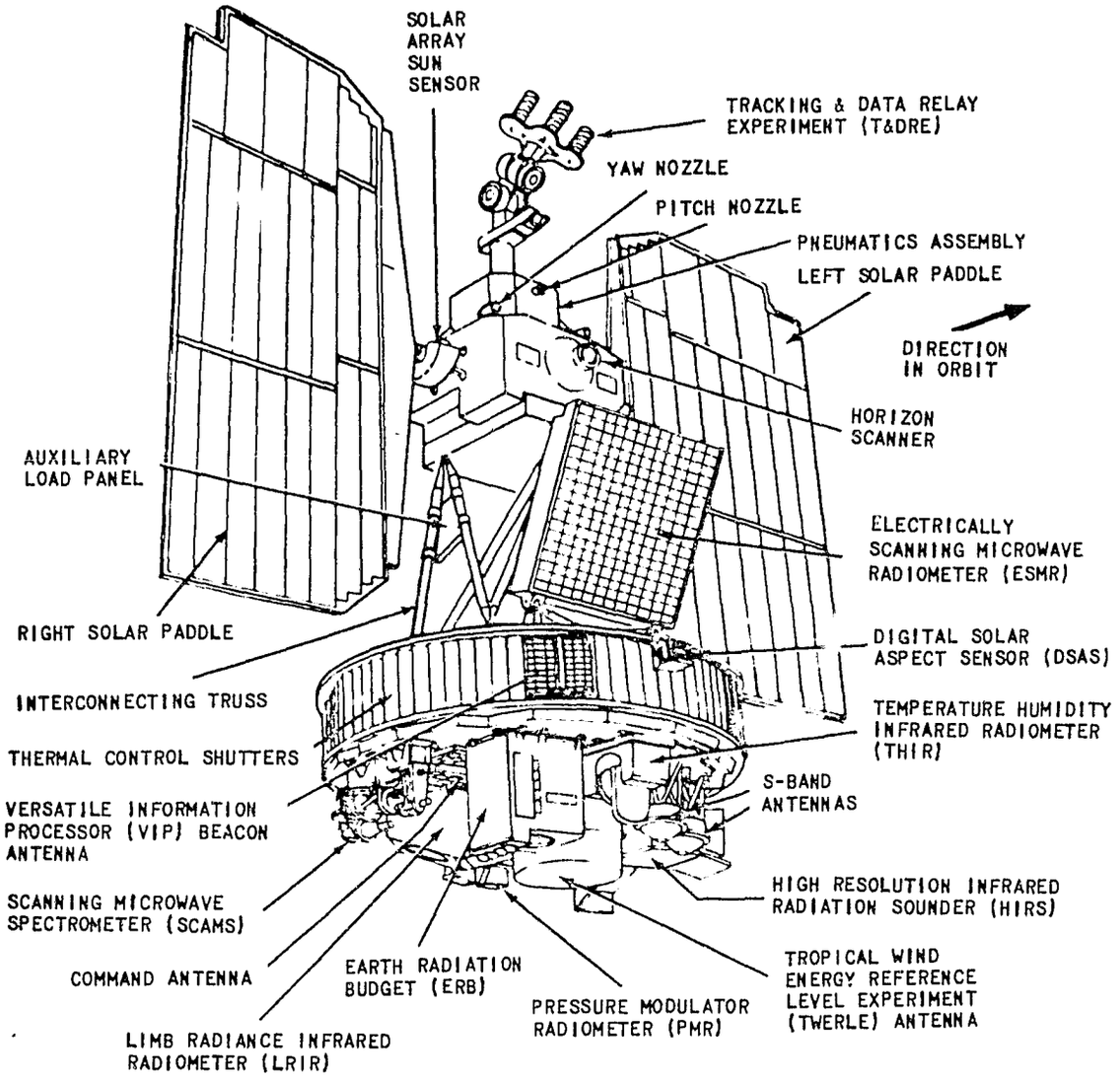

Figure 5. The Nimbus 6 satellite. (From The Nimbus 6 User's Guide)

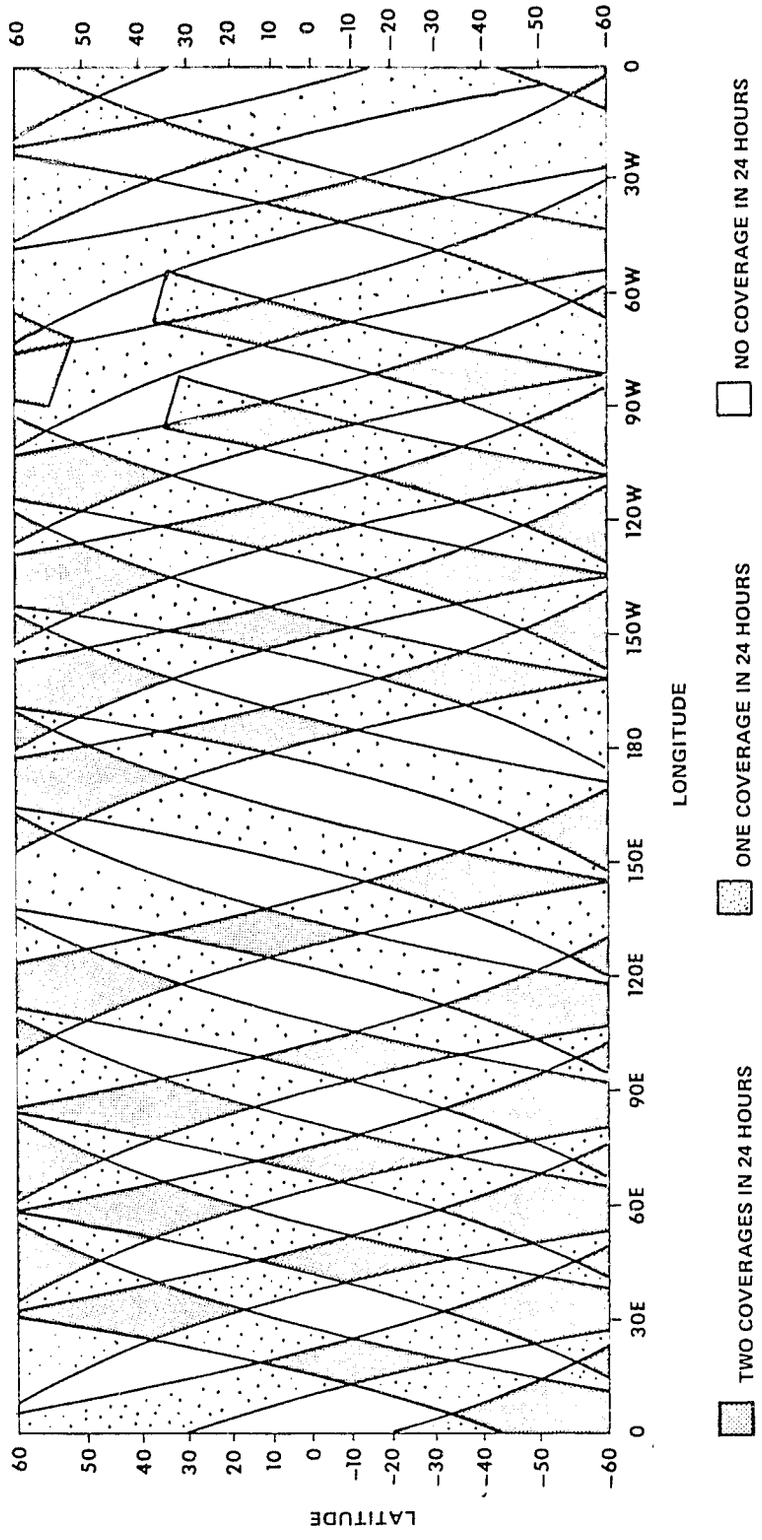

Figure 6. Typical ESMR coverage of the Earth for a 24-hour period. This coverage was derived from Nimbus-5 data. (From The Nimbus 6 User's Guide)

3.2 The ESMR-6 Data Set

The ESMR-6 data used in this study was recorded from 11 June 1976 through 30 August 1976 over the north central U.S. as shown in Figure 7. Prior to this period the ESMR was operated only on a half-time basis while after 15 September 1976 the horizontal polarization was unavailable. This period then represents the most intensive temporal coverage of the ESMR-6. Figure 8 shows the distribution of available orbits over the entire area, so that any one point in the area is viewed by the satellite only about 35 times out of 57 noon orbits and 40 times out of 72 midnight orbits.

3.2.1 Corrections Made to this Data

The microwave brightness temperatures are recorded on magnetic tape and available from the National Space Science Data Center (NSSDC) at the Goddard Space Flight Center (GSFC). Processing of the data at NSSDC includes calibrations which correct for thermal effects of the instrument, sidelobe effects, and polarization mixing. To investigate the completeness of this calibration procedure the data to be used in this study was averaged by beam position for vertical and horizontal polarization of noon and midnight orbits. The results of this averaging are shown in Figure 9. If all necessary corrections had been taken into account, the brightness temperature would be the same for each beam position in a long term average. As is seen in Figure 9 large variations of average brightness temperature with beam position exist, particularly in the outer 5 beam positions. These large variations in the outer positions are due to interference from the sidelobes of the phased array antenna. Because of the large and uncertain magnitude

Figure 7. Areal coverage of this study.

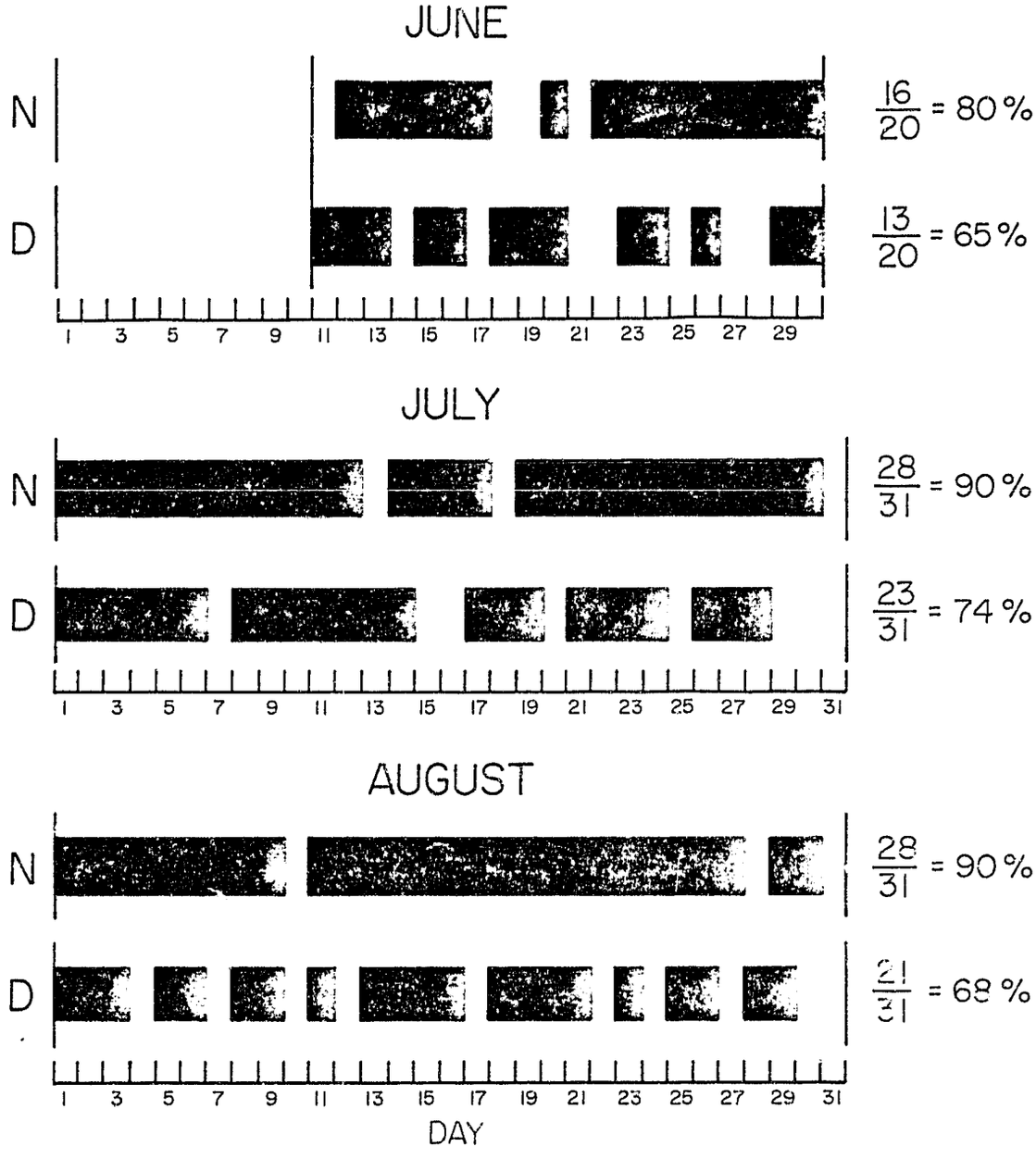

Figure 8. Distribution of available ESMR-6 observations used in this study.

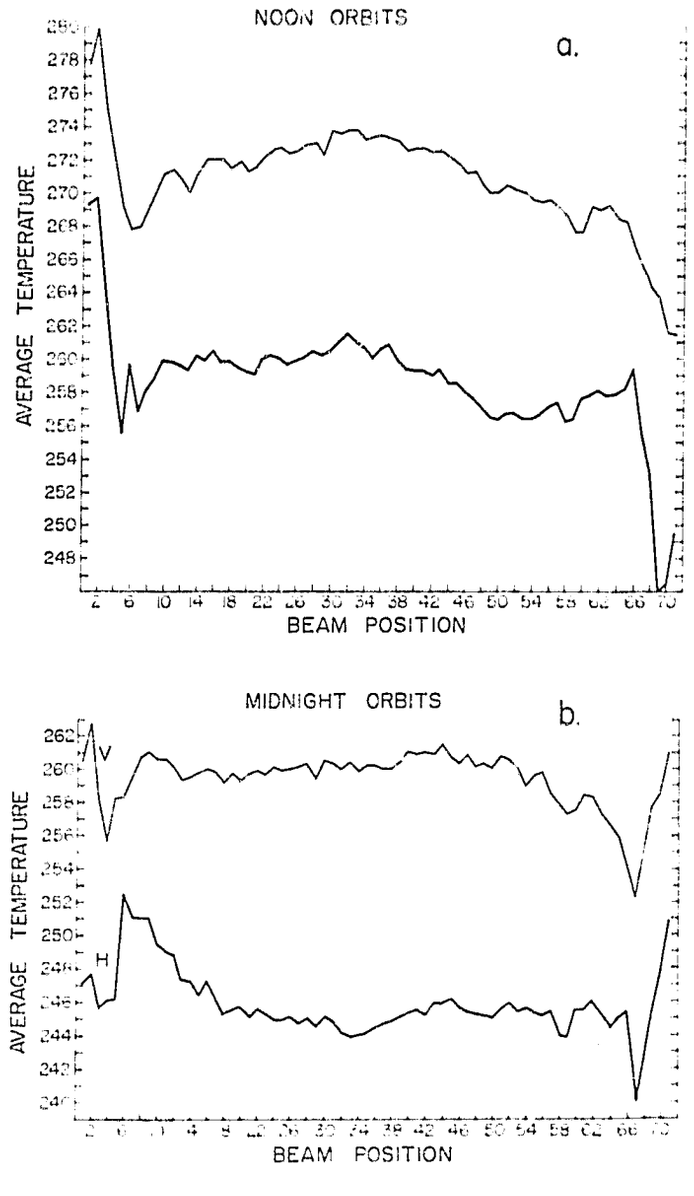

Figure 9. Average brightness temperature for each beam position along the ESMR-6 scan over all observations used in this study, (a) noon observations, (b) midnight observations.

of the sidelobe effects, beam positions 1-5 and 67-71 are useless for quantitative analysis. The variations over the remaining beam positions are probably due to imperfect polarization mixing corrections and slight lobe interference. To account for these variations an empirical correction was applied to all beam positions according to the difference of the beam position's average brightness temperature from the average brightness temperature of the center beam position (position 36). Table 1 lists the values subtracted from the brightness temperatures by beam position, polarization and time.

3.3 The Surface Raingage Data Set

In this study hourly rainfall observations are used for comparison with the satellite derived rainfall. These observations were obtained from Hourly Precipitation Data. The stations for which surface raingage observations are available are shown in Figure 10.

Rainfall occurrence has been tabulated for the hour of each pass of the satellite for those stations which lay within the area of ESMR-6 coverage. The results of the surface raingage observations are given in Chapter 4.

3.4 Thresholding Technique

For a non-scattering atmosphere, the microwave brightness temperature observed from a satellite may be written (Westwater, 1972):

$$T_b = \int_0^\infty T\alpha e^{-\int_0^s \alpha \frac{ds'}{\mu}} \frac{ds}{\mu} + \epsilon_s T_s e^{-\frac{\tau}{\mu}} + (1-\epsilon_s) e^{-\frac{\tau}{\mu}} \int_0^\infty T\alpha e^{-\int_0^\ell \alpha \frac{d\ell'}{\mu}} \frac{d\ell}{\mu} \quad (13)$$

where $\tau = \int_0^\infty \alpha \, ds$ is the total optical depth, ℓ and s are displacements

Table 1

Beam Position Brightness Temperature Correction

Beam Position	Vertical		Horizontal		Beam Position	Vertical		Horizontal	
	Day	Night	Day	Night		Day	Night	Day	Night
6	-5.7	-1.9	-0.9	8.1	37	-0.2	-0.2	-0.3	0.3
7	-5.5	-0.7	-3.8	6.7	38	-0.4	-0.2	-0.6	0.4
8	-4.4	+0.5	-2.5	6.6	39	-1.0	-0.2	-1.2	0.6
9	-3.3	0.8	-1.7	6.6	40	-0.8	0.8	-1.3	0.5
10	-2.3	0.4	-0.7	5.1	41	-0.8	0.7	-1.3	1.1
11	-2.1	0.4	-0.8	4.7	42	-1.0	0.8	-1.6	1.3
12	-2.7	-0.1	-1.0	4.4	43	-1.0	0.7	-1.2	1.3
13	-3.5	-0.9	-1.3	2.9	44	-1.3	1.2	-2.0	1.5
14	-2.4	-0.7	-0.4	2.8	45	-1.7	0.6	-2.0	1.4
15	-1.5	-0.4	-0.7	1.9	46	-2.3	0.2	-2.5	1.2
16	-1.5	-0.2	-0.1	2.8	47	-2.2	0.6	-2.9	1.4
17	-1.5	-0.4	-0.8	1.8	48	-3.0	0.0	-3.5	1.2
18	-2.0	01.0	-0.8	0.9	49	-3.5	0.1	-4.1	1.0
19	-1.6	-0.5	-1.2	1.1	50	-3.4	-0.1	-4.2	0.9
20	-1.2	-0.9	-1.4	1.3	51	-3.9	0.5	-3.9	1.1
21	-1.9	-0.5	-1.6	0.7	52	-3.3	0.3	-3.9	1.4
22	-1.3	-0.3	-0.6	1.2	53	-3.5	-0.2	-4.2	1.7
23	-0.9	-0.5	-0.4	0.9	54	-3.9	-.12	-4.2	1.2
24	-0.8	-0.1	-0.6	0.5	55	-4.0	-0.6	-3.9	0.8
25	-1.1	-0.3	-0.9	0.5	56	-3.9	-1.4	-3.5	0.4
26	-1.0	-0.2	-0.7	0.7	57	-4.4	-1.7	-3.2	1.0
27	-0.6	-0.1	-0.5	0.3	58	-4.9	-2.3	-4.3	-0.4
28	-0.5	0.1	-0.1	0.6	59	-5.8	-2.9	-4.2	-0.4
29	-1.2	-0.8	-0.3	0.1	60	-5.8	-2.7	-3.9	1.1
30	0.2	0.3	-0.1	0.7	61	-4.3	-1.8	-3.8	1.1
31	0.1	0.1	0.5	0.4	62	-4.5	-1.9	-3.5	1.0
32	0.3	-0.2	0.9	-0.2	63	-4.3	-2.9	-3.8	0.7
33	0.3	0.2	0.4	-0.5	64	-5.1	-3.6	-2.7	0.2
34	-0.3	0.3	0.1	-0.4	65	-5.3	-4.3	-2.4	0.4
35	-0.1	0.0	-0.5	-0.3	66	-6.7	-6.0	-2.1	0.7

$V_D(36)=273.5$ $V_N(36)=260.2$ $H_D(36)=260.6$ $H_N(36)=244.4$

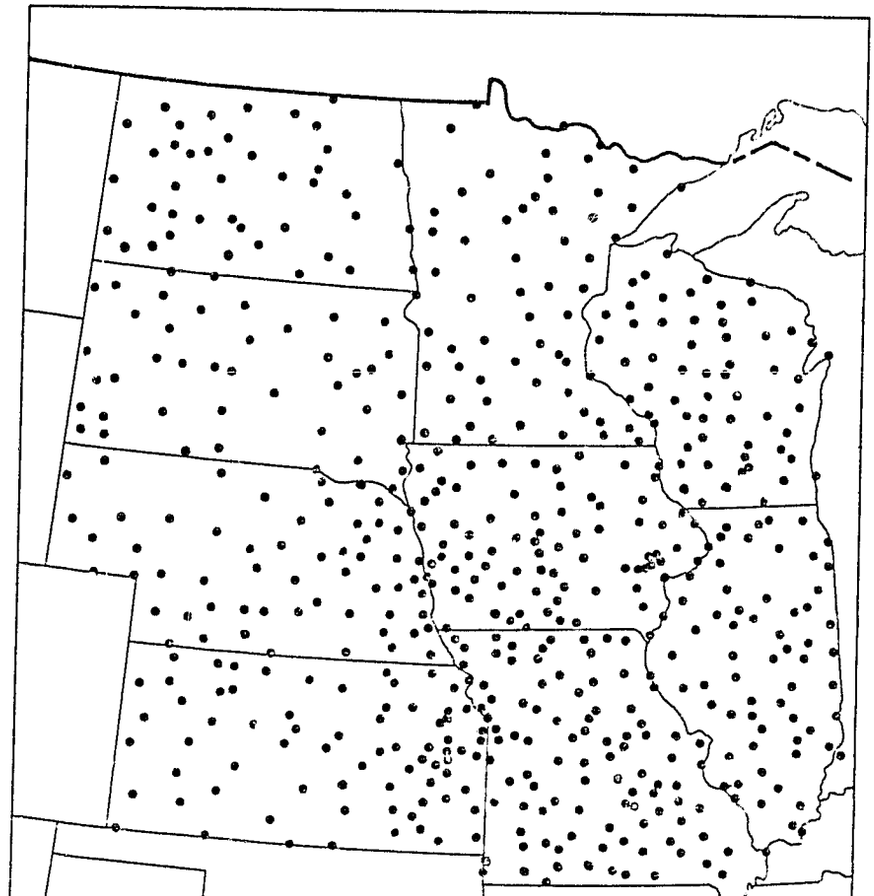

Figure 10. Distribution of surface raingages.

upward and downward respectively, ϵ_s and T_s are the emittance and temperature of the surface, T is the temperature as a function of height and $\mu = \cos\theta$ where θ is the zenith angle. T_b then is simply the sum of contributions from the emission of the atmosphere between the satellite and the surface, the emission of the surface and the reflection of the emission of the atmosphere incident downward on the surface. If we assume that total brightness temperature is a function of surface emittance and temperature only, that is variations in the vertical temperature profile and distribution of absorbing and emitting constituents are negligible, then equation (11) may be written

$$T_b = A + \epsilon_s T_s B + (1 - \epsilon_s)C \qquad (14)$$

where A, B and C are constants. Westwater (1972) has made calculations of the contributions to T_b for both the U.S. Standard Atmosphere and the 15°N Tropical Atmosphere. Table 2 lists the interpolated values of the terms in equation (14) for $\epsilon_s = .9$ and $T_s = 288$ for the U.S. Standard Atmosphere and $T_s = 299$ for the 15°N Tropical Atmosphere. It is apparent from Table 2 that at 37 GHz the dominant term in determining the total brightness temperature is the surface emission which accounts for 88% of the U.S. Standard Atmosphere total. Upward emission of the U.S. Standard atmosphere accounts for 12% while only 1% of the total brightness temperature is contributed by the reflected downward emission of the U.S. Standard Atmosphere. The 15°N Tropical Atmosphere is more moist and warmer than the U.S. Standard Atmosphere which results in a larger portion of the total brightness temperature being contributed by the atmospheric term. The result is that 18% of the total is added by upward atmospheric emission, 80% is added by the surface

Table 2

Numerical values of the terms in Equation (14) from Westwater (1972)

Term	U.S. Standard	15^{o}N Tropical
A	30.0 K	49.5 K
B	0.833	0.823
C	30.0 K	49.5 K
$\epsilon_s T_s B$	229.0 K	221.5 K
$(1-\epsilon_s)C$	3.0 K	5.0 K
T_b	262.0 K	276.0 K

emission and 2% of the total is added by the reflected downward emission of the 15°N Tropical Atmosphere. The results of this partitioning of the total brightness temperature show that the variations in the surface terms, emittance and temperature, will account for the majority of the variance in satellite observed brightness temperatures over land if large areas of scattering hydrometers are not present.

From Table 2 (term C) it is seen that the brightness temperature of the downward radiation incident on the surface is about 30 K and 49.5 K for a U.S. Standard and 15°N Tropical Atmosphere respectively. If water surfaces have an emittance of 0.5 then the addition of this term as seen by the satellite is about 15 K for a U.S. Standard atmosphere and 25 K for a 15°N Tropical Atmosphere. Nearly all of this added brightness temperature will be vertically polarized so that the brightness temperature in the vertically polarized channel will be higher than in the horizontally polarized channel. Therefore, to eliminate cold brightness temperature water surfaces from consideration, areas with greater than a 15 K difference between the vertical and horizontal channels are eliminated throughout this study.

Figure 11 shows the frequency distribution of observed microwave brightness temperatures from the vertically polarized channel over the area in Figure 8 at 0630 UT on 14 June 1976. The shape of the distribution is that of a Gaussian with a tail extending from the cold end of the distribution. This distribution which is typical for this area at this time of year, is comprised of two parts. First, the non-raining fields of view over the area make up the Gaussian part of the distribution with a characteristic standard deviation about some mean due to variations in atmospheric and surface radiative conditions. Second,

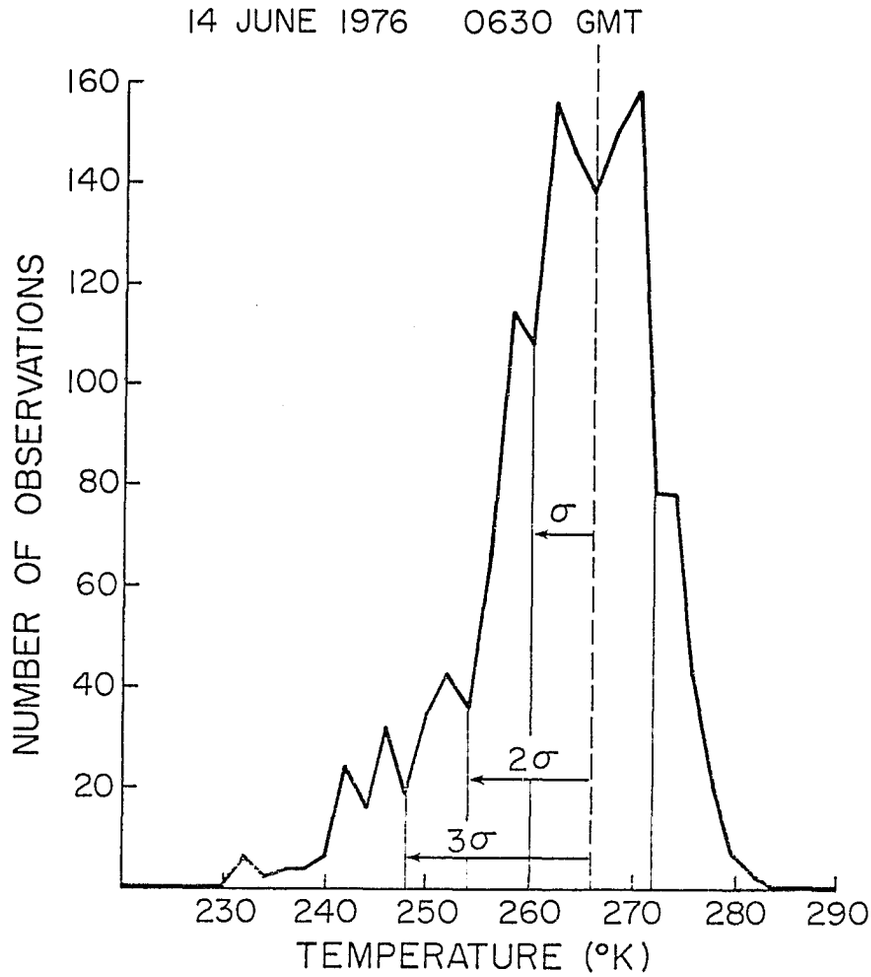

Figure 11. Frequency distribution of observed microwave brightness temperatures from the vertically polarized channel at 0630 GMT on 14 June 1976.

raining areas which decrease the observed brightness temperature of a field of view over land cause a displacement of temperatures towards the colder end of the distribution. The general Gaussian shape of the distribution is therefore distorted somewhat on the cold end by fields of view partially to completely filled with raining elements.

Rodgers et al. (1978) has shown statistically that indeed populations of raining and non-raining fields of view are separable. If the standard deviation of the non-raining distribution is known, the distribution may be subtracted from the whole leaving the raining fields of view.

The following numerical determination of the standard deviation and mean value of a contaminated Gaussian has been presented by Smith (1979). The functional form of a Gaussian distribution can be written

$$f(T) = f_{max} \exp\left\{\frac{-(T-\overline{T})^2}{2\sigma^2}\right\} \tag{15}$$

where f is the number of observations of temperature T, f_{max} is the maximum number of observations for any one temperature, $\overline{T}$ is the average temperature or the temperature of maximum observation, and σ is the standard deviation. Given three points along the distribution say (f_i, T_i), (f_j, T_j) and (f_k, T_k) such that $T_i < T_j < T_k$ then

$$\ln f_i - \ln f_j = \frac{-1}{2\sigma^2} (T_i^2 - T_j^2) - 2\overline{T}(T_i - T_j) \tag{16}$$

$$\ln f_i - \ln f_k = \frac{-1}{2\sigma^2} (T_i^2 - T_k^2) - 2\overline{T}(T_i - T_k) \tag{17}$$

which are two equations with the unknowns σ and $\overline{T}$. If $\alpha = \frac{\ln f_i - \ln f_j}{\ln f_i - \ln f_k}$ and $\beta = \frac{T_i - T_j}{T_i - T_k}$ then

$$\overline{T} = \frac{1}{2} \frac{(1-\alpha)\ T_i^{\,2} - T_j^{\,2} + \alpha T_k^{\,2}}{(1-\alpha)\ T_i - T_j + \alpha T_k} \tag{18}$$

and

$$\sigma = \sqrt{-\frac{1}{2} \frac{(1-\beta)\ T_i^{\,2} - T_j^{\,2} + \beta T_k^{\,2}}{(1-\beta) \ln f_i - \ln f_j + \beta \ln f_k}} \tag{19}$$

Equations (18) and (19) are applied to all possible combinations of three points which are safely in the non-raining portion of the distribution, namely the warm end of the Gaussian. The most common solutions then provide good estimates of σ and $\overline{T}$. The values of σ and $\overline{T}$ derived for the 14 June 1976 distribution are indicated in Figure 11.

The standard deviation is a measure of the width of the distribution. It is therefore feasible to use some multiple of σ below the mean as the lower temperature boundary of the distribution of non-raining fields of view. Figure 12 is a plot of percent of the total Gaussian distribution below the mean minus some multiple of the standard deviation vs. the multiple of the standard deviation. For a threshold of two standard deviations below the mean of the distribution less than 2% of the total non-raining fields of view remain below the threshold. Since these 2% (on the order of 25 fields of view) are expected to have little spatial organization they will be eliminated from the climatology by only accepting connected fields of view below the threshold as raining areas. Also, misclassification of non-raining fields of view can be avoided by examining observed surface temperatures. If large areas of cold surface temperatures exist in the area, say behind a cold front,* fields of view below the threshold in these areas may be eliminated.

---

* Certainly along the cold front where precipitation is highly possible all connected fields of view would be accepted as raining areas in the climatology.

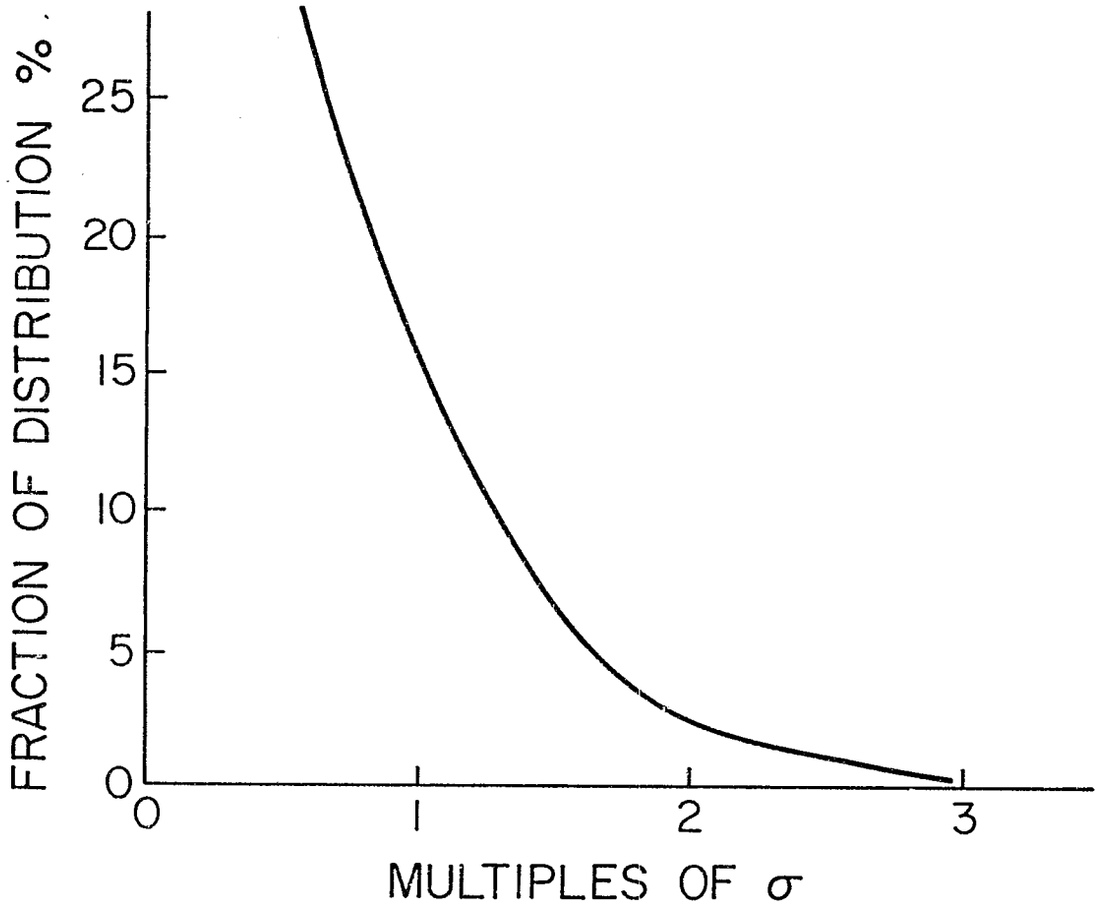

Figure 12. Fraction of a Gaussian distribution less than some multiple of the standard deviation of the distribution below the mean of the distribution.

3.5 Surface Temperature vs. Brightness Temperature

Frequency distributions of surface temperature from the 43 first-order observing stations in the area (Local Climatological Data) have been compared to the satellite brightness temperature distributions to examine the relationship between the two quantities. Figure 13 is a plot of modal brightness temperature vs. modal surface temperature for the area of the study. Daytime cases are open circles and nighttime cases are closed circles and only orbits which covered more than 30 of the 43 surface temperature stations are shown. Assuming an emittance of 0.9 yields the calculated curves for the 15°N Tropical and U.S. Standard atmospheric temperature and moisture profiles from Westwater (1972).

The relationship for daytime cases appears to be well approximated by the 15°N Tropical Atmosphere. The nighttime cases lie along the curve describing nearly surface emission. This infers that the nighttime radiative conditions are such that the addition of atmospheric emission to the brightness temperature is in general cancelled by a decrease of brightness temperature due to the opacity of the atmosphere. The above conclusions are based on the assumption that observed surface temperature (which is actually air temperature) closely approximates the average surface emitting temperature within a field of view or that at least on the average over the area this is true. One would expect that daytime surface emitting temperatures would be somewhat higher than air temperature and that nighttime surface emitting temperatures would be somewhat cooler than air temperatures. If this were the case then the daytime and nighttime cases would be more co-linear along a line lying between the 15°N Tropical curve and the surface emission curve.

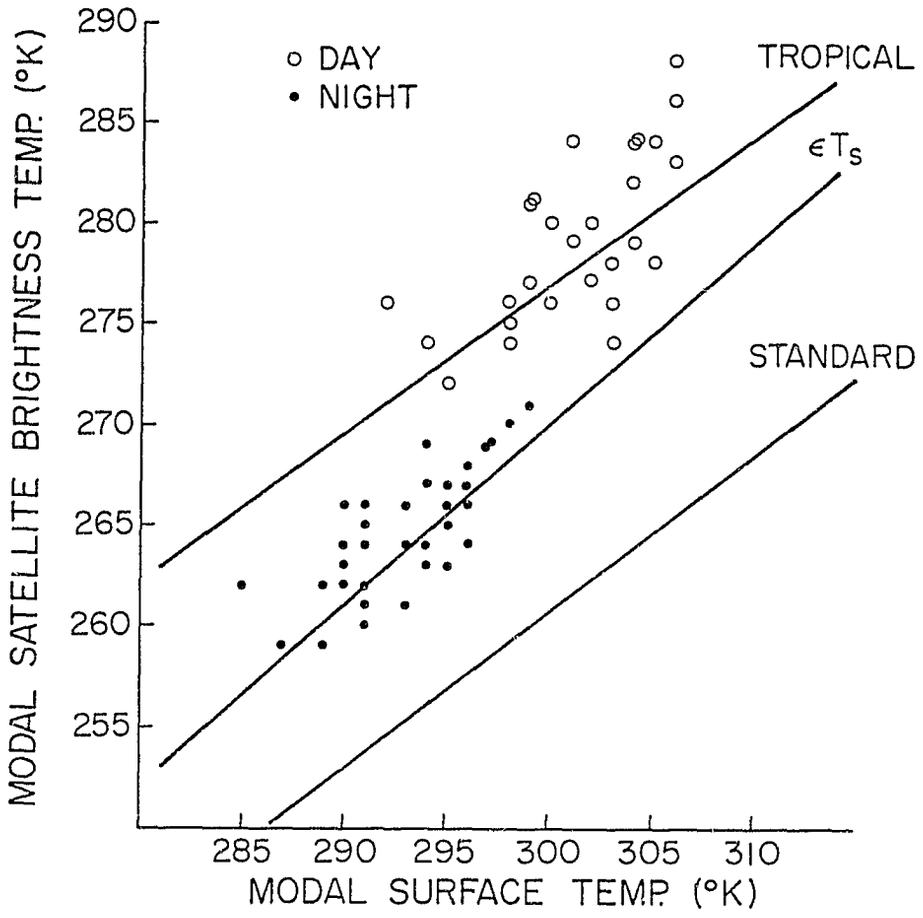

Figure 13. Modal brightness temperature vs. modal surface temperature. Open circles are daytime cases, closed circles are nighttime cases. (Only orbits which covered more than 30 of the 43 surface temperature stations are shown.)

3.6 Classification of Raining Areas

In preparing the precipitation frequency from the ESMR-6 observations the following information sources were used:

1) Microwave brightness temperatures: Areas where the brightness temperatures were less than 2 standard deviations below the mean of the distribution of non-raining brightness temperatures were taken as possible raining areas.

2) Spatial distribution of possible raining areas: Only areas with 2 or more adjoining fields of view were taken as possible raining areas.

3) Simultaneous THIR images: Images by the Temperature-Humidity Infrared Radiometer (THIR) (McColloch, 1975) also on board Nimbus 6 were used to assure the presence of clouds over the raining areas. THIR images were available for about 60% of the daytime ESMR-6 observations over the area of this study, while no nighttime THIR images were available.

4) Surface temperatures: Surface temperatures observed at noon and midnight at the 43 first-order stations were examined so that large areas with cold surface temperatures could be discounted as raining areas. Identification of these areas were aided in that the fields of view with brithtness temperature less than the threshold were scattered throughout the area and showed little or no organization.

5) Surface Relative Humidity: Midnight observations of surface relative humidity were examined so that areas with high probability of dew formation could be discounted as raining areas.

Relative humidities >90% were considered to indicate the possibility of dew formation. Again, identification of these areas was aided by the unorganized spatial distribution of fields of view below the threshold in these areas.

6) Polarization of the microwave brightness temperatures: As throughout this study only fields of view with low polarization (vertical channel not greater than 15 K higher than the horizontal channel) were considered. This eliminates water surfaces from consideration.

Figure 14 is a flow diagram illustrating the decision process used to classify fields of view as raining or non-raining.

An example of a satellite derived precipitation area is shown in Figure 15. This is the corresponding area whose frequency distribution of brightness temperatures is shown in Figure 11; 14 June 1976 at 630 GMT. Also indicated in Figure 15 are the rainfall amounts in hundredths of an inch recorded at the surface gages for the hour 600 to 700 GMT.

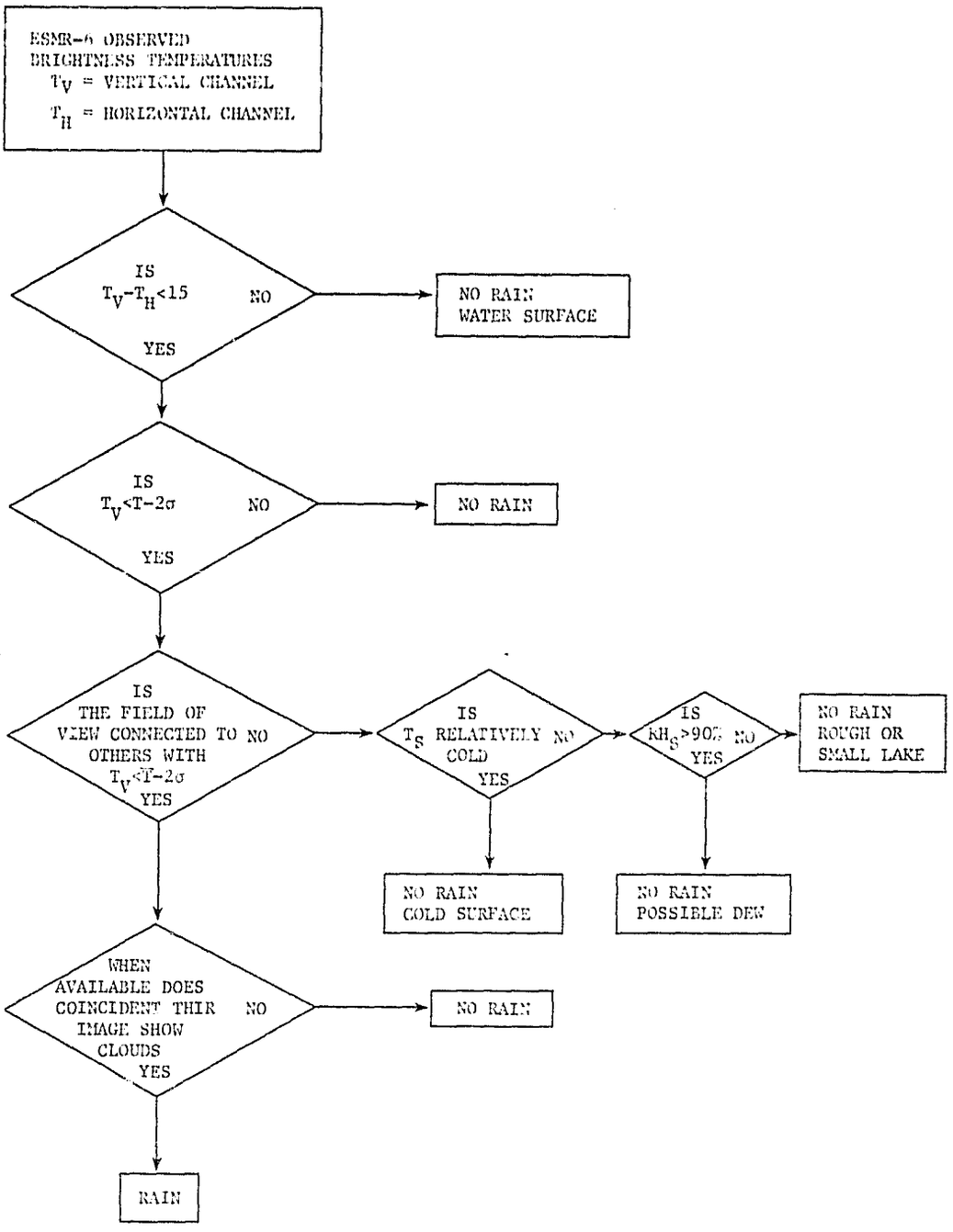

Figure 14. Flow diagram of the decision process used to classify fields of view as raining or non-raining. T_S is observed surface temperature, RH_S is surface relative humidity, $\bar{T}$ is the mean of the Gaussian distribution of non-raining areas, and σ is its standard deviation.

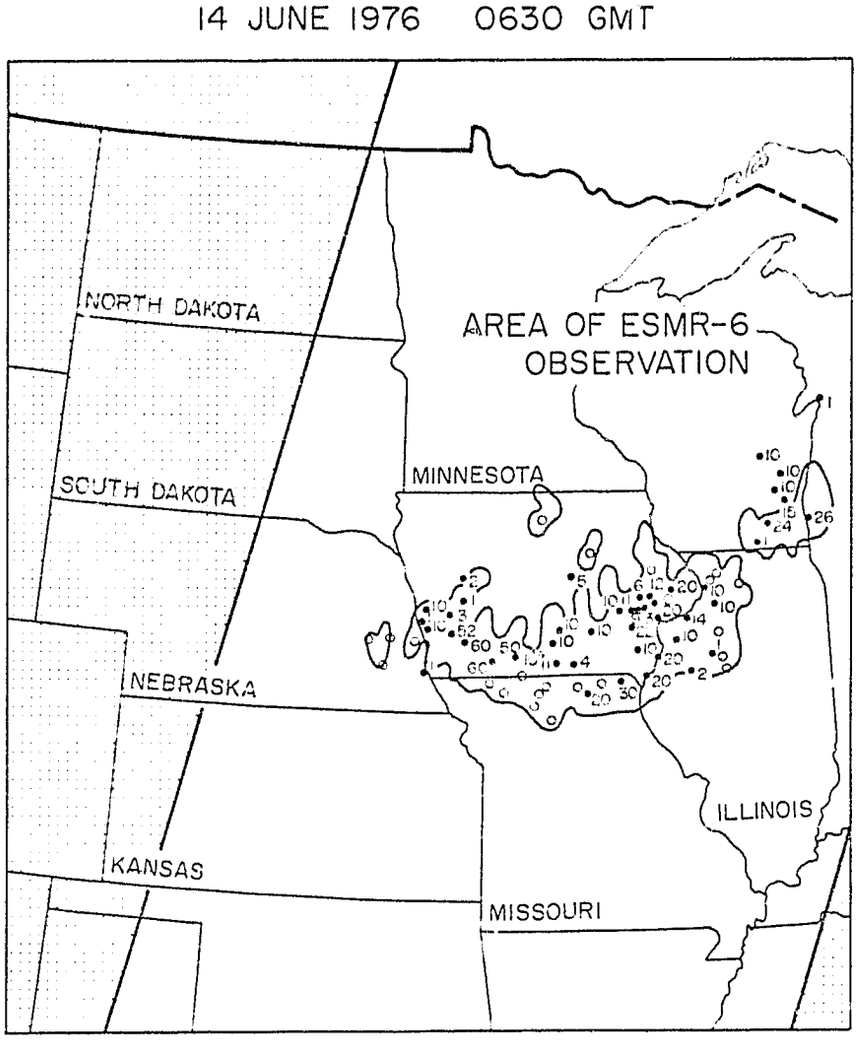

Figure 15. Satellite derived rain areas and amounts of rainfall (hundredths of an inch) at surface observing raingages for 14 June 1976 at 0630 GMT. Area of satellite observation is also indicated.

4.0 RESULTS AND DISCUSSION

4.1 Surface Raingage Results

Surface raingage observations (see Figure 10) have been analyzed for comparison with satellite derived precipitation frequency. Figures 16, 18, 20, 22, 24, 26, 28 and 30 show the results of the surface precipitation observations for June, July, August and total for the three month period (day and night observations being kept separate). Only surface observations which corresponded to the hour of a satellite observation were tabulated.

4.2 Results of the Satellite Derived Precipitation Frequency

The results of the analysis described in Section 3.6 are shown in Figures 17, 19, 21, 23, 25 and 27 and give the number of precipitation observations within 100 x 100 km squares for June, July and August, day and night observations being kept separate. Figures 29 and 31 give the precipitation observations as the percent of the total observations for the total three month period, again day and night observations are kept separate.

4.3 Discussion

4.3.1 The Climatology

The relationship between the surface observed precipitation via hourly observations with raingages and satellite derived precipitation via microwave brightness temperature analysis is not straight forward. The two systems are in fact measuring somewhat different quantities.

Raingages measure the precipitation which reaches the surface at a single point leaving large areas unobserved. Also, hourly observations

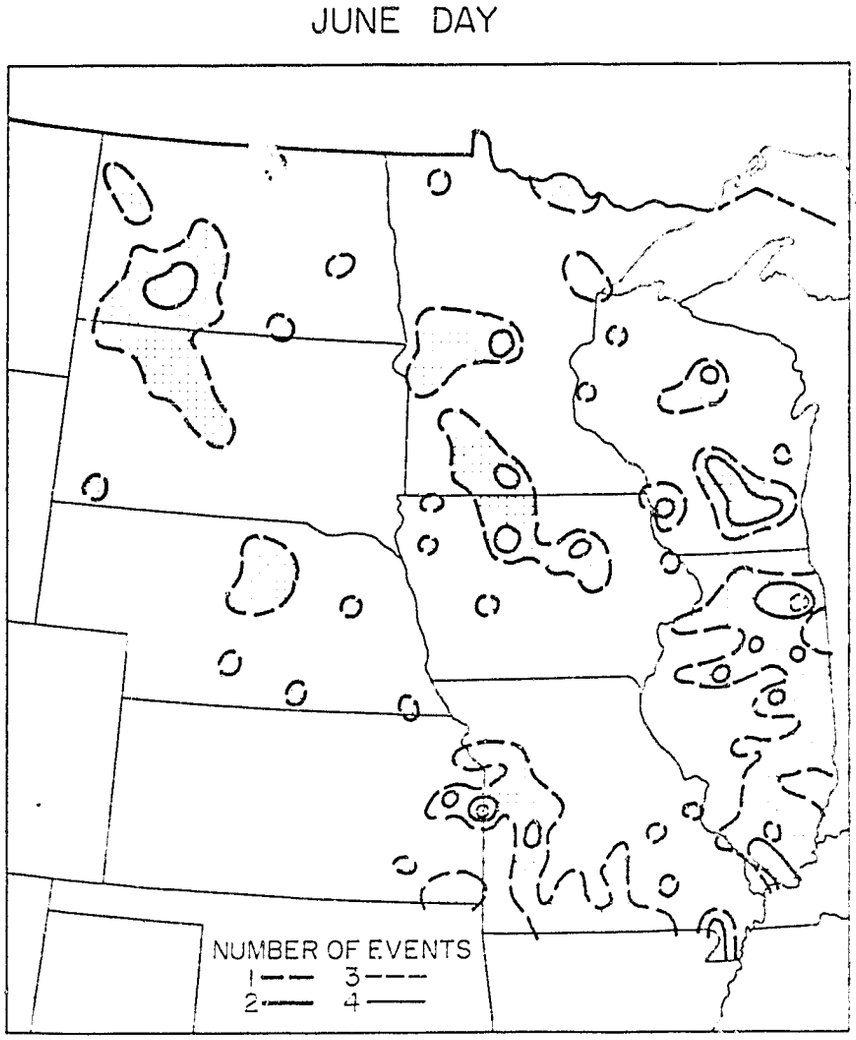

Figure 14. Distribution of surface raingage precipitation observations corresponding to June daytime orbits.

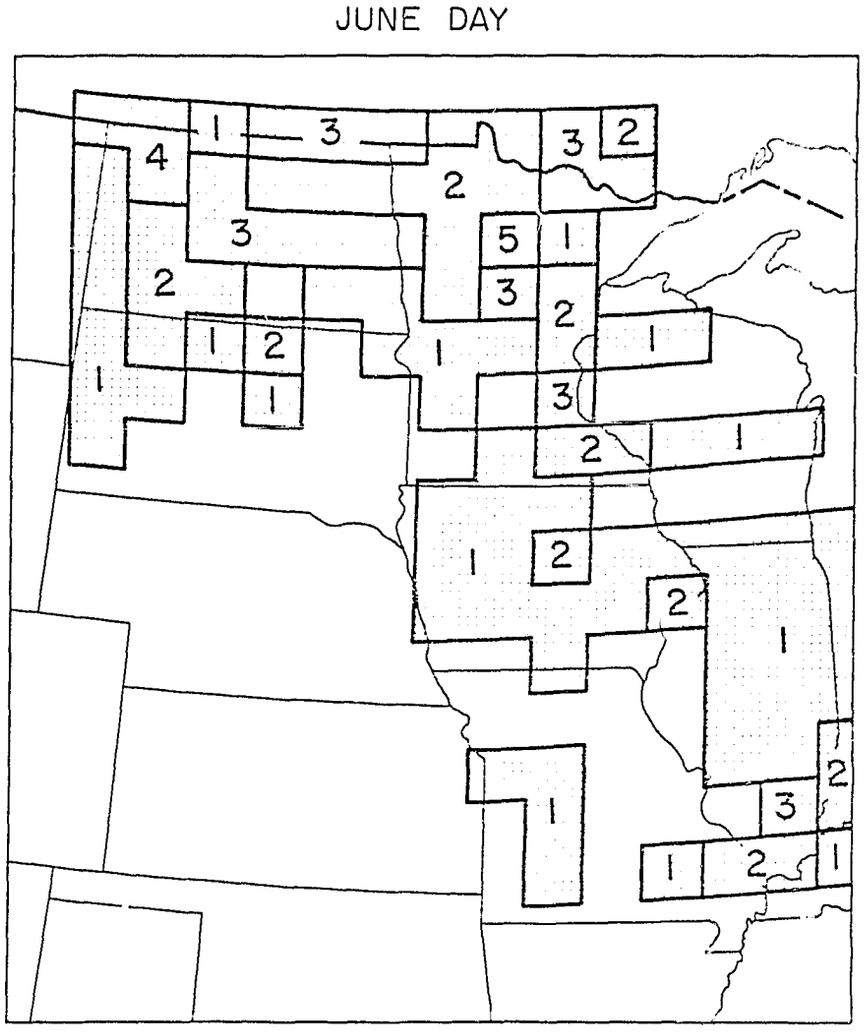

Figure 17. Distribution of satellite derived precipitation observations for June daytime orbits.

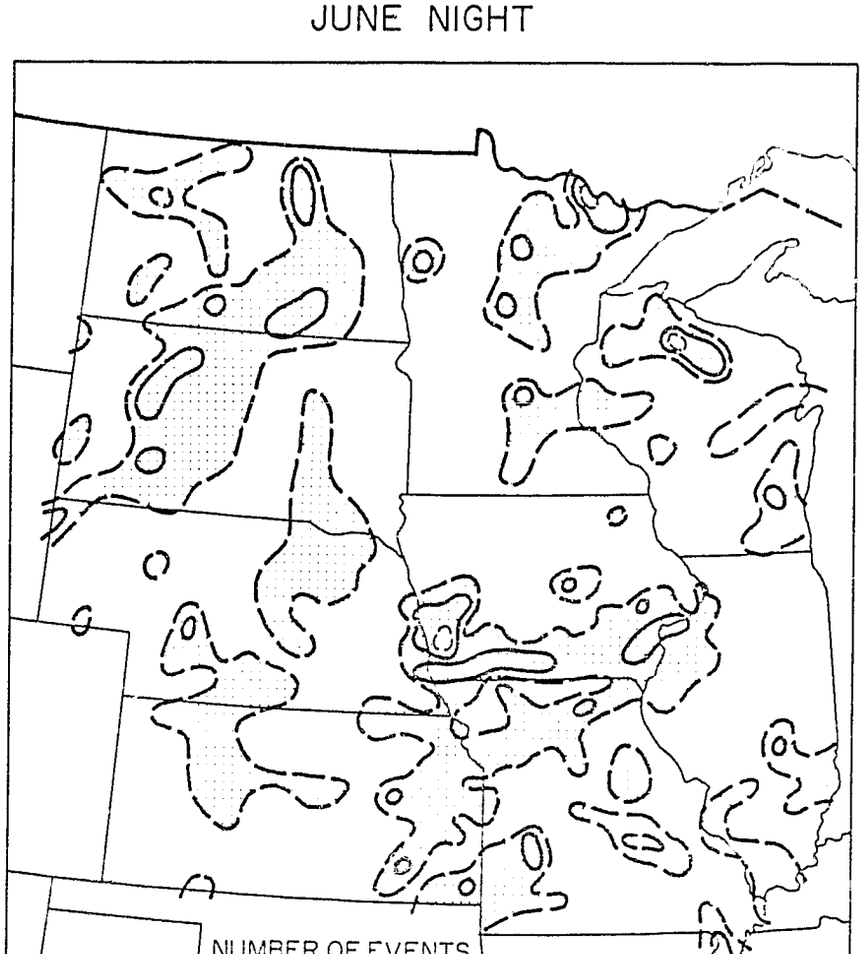

Figure 18. Same as Figure 16 but for June nighttime orbits.

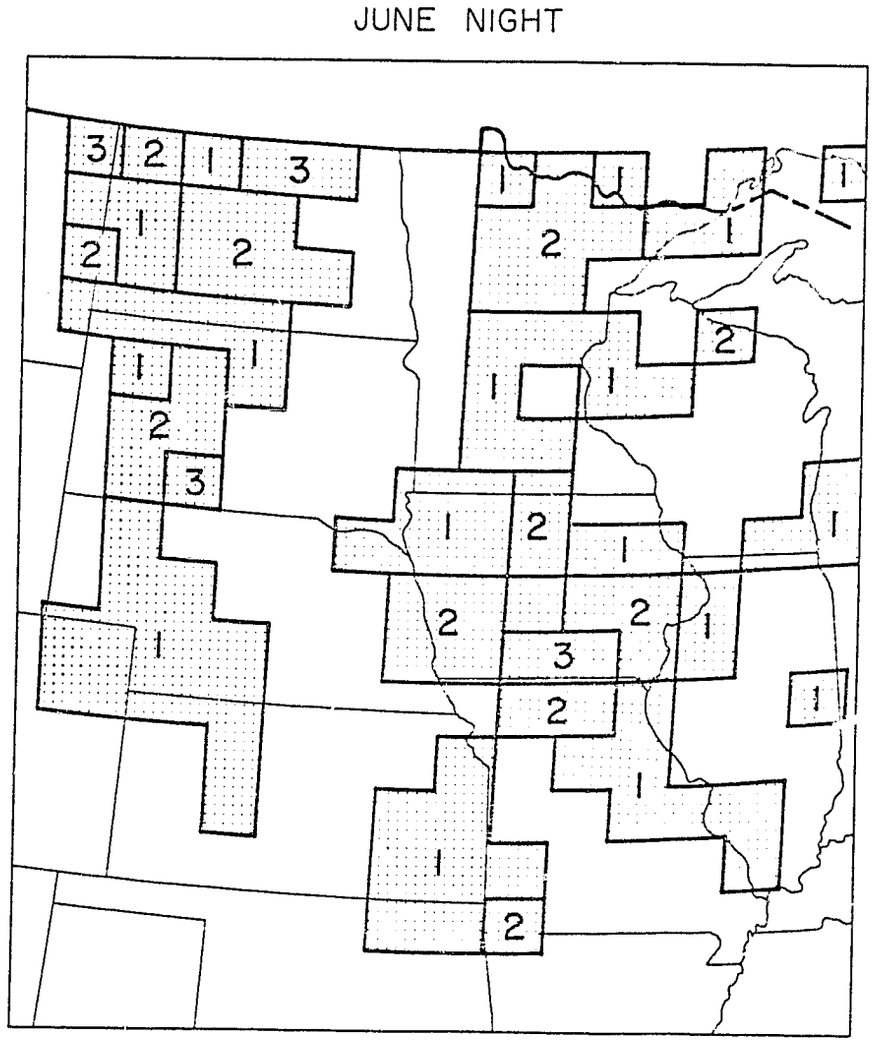

Figure 19. Same as Figure 17 but for June nighttime orbits.

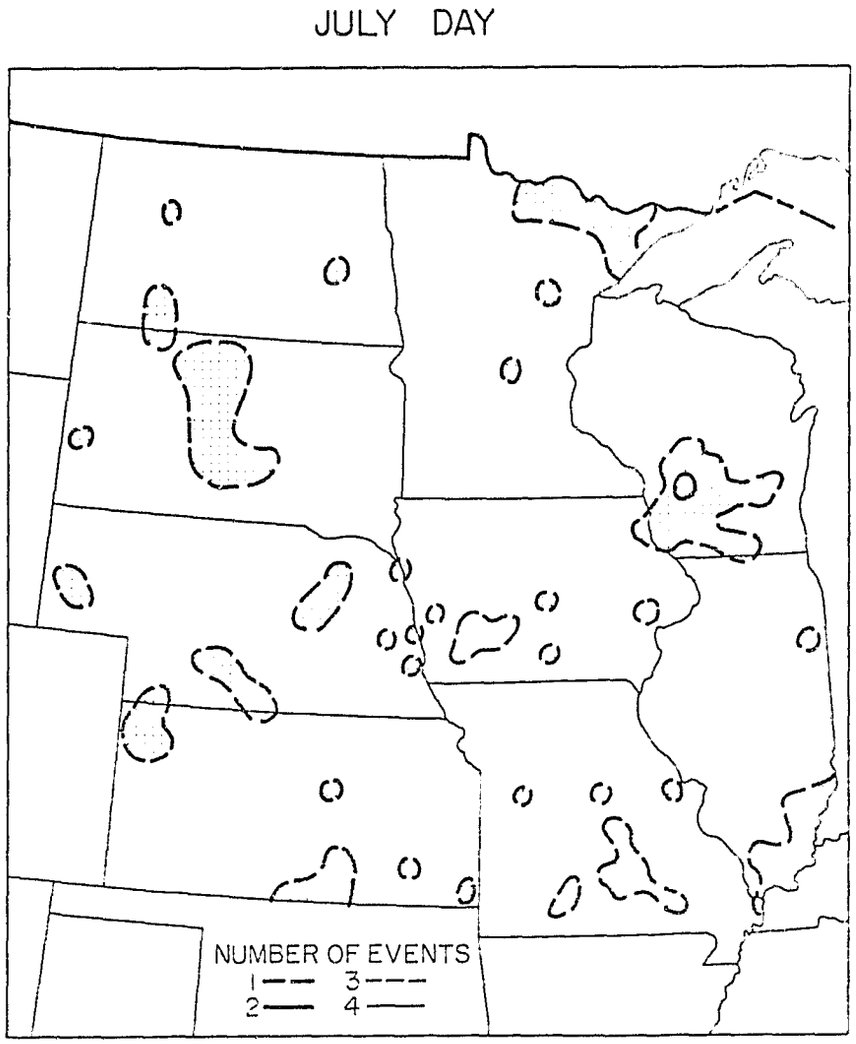

Figure 20. Same as Figure 16 but for July daytime orbits.

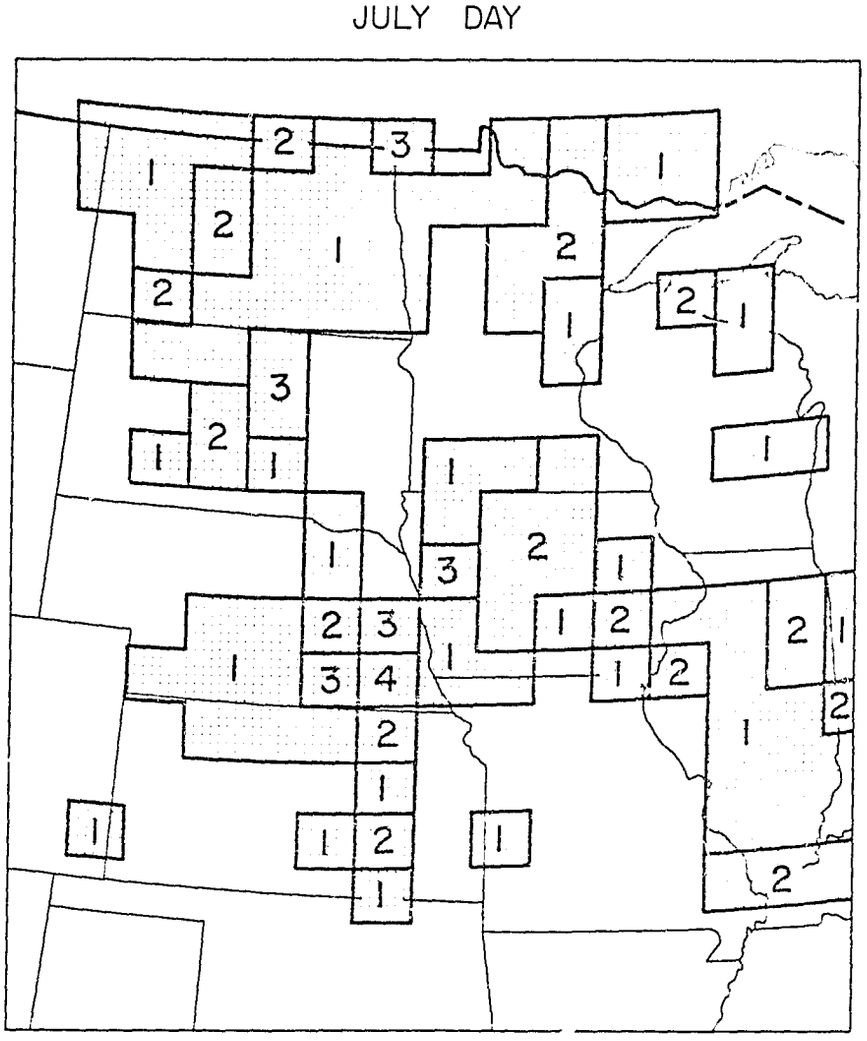

Figure 21. Same as Figure 17 but for July daytime orbits.

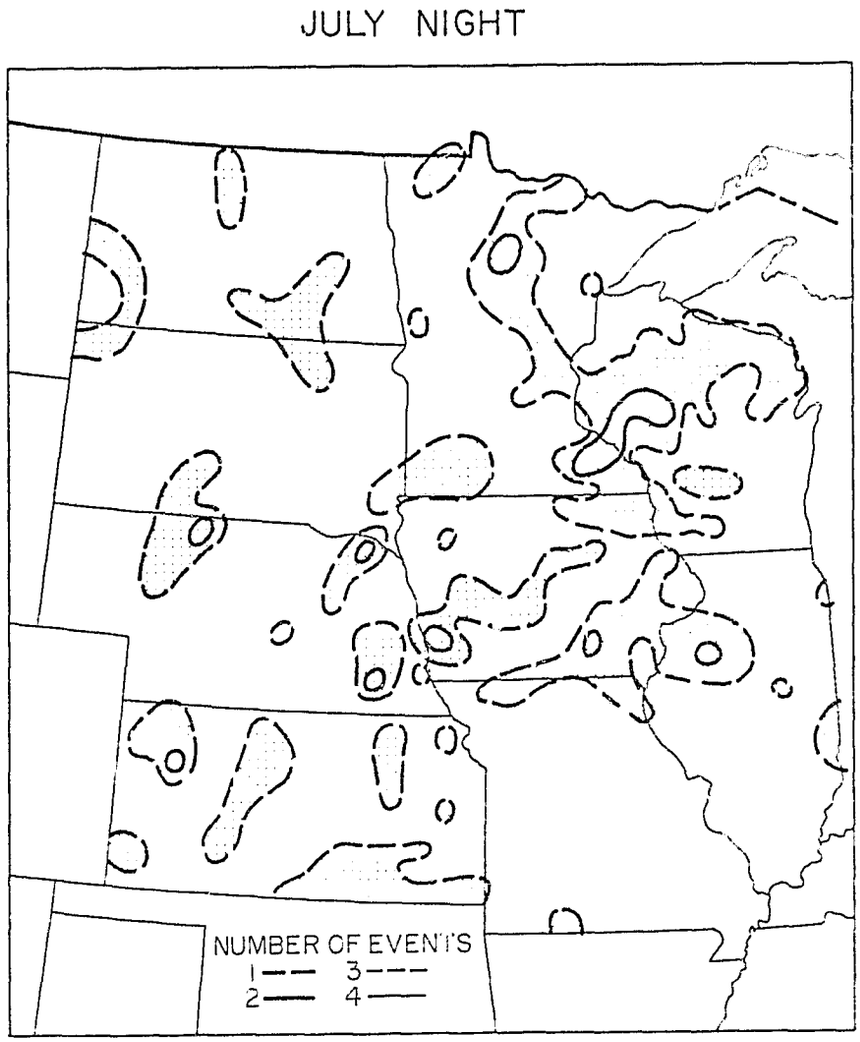

Figure 22. Same as Figure 16 but for July nighttime orbits.

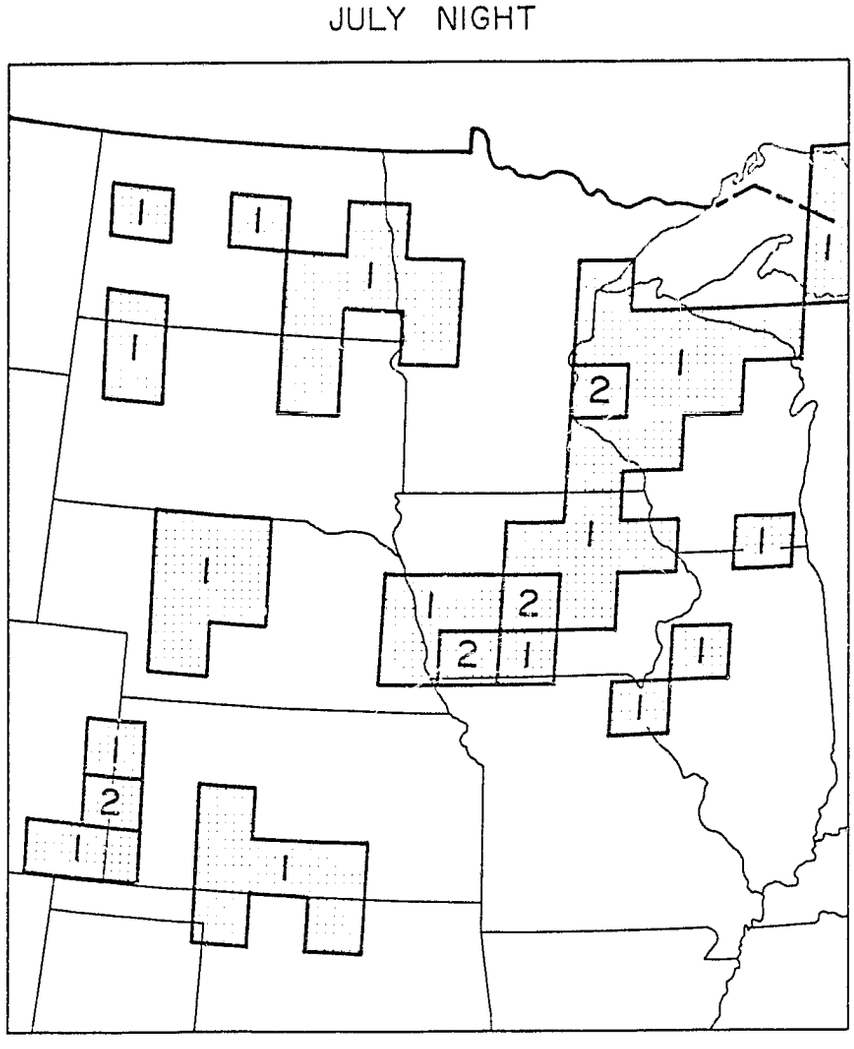

Figure 23. Same as Figure 17 but for July nighttime orbits.

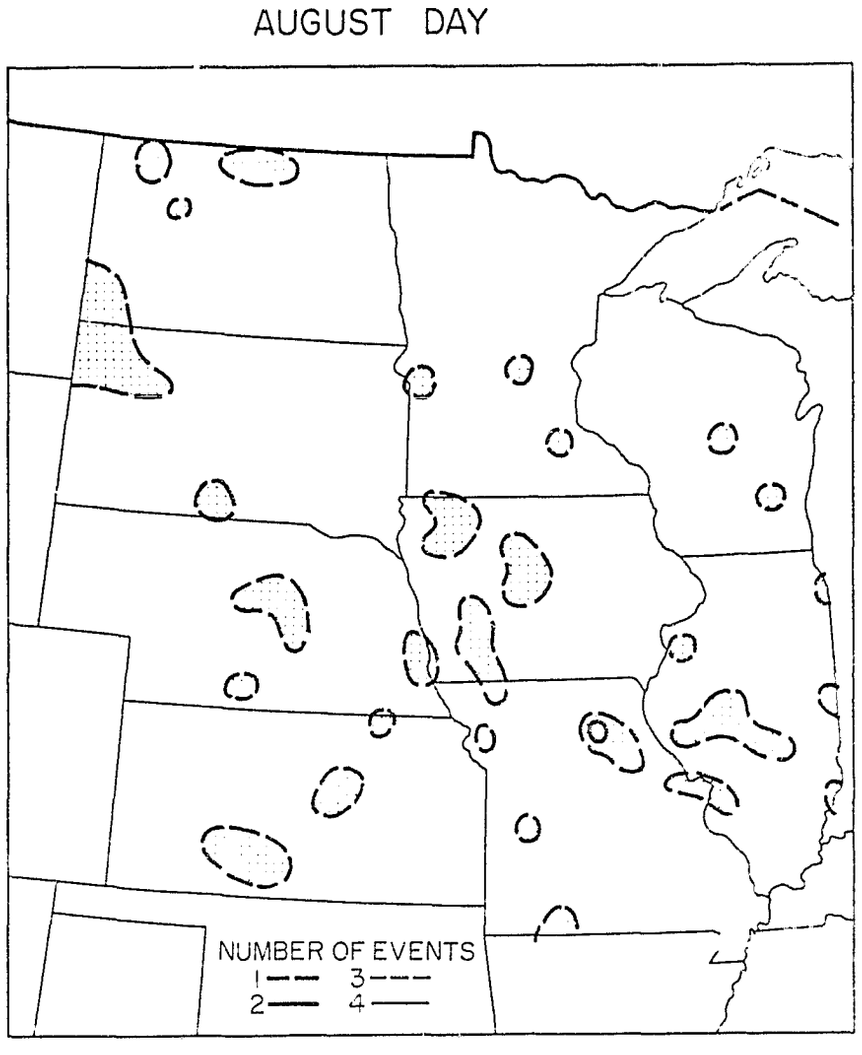

Figure 24. Same as Figure 16 but for August daytime orbits.

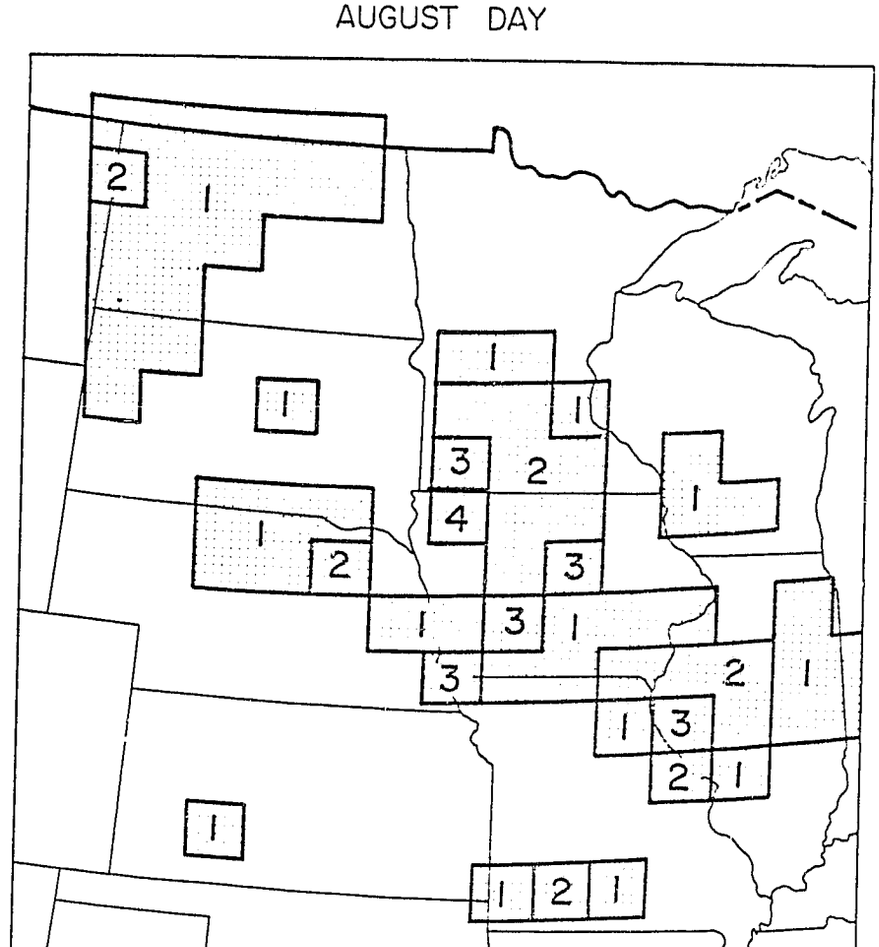

Figure 25. Same as Figure 17 but for August daytime orbits.

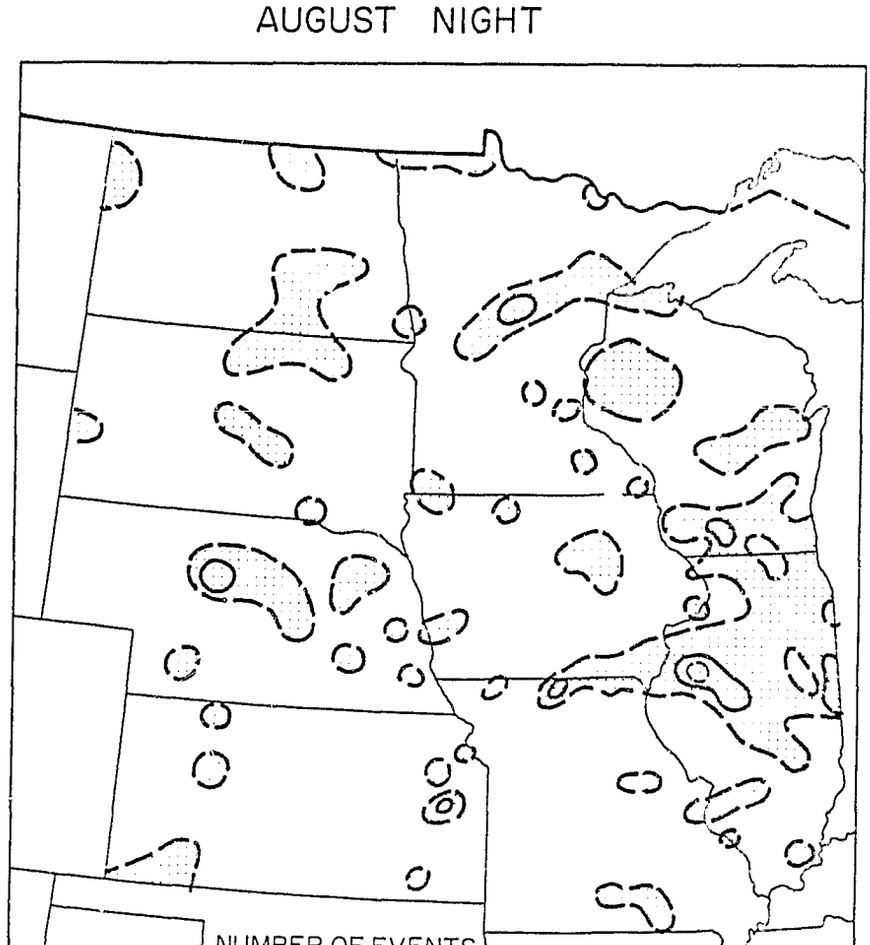

Figure 26. Same as Figure 16 but for August nighttime orbits.

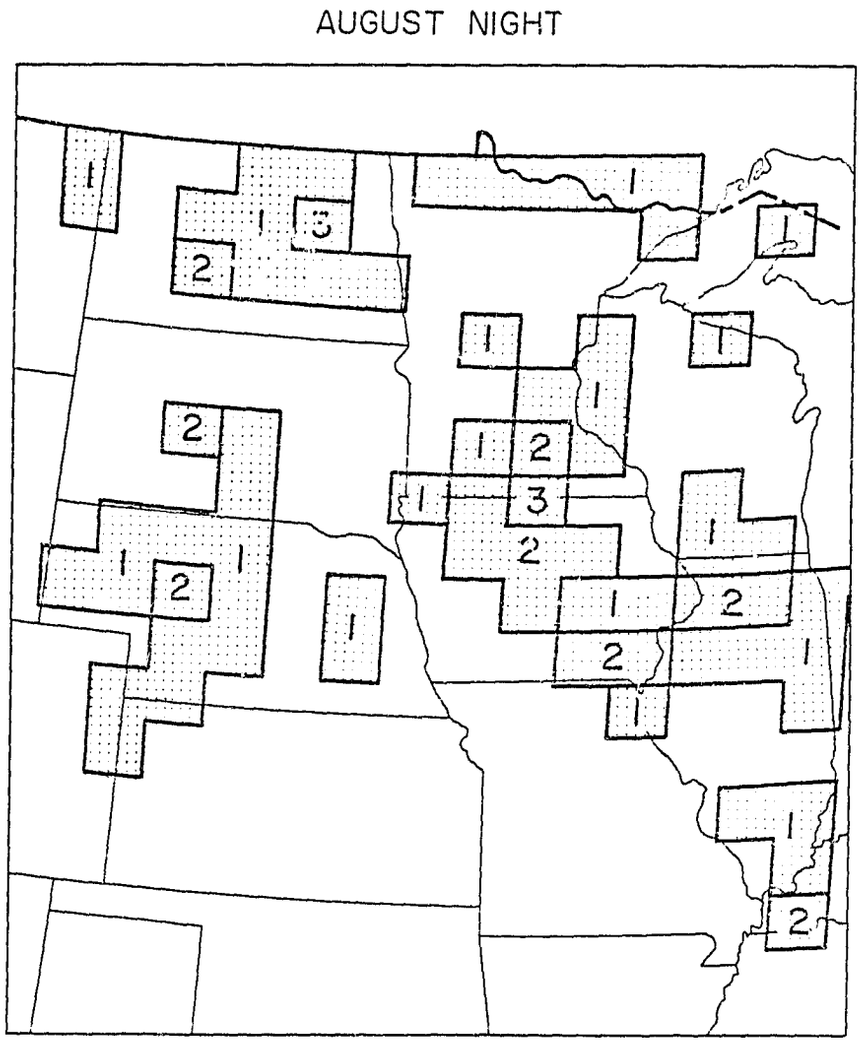

Figure 27. Same as Figure 17 but for August nightime orbits.

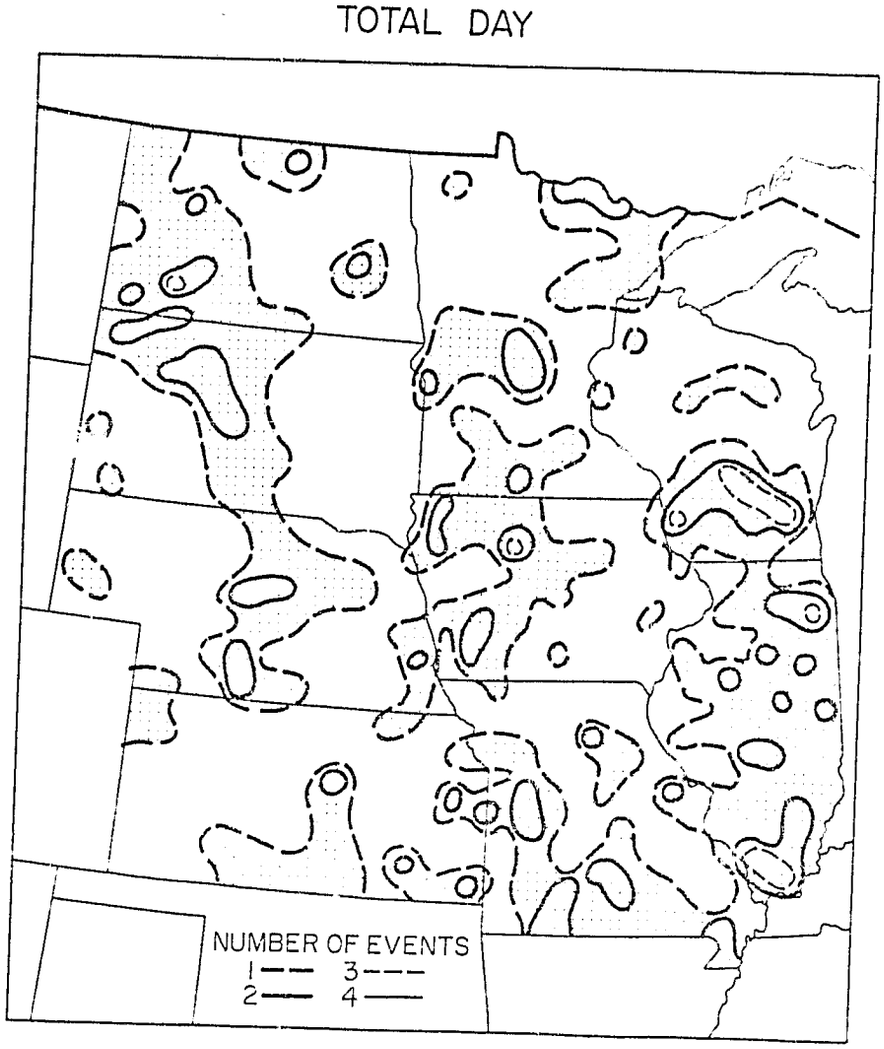

Figure 28. Same as Figure 16 but for the total three month daytime orbits.

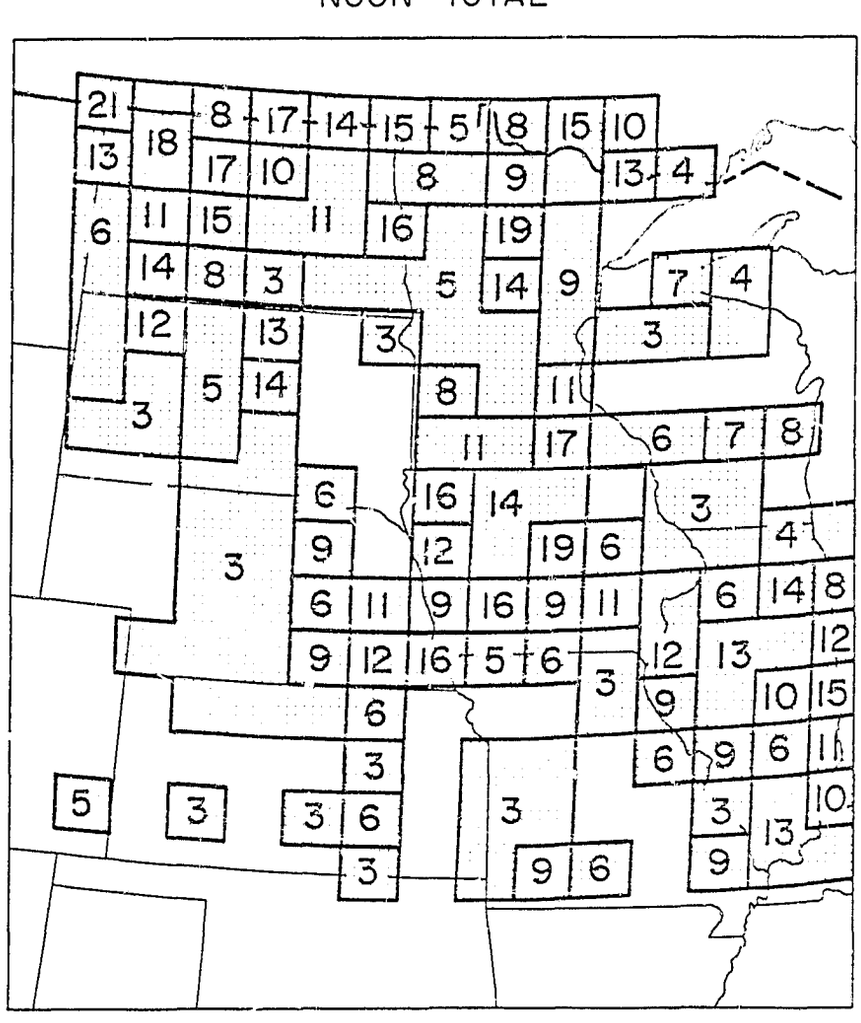

Figure 29. Precipitation frequency of the total three month period as derived by the satellite in percent of total observations.

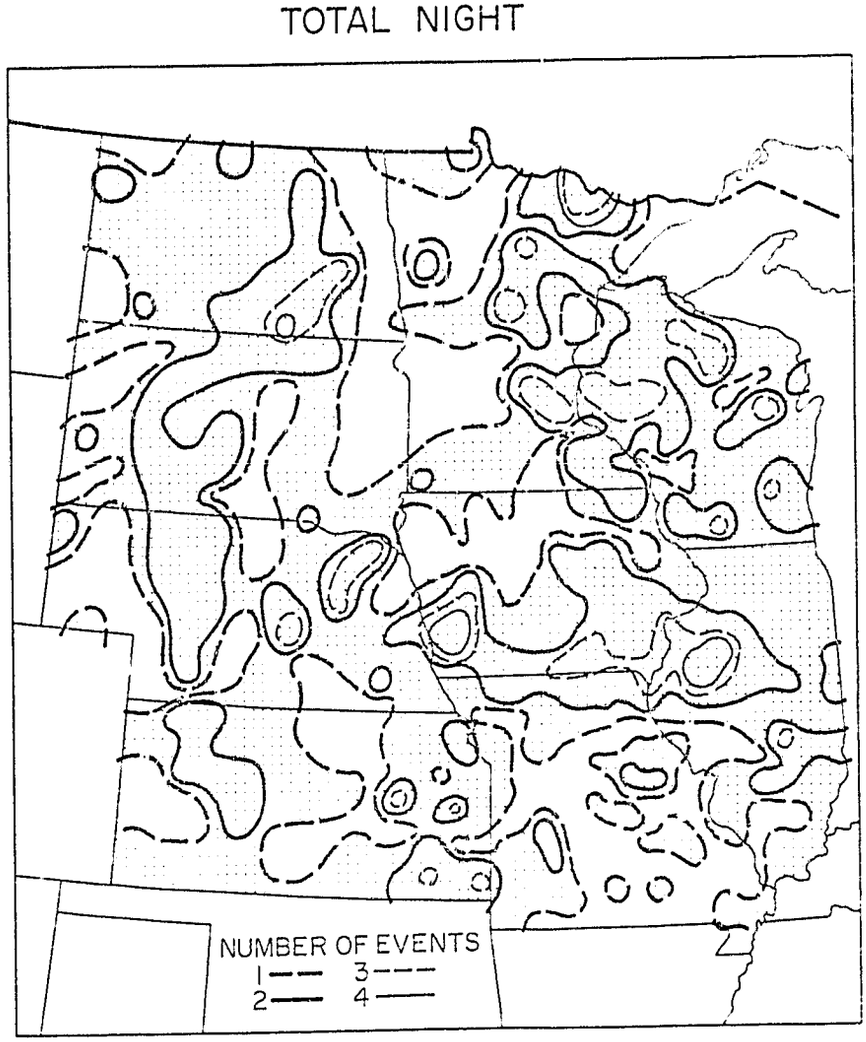

Figure 30. Same as Figure 16 but for the total three month nighttime orbits.

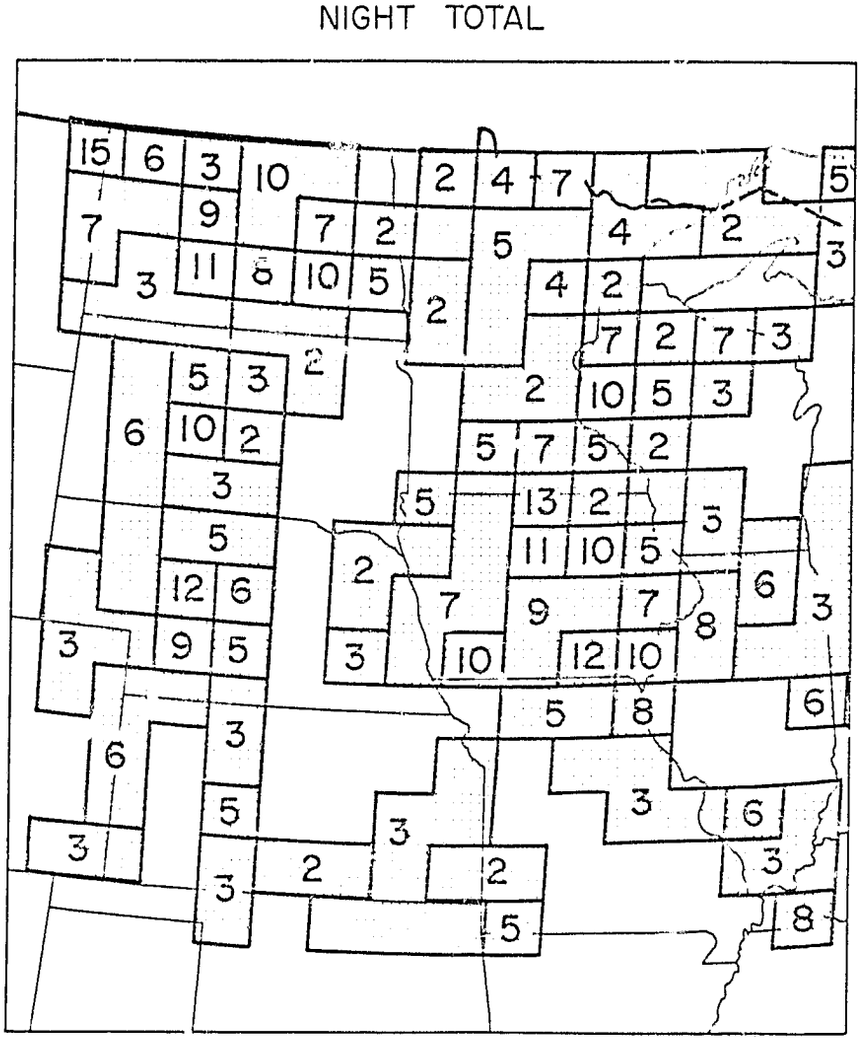

Figure 31. Same as Figure 29 but for the total three month nighttime orbits.

give the integrated rainfall over a complete hour so that more than a single raining system may contribute to a gage's recorded total.

The satellite observed scattering by rain drops which may or may not reach the ground. It "sees" all areas, however it integrates everything within one field of view (20 km x 42 km) into a single observation. Raining clouds must therefore be extensive enough or raining hard enough to affect the radiative condition of a large area and be observed by the satellite. The satellite also takes an effective "snapshot" of the area giving only an instantaneous view of the area's precipitation.

With the above differences in the measuring systems in mind, the major comparative features of the two analyses are discussed below.

JUNE (10th through the 30th)

Day - The absence of rain in Nebraska and Kansas are apparent in both the satellite and raingage observation. Relative maximums in the western Dakotas, central and southern Minnesota, northern Iowa and most of Illinois are also seen by both systems.

Night - Minima seen in both the satellite and raingage observations are in the eastern Dakotas, Nebraska and Kansas, Illinois, Wisconsin and southern Missouri. Maxima are seen in the western Dakotas, northeastern Minnesota, southern Iowa, and eastern Kansas.

JULY

Day - Rain events observed by the gages are very scattered over the area. The satellite observed substantially more rain events than the gages and the spatial correlation between the two systems of observation is only generally good. The minima in the eastern Dakotas and central Minnesota are apparent in both systems. Maxima in central South Dakota, eastern Nebraska and northeastern Minnesota correlate well. The areas of

rain in northern North Dakota, eastern Kansas and Illinois as seen by the satellite are not apparent from surface raingage observation.

Night - The correlation of the midnight observations is much better in July than for the noon observations. Minima in central Minnesota, South Dakota, Missouri and Illinois correlate well between the two systems. Maxima in North Dakota, eastern Minnesota to northern Wisconsin, Iowa and western Kansas show up well in both systems as well.

AUGUST

Day - As in July the gage observations are highly scattered and the satellite observes more events than do the raingages. The spatial correlation between the systems, however, is better than for the July noon observations. Correlative minima are in northern Minnesota, northern Wisconsin, eastern South Dakota, Kansas and Missouri. Maxima in western North Dakota, eastern Nebraska, western Iowa and western Illinois are also highly correlated.

Night - Good correlation is again apparent both spatially and in number of events for this nighttime case. Minima covering most of South Dakota, Kansas and Missouri are seen in both systems. The rain areas in North Dakota, Nebraska and northern Illinois are all seen in both the satellite observations and the raingages. The large number of rain areas as seen by the satellite in northern Iowa are not observed by the surface gages, however.

THREE MONTH TOTAL

Day - Spatial correlation is quite high although the satellite observes more rain events than do the gages. Figures 28 and 30 give rainfall in percent of total observations but due to July and August especially the number of events is quite high. The prominent minima

which show up are in eastern South Dakota, western Nebraska, most of Kansas, northern and eastern Missouri, eastern Iowa and northern Wisconsin. Maxima apparent in both systems are in western North Dakota, central South Dakota, central Nebraska, southeastern Missouri, western Iowa, northeastern and southern Minnesota, southern Wisconsin and most of Illinois. An extensive area of large percentages of rainfall is in northern North Dakota into Minnesota. This area contains the least dense raingage distribution (see Figure 10) so that a lot of scattered precipitation events could occur without being detected by any raingages.

Night - Spatial as well as quantitative correlation between the two systems is very good. Minima are seen in eastern South Dakota, western Minnesota, Kansas and Missouri all of which appear in both systems. The maxima which correlate well are in central North and South Dakota, western Nebraska, southeastern Kansas, Iowa, eastern Minnesota and western Wisconsin.

4.3.2 Regression of Satellite Observations on Raingage Observations

Tabulation of the raingage observations into number of events in 100 x 100 km square areas as with the satellite data has been done to compare quantitatively the results from the two systems of observation. To examine how the satellite observed precipitation is related to the surface raingage observations a linear regression analysis has been done.

The area has been divided into 4 quadrants and the results of the regression analysis in each quadrant are shown in Figures 32 and 33. The straight lines are the sample regression curves for each quadrant with X representing the raingage observations and Y the satellite

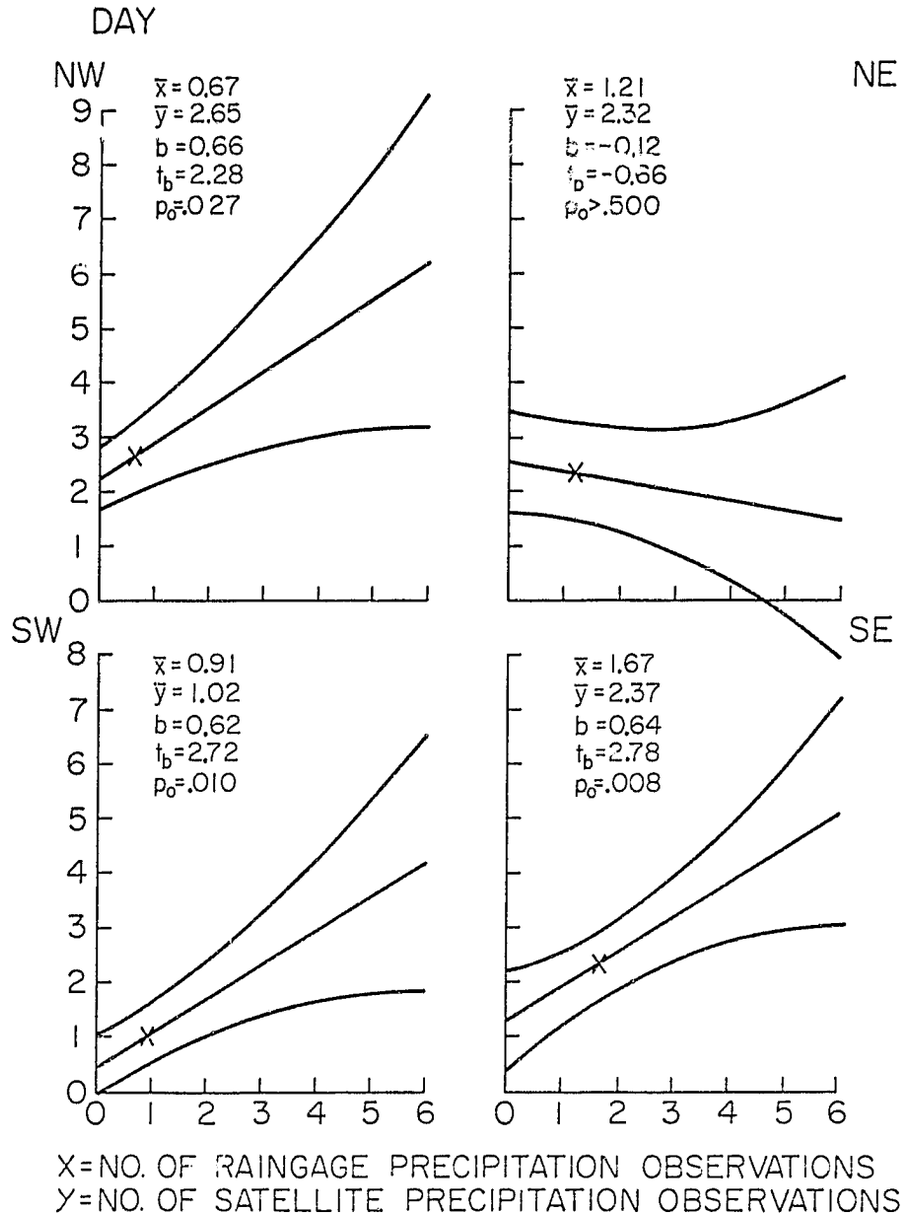

Figure 32. Results of regression analysis of the 4 quadrants for daytime cases. Straight lines are the regression curves and the hyperbolas indicate the 95% confidence intervals of the regression curve.

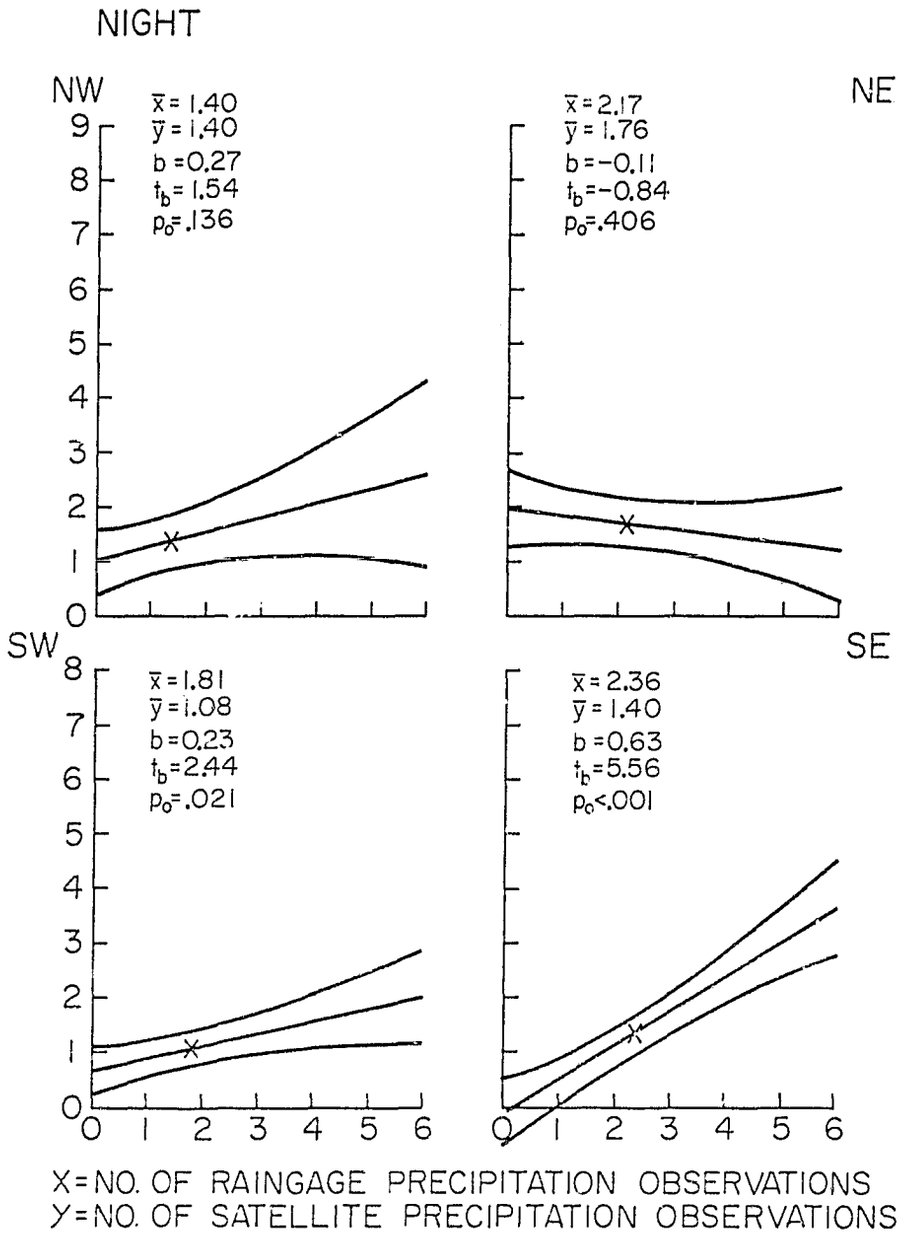

Figure 33. Same as Figure 32 but for nighttime cases.

observations. The hyperbolas above and below the regression curves are the 95% confidence intervals of the sample regression curves. That is we are certain to 95% that the regression curve lies within these limits. Also indicated on Figures 32 and 33 are the averages of the two variables (also indicated with an X on the regression curves), the sample regression coefficient b, t_b which is a test parameter on the significance of b and p_o which is the probability of b actually being zero, Y is then independent of X.

It is apparent that the best relationship between satellite and raingage observations is exhibited in the southern half of the area at both day and night (p_o is less than about 2% over the southern part of the area). The northeastern quadrant shows by far the worst relationship with large p_o (40.6% night and >50% day).

The southern half of the area is expected to be the best suited to the technique since warmer surface temperatures provide a better background with which to observe raining areas from the satellite. The colder surface temperatures to the north, particularly at night mask the raining areas. Also, the northeastern quadrant contains Lake Superior and Lake Michigan as well as numerous small lakes throughout Minnesota and Wisconsin. Although polarizing water surfaces have been eliminated from the analysis, small lakes which do not fill a field of view as well as rough wind blown lakes can create ambiguities in classification of raining areas.

It can be said with confidence (within 2 to 3%) that indeed satellite observed rainfall is related positively to surface observed rainfall over the northwest, southwest and southeast quadrants of the area during daytime cases and over the southern half of the area during nighttime cases.

4.3.3 Diurnal Variation

Wallace (1975) investigated the diurnal nature of precipitation frequency over the U.S. by examining hourly precipitation observations and has shown that over the north central U.S., including much of the area of this study, there is a pronounced near midnight maximum in thunderstorm and heavy rainfall frequency during the summer season. The same diurnal character is observed in the hourly raingage observations for June-August at least for midnight relative to noon. However, precipitation frequency derived from satellite microwave brightness temperatures shows more events around noon than near midnight.

From the average values of the two variables in Figures 32 and 33, it is seen that for the nighttime case the raingages observe more events than the satellite and for the daytime case the satellite observes more events than the raingages. Therefore, it is believed that the satellite method is biased, observing more rain events than actually occur for the near noon case and observing fewer events for the near midnight case.

The probable cause of the daytime bias is the larger variation in surface temperatures during the noon hours over the area which may be enhanced by cloud cover. That is areas overcast with non-raining clouds will have considerably lower surface temperatures than the surrounding sunlit areas causing their brightness temperatures to fall in the cold end of the frequency distribution and possibly below the threshold. Another possible cause may be that the satellite method during the day observes a large amount of rain which never reaches the ground but is evaporated into the warmer (relative to the midnight case) lower relative humidity air below cloud base. Both of these causes include the existence of clouds which could also account for the maintenance of the

spatial correlation between the two observing systems during the near noon cases. The "misclassified" (rain does not reach the ground) events by the satellite would tend to be near raining systems (other clouds) and simply expand the areal extent of the "real" rain areas.

The nighttime bias is due to the occurence of colder surface temperatures which mask the raining areas. From Figures 4 and 13, an area with a rainfall rate of 4 mm/hr has a brightness temperature of 255 K while a non-raining area with a surface temperature of 283 K (10^{o}C) would also be expected to have a brightness temperature of 255 K.

4.3.4 Total Precipitation

Maps of total precipitation for June, July and August 1976 (Weekly Weather and Crop Bulletin) are shown in Figure 34. It is apparent that, as in the noon and midnight observations previously discussed, June was the rainiest month over the north central U.S. followed by July and then August. Furthermore, the major spatial features of the total precipitation are seen as well in the satellite derived precipitation. Maxima in central Iowa and northern North Dakota and Minnesota (especially in June and August) are apparent in both sets of figures. Also, minima throughout much of South Dakota, eastern Nebraska and Kansas as well as parts of Missouri and Wisconsin are generally correlated over the three month period.

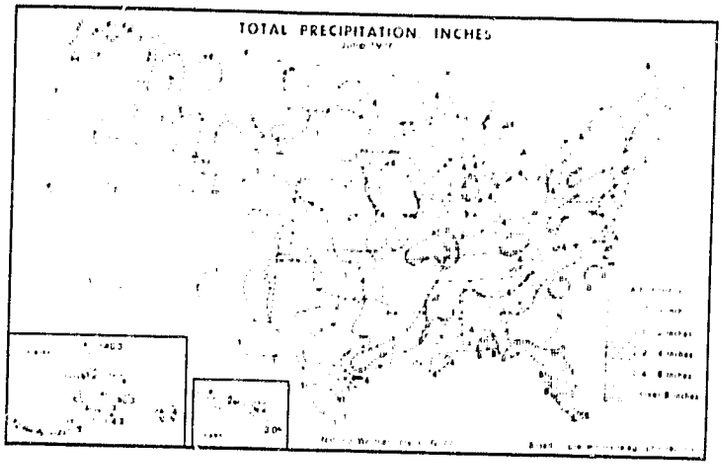

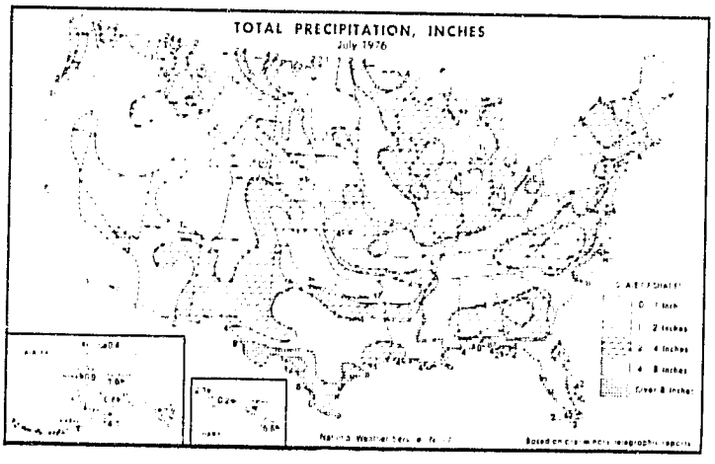

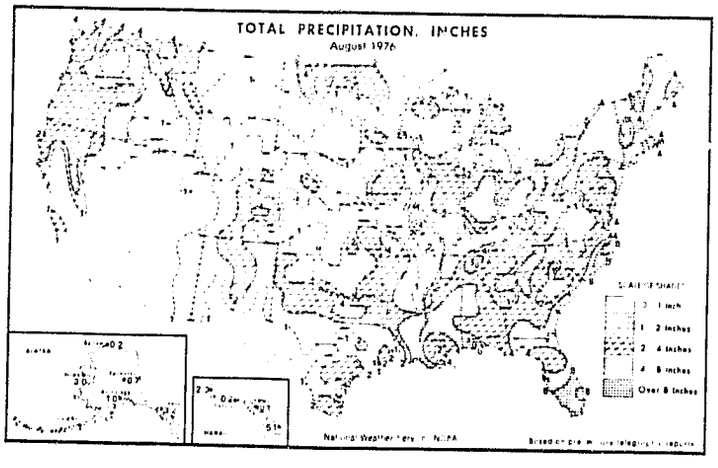

Figure 34. Total precipitation for June, July and August 1976. (From Weekly Weather and Crop Bulletin, 1976)

5.0 CONCLUSIONS

Microwave brightness temperatures from ESMR-6 have been analyzed to determine raining areas over the north central U.S. during the months June through August 1976. The precipitation frequency of the area derived by the satellite has been compared with that derived from hourly surface raingage observations. Both noon and midnight cases are seen to exhibit a positive relationship over much of the area between satellite observed rainfall events and surface raingage events. Only the northeast quadrant of the area shows little relationship. The satellite method is biased such that more events are observed during the daytime cases than actually occur at the surface and fewer events are seen during the nighttime cases than are observed at the surface. It was also found by qualitative comparison that extreme maxima and minima in the total precipitation of the area correspond to areas of maximum and minimum precipitation frequency as derived by the satellite microwave analysis.

It should be noted that although the thresholding technique described in Chapter 3 has worked well in this study, general effectiveness of the technique should not be tacitly assumed for other areas at other times of the year. The technique works during the summer months because of hot surface brightness temperatures which provide a background distinguishable from the cold brightness temperatures of raining areas. Ambiguities occur when conditions change the radiative characteristics of the surface or intervening non-raining atmosphere such as to lower the observed brightness temperature. For this reason supplemental information is needed to resolve as many ambiguities as possible; e.g. surface temperatures, cloudiness, dew formation, polarization, etc. The use of

man-interactive computer analysis systems will allow multi-parameter decision making to be done efficiently.

Precipitation frequency has been derived in this study, however other important precipitation parameters may also be obtainable from this mode of analysis. Areal extent of rainfall events is observable via the satellite and is difficult at best to derive from synoptically spaced raingage measurements. Volumetric estimates of precipitation may be possible if rates can be assigned to the satellite derived rainfall areas, a difficult if not impossible task due to the low response in brightness temperature from a change in rainfall rate compared to changes in surface temperature and emittance. This may be done indirectly from comparison with surface raingage and radar observations. Studies of the distribution of rainfall for varying synoptic conditions, i.e. warm frontal, cold frontal, convective, etc., are also feasible.

Further theoretical and observational investigations are needed in the areas of microwave interaction with the atmosphere and how various surface types affect microwave emission. Studies utilizing extensive ground truth, both of precipitation and surface temperature, are necessary. Also, additional observing frequencies would largely decrease possible ambiguities. The Nimbus-7 satellite carries a Scanning Multichannel Microwave Radiometer (SMMR)* which measures radiation at 6.6, 10.7, 18, 21 and 37 GHz. Information expected from SMMR include sea ice parameters, soil wetness, snow accumulation over ice sheets as well as atmospheric total water vapor and non-precipitating liquid water to enhance rainfall estimations. An important advance in precipitation

---

* See Gloerson and Hardis (1978).

observation from satellites would be a geosynchronous orbiting microwave radiometer (Staelin and Rosenkranz, 1978). This would allow for frequent observation and thus studies of mesoscale precipitating systems.

REFERENCES

Adler, R. F. and E. B. Rodgers, 1977: Satellite-observed latent heat release in a tropical cyclone. Monthly Weather Review, 105, pp. 956-963.

Chandrasekhar, S., 1960: Radiative Transfer. Dover Publications, Inc., New York, 393 pp.

Deirmendjian, D., 1963: Complete Microwave Scattering and Extinction Properties of Polydispersed Cloud and Rain Elements. Rand Corporation Report 12-422-PR, Santa Monica, California, 54 pp.

Gloerson, P., and L. Hardis, 1978: The Scanning Multichannel Microwave Radiometer (SMMR) Experiment, in The Nimbus 7 User's Guide, NASA/ Goddard Space Flight Center, Greenbelt, Maryland, pp. 213-245.

Griffith, C. G., W. L. Woodley, P. G. Grube, D. W. Martin, J. Stout and D. N. Sikdar, 1978: Rain estimation from geosynchronous satellite imagery - visible and infrared studies. Monthly Weather Review, 106, pp. 1153-1171.

Hourly Precipitation Data, 1976: Volume 26, Numbers 4-9 for Illinois, Iowa, Kansas, Minnesota, Missouri, Nebraska, North Dakota, South Dakota and Wisconsin. NOAA, Environmental Data Service, National Climatic Center, Ashville, North Carolina.

Kidder, S. Q., 1976: Tropical oceanic precipitation frequency from Nimbus 5 microwave data. Atmospheric Science Paper 248, Colorado State University, Ft. Collins, Colorado, 50 pp.

Kreiss, W. T., 1968: Meteorological observations with passive microwave systems. Ph.D. dissertation, University of Washington, 198 pp.

Meeks, M. L. and A. E. Lilley, 1963: The microwave spectrum of oxygen in the earth's atmosphere. J. Geophys. Res., 68, 1683-1703.

Rodgers, E., H. Siddalingaiah, A. T. C. Chang and T. Wilheit, 1978: A statistical technique for determining rainfall over land employing Nimbus-6 ESMR measurements. Technical Memorandum 79631, NASA/Goddard Space Flight Center, Greenbelt, Maryland, 33 pp.

Savage, R. C., 1976: The transfer of thermal microwaves through hydrometers. Ph.D. dissertation, University Wisconsin-Madison, 147 pp.

Savage, R. C., and J. A. Weinman, 1975: Preliminary calculations of the upwelling radiance from rain clouds at 37.0 and 19.35 GHz. Bull. Amer. Meteorol. Soc., 56, 1272-1274.

Smith, W. L., 1979: Personal communication, The three point method of analyzing a contaminated Gaussian.

Staelin, D. H., 1966: Measurements and interpretation of the microwave spectrum of the terrestrial atmosphere near 1-centimeter wavelength. J. Geophys. Res., 71, 2875-2881.

Staelin, D. H., and P. W. Rosenkranz, 1978: Applications Review Panel Report: High Resolution Passive Microwave Satellites. Research Laboratory of Electronics, M.I.T., Cambridge, Massachusetts.

Van Vleck, J. H., 1947: The absorbtion of microwaves by uncondensed water vapor. Phys. Rev., 71, 425-433.

Wallace, J. M., 1975: Diurnal variations in precipitation and thunderstorm frequency over the conterminous United States. Monthly Weather Review, 103, 406-419.

Weekly Weather and Crop Bulletin, 1976: Volume 63, Numbers 27, 32 and 36, DOC/DOA, Washington, D.C.

Weinman, J. A. and R. Davies, 1978: Thermal microwave radiances from horizontally finite clouds of hydrometers. J. Geophys. Res., 83, 3099-3107.

Weinman, J. A. and P. J. Guetter, 1977: Determination of rainfall distribution from microwave radiation measured by the Nimbus 6 ESMR. J. Applied Meteorol., 16, 437-442.

Westwater, E. R. and R. L. Abbott, 1965: Passive Probing in the Microwave Region and Microwave Absorbtion Properties of Oxygen. National Bureau of Standards Report 8799, U.S. Department of Commerce, 61 pp.

Westwater, E. R., 1972: Microwave Emission From Clouds. NOAA Technical Report ERL 219-WPL18, NOAA/Environmental Research Laboratories, Boulder, Colorado, 66 pp.

Wilheit, T. T., 1975: The Electrically Scanning Microwave Radiometer (ESMR) Experiment, in The Nimbus 6 User's Guide, NASA/Goddard Space Flight Center, Greenbelt, Maryland, pp. 87-108.

Wilheit, T. T., A. T. C. Chang, M. S. V. Rao, E. B. Rodgers, and J. S. Theon, 1977: A satellite technique for quantitatively mapping rainfall rates over the oceans. J. Appl. Meteor., 16, 551-560.